

Photocurrent in Carbon Nanotubes

Photocurrent in Carbon Nanotubes

Proefschrift

ter verkrijging van de graad van doctor
aan de Technische Universiteit Delft,
op gezag van de Rector Magnificus prof. ir. K.C.A.M Luyben,
voorzitter van het College voor Promoties,
in het openbaar te verdedigen op 2 juli 2014 om 12:30 uur

door

Karin Maria BARKELID

Master of Science in Engineering Nanoscience, Lund University
geboren te Helsingborg, Sweden.

Dit proefschrift is goedgekeurd door de promotor:

Prof. dr. ir. L. P. Kouwenhoven

Copromotor:

Dr. V. Zwiller

Samenstelling van de promotiecommissie:

Rector Magnificus	voorzitter
Prof. dr. ir. L.P. Kouwenhoven	Technische Universiteit Delft, promotor
Dr. V. Zwiller	Technische Universiteit Delft, copromotor
Prof. dr. Y. M. Blanter	Technische Universiteit Delft
Prof. dr. E. Charbon	Technische Universiteit Delft
Prof. dr. H. P. Urbach	Technische Universiteit Delft
Prof. dr. F. M. Mulder	Technische Universiteit Delft
Prof. dr. W. Wenseleers	University of Antwerp
Prof. dr. ir. R. Hanson	Technische Universiteit Delft, reservelid

ISBN: 978-90-8891-914-5

Casimir PhD Series, Delft-Leiden 2014-17

An electronic version of this thesis is available at www.library.tudelft.nl/dissertations

Printed by: Proefschriftmaken.nl || Uitgeverij BOXpress

Cover design: Proefschriftmaken.nl || Uitgeverij BOXpress

Copyright © 2014, Maria Barkelid

Contents

1	Introduction	1
1.1	Nanoscience and Nanotechnology	1
1.2	Carbon Nanotubes	2
1.3	Research Scope	3
1.4	Thesis Outline	3
	Bibliography	5
2	Theory of Carbon Nanotube Optoelectronics	7
2.1	Electronic Band Structure of Carbon Nanotubes	8
2.1.1	Crystallographic Structure of Carbon Nanotubes	8
2.1.2	Band Structure of Graphene	10
2.1.3	Band Structure of Carbon Nanotubes	10
2.1.4	Density of States	12
2.2	Optical Transitions in Carbon Nanotubes	13
2.2.1	Excitons in Carbon Nanotubes	13
2.3	Carbon Nanotube p-n Junctions	15
2.3.1	Semiconductor p-n Junctions	15
2.3.2	A p-n Junction in a Carbon Nanotube	16
2.4	Photocurrent in Carbon Nanotubes	17
2.4.1	Photocurrent Generation	19
2.4.2	Electron-Hole Pair Creation and Annihilation	19
	Bibliography	21
3	Device Fabrication and Measurement Techniques	23
3.1	Fabrication of air-suspended carbon nanotube devices	24
3.2	Carbon nanotube synthesis	28
3.3	Experimental Setup	29
3.4	Photocurrent imaging and spectroscopy	30
	Bibliography	33

4	Imaging the Formation of a p-n Junction in a Suspended Carbon Nanotube with Scanning Photocurrent Microscopy	35
4.1	Introduction	36
4.2	Experimental Setup	36
4.3	Scanning Photocurrent Microscopy of a Tunable p-n Junction . . .	37
4.4	Imaging the Formation of a p-n Junction	38
4.5	Conclusions	41
	Bibliography	43
5	Probing Optical Transitions in Individual Carbon Nanotubes using Polarized Photocurrent Spectroscopy	45
5.1	Introduction	46
5.2	Device characterization	46
5.3	Polarization dependence	48
5.4	Extracting the dielectric constant of a semiconducting carbon nanotube	49
5.5	Polarized photocurrent spectroscopy	49
5.6	Quantitative absorption cross section of a semiconducting carbon nanotube	51
5.7	Conclusions	52
	Bibliography	54
6	Single Carbon Nanotube Photovoltaic Device	57
6.1	Introduction	58
6.2	Characterization	58
6.2.1	Single Carbon Nanotube Photovoltaics	59
6.3	Energy Conversion Efficiency	60
6.3.1	Internal Power Conversion Efficiency	61
6.4	Carbon Nanotube Photovoltaic Device	62
6.5	Conclusion	64
	Bibliography	65
7	Photocurrent Generation in Semiconducting and Metallic Carbon Nanotubes	67
7.1	Introduction	68
7.2	Photocurrent response from a metallic and a semiconducting carbon nanotube	68
7.2.1	Identification of individual carbon nanotubes	69
7.2.2	Metallic vs. Semiconducting Carbon Nanotubes	70
7.2.3	Scanning photocurrent microscopy of a metallic carbon nanotube	71

7.3	Photocurrent maps of a semiconducting and a metallic carbon nanotube	73
7.3.1	Experimental conditions	74
7.4	Photocurrent response from nanotube / electrode interface	76
7.4.1	Spatial dependence of the photocurrent response	76
7.4.2	Laser induced temperature	78
7.5	Low temperature measurements	79
7.6	Pulsed and continuous-wave excitation	79
7.7	Additional devices	82
7.8	Conclusions	83
	Bibliography	84
8	Resonant Photocurrent Response in a Semiconducting Carbon Nanotube	87
8.1	Introduction	88
8.2	Device characterization	88
8.3	Photocurrent response from the E11 and E22	89
8.3.1	Power Dependence	91
8.3.2	Photocurrent response with thermal coupling to the environment	93
8.4	Conclusions	94
	Bibliography	96
9	Large and Tunable Photothermoelectric Effect in Single-Layer MoS₂	99
9.1	Introduction	100
9.2	Sample preparation and characterization	100
9.3	Photothermoelectric Effect in MoS ₂	103
9.3.1	Relationship between morphology and SPCM measurements	105
9.3.2	Gate dependent photocurrent spectroscopy	106
9.4	Tunable Seebeck Effect in MoS ₂	109
9.5	Conclusions	112
	Bibliography	113
10	Conclusions and Outlook	117
10.1	Summary and Conclusions	117
10.2	Future Directions	118
10.3	Current Status of the Field	121
10.4	Outlook	122
	Bibliography	124

A Appendix to Chapter 7	127
A.1 The effect of color scale choice on the photocurrent map	127
A.2 Line profiles from the photocurrent response in a semiconducting carbon nanotube	128
A.2.1 Nanotube A	129
A.2.2 Nanotube B	130
A.2.3 Nanotube C	130
A.2.4 Nanotube D	132
A.2.5 Nanotube E	133
A.3 Photocurrent from a homogeneously doped semiconducting carbon nanotube	133
A.3.1 Experiment	133
A.3.2 Discussion	135
A.4 Conclusion	135
Bibliography	137
Summary	139
Samenvatting	141
Acknowledgement	143
Curriculum Vitae	147
List of Publications	149

Chapter 1

Introduction

1.1 Nanoscience and Nanotechnology

Nanoscience, although at the front of modern cutting-edge research, is not a new phenomenon, but dates back as far as to Roman times. Perhaps the most famous example of how nanotechnology was used to enhance glassware is the Lycurgus cup [1]. By embedded nanoparticles the cup assumes a green color if light is shone from the outside, but a red color if the light source is located inside the cup.

However, nanoscience as a field of research was not founded until many years later, namely in 1959 in a speech by physicist Richard Feynman, where he stated the now famous words: "There is plenty of room at the bottom". Since then this field has experienced a booming development.

Nanoscience, sculpturing with atoms [2], inspired a new way of thinking, where technological devices can be built bottom-up instead of top-down. This new technology required new tools in order to see and manipulate these miniature structures. As a result the electron microscope and the atomic force microscope were developed.

Nanoscience in its essence represents the fundamental research of molecules and structures of dimensions 100 nm or less. This field of nanoscience is truly interdisciplinary in the sense that it brings together scientists from physics, chemistry and biology. At the nanoscale the physical properties of a material may be very different than properties of the material in bulk [3]. Nanotechnology is the field where this diverse knowledge is put to use to design and develop devices at

the nanoscale. A continuous miniaturization in the semiconductor industry has fueled the development of yet smaller, however, still reliable and efficient devices.

1.2 Carbon Nanotubes

Carbon nanotubes are part of the family of fullerenes [4] and can be viewed as a sheet of graphene [5] rolled up to a cylinder of a diameter as small as 1 nm, see figure 1.1. Depending on how the graphene sheet is cut when rolling it up, the nanotube will end up with a certain chirality [6]. This is a property of the carbon nanotube which determines its electrical and optical properties. There are over 300 different chiralities of nanotubes. The chirality will determine if the nanotube is metallic or semiconducting.

First discovered in 1991 by Iijima [7], carbon nanotubes have experienced an intense research interest in fields from physics and material science to medicine. Significant advances such as controlled synthesis [8–10], observation of photoluminescence [11] and gate-defined quantum dots [12] have already been made. The first carbon nanotube transistor was created in 1998 [13,14] and the first reports on light emission from a carbon nanotube transistor followed in 2003 [15].

In the early 1990's the main questions were: "can we make single-walled carbon nanotubes?" and "would they be interesting structures to work on?". Once R. Saito introduced the concept of varying metallicity and semiconductivity in carbon nanotubes [16], this concept was so exceptional that the community for a very long time did not believe him. We now know that this is one of the most exciting properties of nanotube research and what makes the nanotube research so rich.

The field of carbon nanotube optics was born a few years later and has similarly matured severely in the last years. In early 2000's, when excitons were discovered in carbon nanotubes, the main question circulating was: "excitons, do we need them?". We now know that excitonic effects completely dominate the nanotube optical response. The community thereafter investigated dark excitons, trions, quantum optics and photovoltaics.

In spite of these remarkable advances made, there is still several challenges that remains. One of the most pressing ones is the nanotube chirality. If one would like to scale up the production of carbon nanotubes to levels of interest for industry, the fact that carbon nanotubes come in several chiralities, each with different electrical and optical properties, poses a big obstacle. Today, a lot of research effort goes into the study of chirality selective synthesis [17] as well as post-synthesis selection and purification techniques [18,19].

1.3 Research Scope

Light-matter interaction has intrigued scientists and engineers for generations. At the nanoscale the principles of interaction between light and matter, down to the scale of single photons and single electrons, exhibit exotic behavior, which can differ substantially from macroscopic systems.

In this thesis we have studied light-matter interaction in carbon nanotubes. As nanotubes exhibit large mobilities and current carrying capabilities [20, 21] and at the same time are optically active materials [6] they provide an optimal platform to combine optics and electronics. Their large aspect ratio makes them ideal systems to study one-dimensional effects. The system of choice in this thesis is an ultra-clean carbon nanotube, which enables us to study physics originating from the carbon nanotube itself instead of for example impurities, with a p-n junction incorporated. A p-n junction is the fundamental building block in optoelectronic devices.

We employ the scanning photocurrent microscopy (SPCM) technique to monitor the spatial development of the photoresponse as a function of charge carrier doping, as well as study the photocurrent response in the near infra-red part of the spectrum. By probing specific optical resonances we can gain information about physical properties of the carbon nanotubes, such as their dielectric constant and absorption coefficient. We then continue to show that these optical resonances also can be of great interest for designing optoelectronic devices, such as solar cells, based on carbon nanotubes. Thereafter this thesis continues by going to the bottom of which physical mechanism is responsible for the photocurrent generation in carbon nanotubes and we here expand our research further by considering both semiconducting and metallic carbon nanotubes. Finally we use the technique of photocurrent imaging on a related material system (MoS_2) to establish the photocurrent generation mechanism also in this material system.

1.4 Thesis Outline

In **chapter 2** the basic physics of carbon nanotubes will be outlined. Thereafter a more detailed description of the optical properties of carbon nanotubes will follow as well as a review of p-n junction physics.

In **chapter 3** the fabrication scheme and growth process of the individually suspended carbon nanotube devices will be described. The experimental setup used for the measurements will be presented as well as a standard post-measurement analysis technique used.

Chapter 4 describes an experiment on a carbon nanotube where the scanning

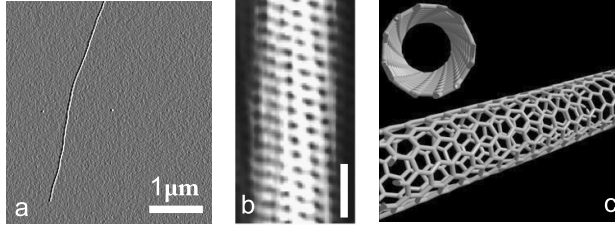


Figure 1.1: Carbon nanotubes. (a) Atomic force microscopy image of a carbon nanotube, (b) Scanning tunneling microscopy image of a carbon nanotube (c) Schematic of a carbon nanotube. Figure adapted from ref [22].

photocurrent microscopy technique was employed to study the emergence of a p-n junction as a function of charge carrier doping. This chapter introduces our devices and measurement technique and demonstrates the high level of control and tunability of our system.

In **chapter 5** we use polarized photocurrent spectroscopy to address the optical resonances in our carbon nanotube. From the polarization dependence we can extract a dielectric constant for the semiconducting nanotube and from the photocurrent enhancement on the optical resonances we can estimate a lower limit for a quantitative number for the absorption coefficient in a carbon nanotube.

Chapter 6 shows how these resonances can be used for efficient energy conversion in carbon nanotube photovoltaic devices.

Chapter 7 presents a study of the underlying physical mechanism behind photocurrent generation in carbon nanotubes. It is shown that the photocurrent originates from the photothermal effect in metallic carbon nanotubes, while it in semiconducting nanotubes is a result of the photovoltaic effect.

In **chapter 8** the photocurrent generation mechanism in a semiconducting nanotube is further explored under various experimental conditions.

In **chapter 9** photocurrent has been used to study a single 2-dimensional sheet of MoS_2 . It is found that the photocurrent in MoS_2 comes from the photothermoelectric effect and a large and tunable Seebeck coefficient is measured for the single-layer MoS_2 device.

In **chapter 10** some concluding remarks are presented, together with an outlook and possible future directions of this field of photocurrent on carbon materials.

Bibliography

- [1] I. Freestone, N. Meeks, M. Sax and G. Higgitt. The lycurgus cup - a roman nanotechnology. *Gold Bulletin* **40**, 270 (2007).
- [2] D. M. Eigler and E. K. Schweizer. Positioning single atoms with a scanning tunnelling microscope. *Nature* **344**, 524 (1990).
- [3] M. Ratner and D. Ratner. *Nanotechnology: A Gentle Introduction to the Next Big Idea*. Pearson Education Inc, New Jersey (2003).
- [4] H. W. Kroto, J. R. Heath, S. C. O'Brien, R. F. Curl and R. E. Smalley. C60: Buckminsterfullerene. *Nature* **318**, 162 (1985).
- [5] K. Novoselov *et al.* Electric field effect in atomically thin carbon films. *Science* **306**, 666 (2004).
- [6] F. Leonard. *The Physics of Carbon Nanotube Devices*. William Andrew Inc., Norwich (2009).
- [7] S. Iijima. Helical microtubules of graphite carbon. *Nature* **354**, 56 (1991).
- [8] H. Dai *et al.* Controlled chemical routes to nanotube architectures, physics and devices. *J. Phys. Chem. B* **103**, 11246 (1999).
- [9] M. J. Bronikowski, P. A. Willis, D. T. Colbert, K. A. Smith and R. E. Smalley. Gas-phase production of carbon single-walled nanotubes from carbon monoxide via the hipco process: A parametric study. *J. Vac. Sci. Technol. A* **19**, 1800 (2001).
- [10] M. S. Strano *et al.* Electronic structure control of single-walled carbon nanotube functionalization. *Science* **301**, 1519 (2003).
- [11] M. J. O'Connell *et al.* Band gap fluorescence from individual single-walled carbon nanotubes. *Science* **297**, 593 (2002).
- [12] M. J. Biercuk, N. Mason and C. M. Marcus. Locally addressable tunnel barriers within a carbon nanotube. *Nano Lett.* **4**, 2499 (2004).
- [13] S. J. Tans, A. R. M. Verschueren and C. Dekker. Room-temperature transistor based on a single carbon nanotube. *Nature* **393**, 49 (1998).
- [14] R. Martel, T. Schmidt, H. R. Shea, T. Hertel and P. Avouris. Single- and multi-wall carbon nanotube field-effect transistors. *Appl. Phys. Lett.* **73**, 2447 (1998).

- [15] J. Misewich *et al.* Electrically induced optical emission from a carbon nanotube fet. *Science* **300**, 783 (2003).
- [16] R. Saito, M. Fujita, G. Dresselhaus and M. S. Dresselhaus. Electronic structure of chiral graphene tubules. *Appl. Phys. Lett.* **60**, 2204 (1992).
- [17] W.-H. Chiang and R. M. Sankaran. Linking catalyst composition to chirality distributions of as-grown single-walled carbon nanotubes by tuning $\text{ni}(x)\text{fe}(1-x)$ nanoparticles. *Nature Mat.* **8**, 882 (2009).
- [18] R. Krupke, F. Hennrich, H. von Lohneysen and M. M. Kappes. Separation of metallic from semiconducting single-walled carbon nanotubes. *Science* **301**, 344 (2003).
- [19] M. S. Arnold, A. A. Green, J. F. Hulvat, S. I. Stupp and M. C. Hersam. Sorting carbon nanotubes by electronic structure using density differentiation. *Nature Nanotechn.* **1**, 60 (2006).
- [20] F. Kreupl *et al.* Carbon nanotubes in interconnect applications. *Microelectron. Eng.* **64**, 399 (2002).
- [21] Q. Ngo *et al.* Electron transport through metal-multiwall carbon nanotube interfaces. *IEEE Trans. Nanotechnol.* **3**, 311 (2004).
- [22] L. C. Venema, V. Meunier, P. Lambin and C. Dekker. Atomic structure of carbon nanotubes from scanning tunneling microscopy. *Phys. Rev. B* **61**, 2991 (2000).

Chapter 2

Theory of Carbon Nanotube Optoelectronics

This chapter introduces some theoretical concepts which lay the foundation for the rest of this thesis. First the electronic band structure of carbon nanotubes are worked out from the band structure of graphene. Thereafter the optical transitions which occurs in carbon nanotubes will be outlined and we will learn about the strong excitonic nature in nanotubes as well as the radiative and non-radiative recombination pathways. We then discuss the carbon nanotube p-n junction and how this can be realized by remote doping, before we finish by discussing the concept of photocurrent.

2.1 Electronic Band Structure of Carbon Nanotubes

Carbon nanotubes are one-dimensional objects, consisting of a rolled up sheet of graphene. They belong to the carbon family together with the zero-dimensional fullerenes, the two-dimensional graphene and the three-dimensional diamond structure. Carbon nanotubes exist as multiwalled nanotubes, first discovered in 1991 [1] with a diameter of ~ 10 nm or larger, and as single-walled carbon nanotubes, discovered two years later [2, 3] with a diameter of ~ 1 nm.

To deduce the band structure for carbon nanotubes it is instructive to start from the band structure of graphene. However, before discussing the electronic band structure, we will begin by reviewing the crystallographic structure of carbon nanotubes.

2.1.1 Crystallographic Structure of Carbon Nanotubes

To construct a carbon nanotube we start from a single graphene layer. The atoms in the graphene are arranged in a hexagonal honeycomb pattern, with a carbon-carbon bond length, a , of 0.142 nm. A schematic of the carbon honeycomb lattice can be found in figure 2.1. The hexagonal lattice can be described as two sublattices with atoms A and B. A unit cell can be defined to contain two atoms (A and B), see figure 2.1a. The lattice vectors are \vec{a}_1 and \vec{a}_2 and the lattice constant $a_i = \sqrt{3}a = 0.246$ nm. In the reciprocal space the lattice becomes rotated 90° and the lattice vectors are \vec{b}_1 and \vec{b}_2 , shown in figure 2.1. Any point in the lattice can be reached by a combination of $n \cdot \vec{a}_1 + m \cdot \vec{a}_2$ unit vectors from a defined origin. A vector, C , which connects the point (n, m) with the origin $(0, 0)$ is called the wrapping vector. Once the carbon nanotube is rolled up the wrapping vector goes around the circumference of the tube so that the tip and tail of the vector meet. As illustrated in figure 2.2a the angle between the wrapping vector, C , and \vec{a}_1 (top arrow in figure 2.2a) is called the chiral angle, θ .

Depending on how the graphene sheet is rolled up, the orientation of the carbon nanotube axis with respect to the graphene crystal axis will differ. This gives the carbon nanotubes a specific chirality, or (n, m) index. Each (n, m) combination corresponds to a chiral angle θ and a specific nanotube diameter, d , according to [4, 5]:

$$\theta = \arctan \left[\frac{\sqrt{3}m}{m + 2n} \right] \quad (2.1)$$

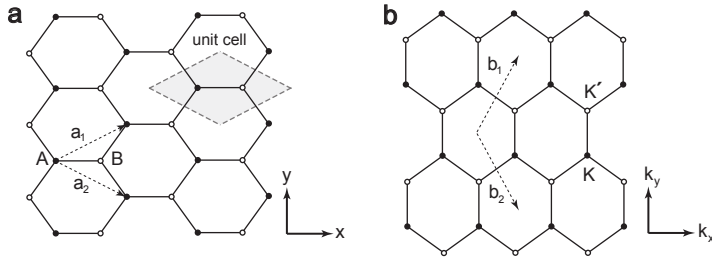


Figure 2.1: Carbon lattice. (a) The honeycomb lattice in real space. The two sublattices A and B are indicated, together with the two lattice vectors a_1 and a_2 . (b) The lattice in reciprocal space. The two corner points K and K' , and the reciprocal lattice vectors b_1 and b_2 are indicated.

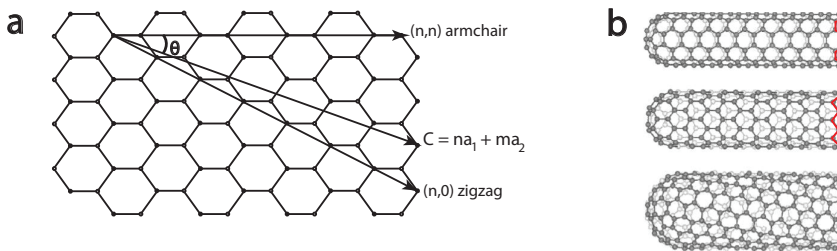


Figure 2.2: Construction of carbon nanotubes. (a) The chiral angle θ at which the graphene sheet is cut defines the chirality (n,m) of the carbon nanotube. (b) Examples of carbon nanotube geometries. Top: armchair, middle: zigzag and bottom: a chiral carbon nanotube. Figure adapted from ref [5].

$$d = C/\pi = \frac{a}{\pi} \sqrt{n^2 + m^2 + nm}. \quad (2.2)$$

The chiral index determines if the nanotube is semiconducting or metallic. There are also two directions in the graphene lattice that generates non-chiral nanotubes. One is the (n,0) direction, which is called zigzag, and the other is the (n,n) direction, which is called armchair. Armchair nanotubes are always metallic. All other combinations of (n,m) gives chiral nanotubes. The origin of the names is illustrated in figure 2.2b.

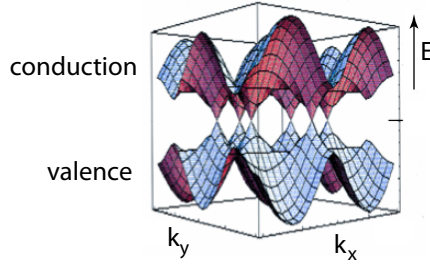


Figure 2.3: Band structure of graphene. The energy dispersion of graphene as a function of wavevector \mathbf{k} . The conduction and valence bands meet at the six K-points. Figure adapted from ref [6].

2.1.2 Band Structure of Graphene

Carbon atoms have four valence electrons in its outer shell. Three of these electrons form van der Waals bonds to the neighboring atoms in the plane in the honeycomb lattice, generating a sp^2 hybridization. The fourth electron occupies the p_z orbital, oriented perpendicular to the graphene plane. These electrons form delocalized electronic states called π -bonds. Only these delocalized electrons contribute to the electronic properties of the graphene and the carbon nanotubes. These electronic properties can be described with a tight-binding model for graphene [4, 5].

Starting in the reciprocal lattice, the first Brillouin zone is hexagonal and at its corners the conduction and valence band touch, as shown in figure 2.3. These corner points are called K-points and consist of two inequivalent points, K and K'. The energy dispersion in the vicinity of these K points is conical, making graphene a semimetal or a zero bandgap semiconductor.

2.1.3 Band Structure of Carbon Nanotubes

As we roll up the graphene layer to a carbon nanotube, we find that the momentum dispersion becomes quantized. We now consider a coordinate system for the momentum vector, \mathbf{k} , with one component, k_{\parallel} , pointing along the carbon nanotube axis, and one component, k_{\perp} , pointing around the nanotube axis. The $(k_{\parallel}, k_{\perp})$ coordinate system is rotated with respect to (k_x, k_y) by the chiral angle θ . The k_{\perp} vector becomes quantized due to the small diameter of the carbon nanotube (while k_{\parallel} remains continuous, assuming infinite length of the nanotube) [4].

This results in discrete lines in the momentum dispersion of a carbon nan-

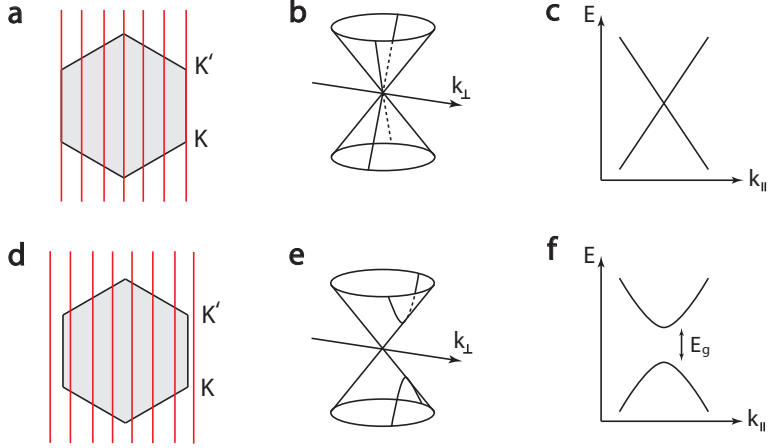


Figure 2.4: Electronic band structure of carbon nanotubes. The quantized wavevector k_{\perp} results in a set of discrete states, indicated with red lines. Each line correspond to a subband. (a) When these lines pass through the K points they will cut through the middle of the conical energy dispersion in (b) and result in a zero band gap (metallic) nanotube, shown in (c). When the allowed k-lines do not pass directly through a K point, as in (d), the cut through the energy dispersion will have an offset from the centre, shown in (e). (f) This will result in a band gap, E_g in the (semiconducting) carbon nanotube.

otube, that intersects the energy dispersion of the graphene sheet:

$$\Delta k_{\perp} \pi d = 2\pi. \quad (2.3)$$

Figure 2.4 illustrates this concept. If one of these quantized k-lines (shown in red) goes through a K point the carbon nanotube will have a conical energy dispersion, similar to graphene, and be metallic in nature (figure 2.4a-c). If no line passes exactly through a K point (2.4d) they will cut the conical energy dispersion of graphene (2.4e) and the carbon nanotube will have a band gap and become semiconducting. The band gap, E_g will be determined by the distance between the K point and the closest k_{\perp} -line, This means that for semiconducting carbon nanotubes the band gap is inversely proportional to the nanotube diameter, independently of chirality [7]. The relation between band gap and nanotube diameter can be determined as:

$$E_{gap} = 2\gamma_0 a / (\sqrt{3}d) \simeq \frac{0.8}{d} \quad (2.4)$$

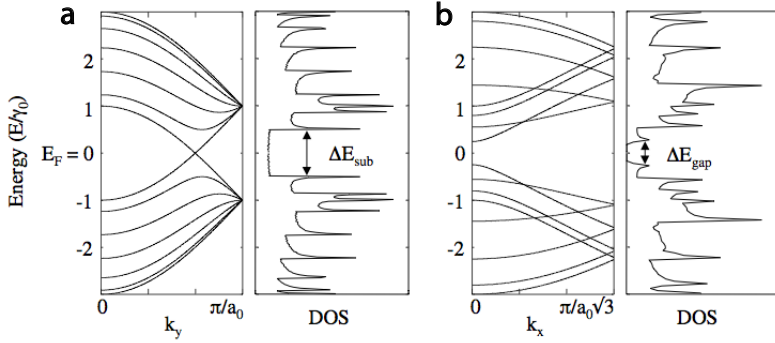


Figure 2.5: Density of states for a metallic and a semiconducting carbon nanotube. (a) Left: band structure of a (6,6) armchair nanotube. The corresponding density of states are shown on the right with the separation between the first two subbands indicated as ΔE_{sub} . (b) Band structure (left) and density of states (right) of a (7,0) zigzag nanotube. The band gap which arise in the density of states is indicated as ΔE_{gap} . Figure adapted from ref [10].

where a is the lattice constant and $\gamma_0 \approx 2,9$ eV is the transfer integral from the tight binding model for graphene [4, 5].

The metallicity of carbon nanotubes can be deduced from $n - m = 3q$, where q is an integer. If q is not an integer the nanotube is semiconducting. This results in 1/3 of all nanotube species being metallic in nature and 2/3 being semiconducting [8].

2.1.4 Density of States

From the band diagram the density of states of a carbon nanotube can be calculated. Figure 2.5 shows the band structure and density of states for a metallic and a semiconducting carbon nanotube. The band crossing at the Fermi level in figure 2.5a gives rise to a non-zero density of states for this (6,6) armchair carbon nanotube. For the (7,0) zigzag semiconducting carbon nanotube in figure 2.5b the band structure has a gap around the Fermi level, which translates to the density of states. In the density of states a number of peaks arise at the edges of the sub-bands. These peaks are called van Hove singularities and have been shown to have a large impact on the optical properties of carbon nanotubes [9]. The energy between the two lowest singularities in the metallic nanotube has been defined as ΔE_{sub} while for the semiconducting nanotube it is defined as the nanotube band gap, ΔE_{gap} [10].

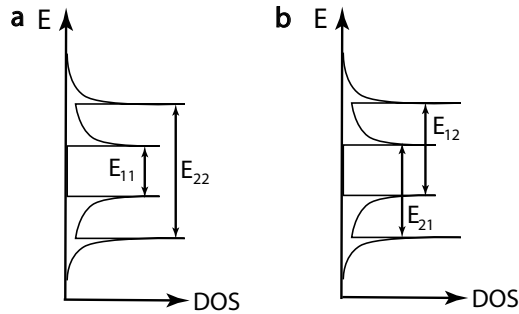


Figure 2.6: Optical transitions in a carbon nanotube. (a) The E_{11} (E_{22}) transition occur between the first (second) subbands. (b) The E_{12} and E_{21} transition occurs between subbands of different index.

2.2 Optical Transitions in Carbon Nanotubes

In a first simple model optical transitions in carbon nanotubes take place between subbands of the same or different index. For example, if a transition occurs between the first valence band and the first conduction band it would be indexed E_{11} . Similarly E_{22} (E_{12}) occurs between the second (first) valence band and the second conduction band. These transitions are schematically illustrated in figure 2.6. For a more detailed explanations of when the different transitions occur, please see chapter 5.

In many bulk material systems, optical transitions are band-to-band transitions explained by single particle physics. In low-dimensional material systems the optical properties are typically governed by many-body effects. A carbon nanotube is an almost ideal one-dimensional system and hence exhibit a very strong Coulomb interaction [11, 12]. This Coulomb interaction is the reason the optical properties of carbon nanotubes are dominated by excitons [11].

Because of this large Coulomb interaction, the exciton binding energy in carbon nanotubes can be of the order of 1/3 of the band gap. With exciton binding energies that can approach 1 eV, excitonic physics in carbon nanotubes can be readily observed at room temperature [9].

2.2.1 Excitons in Carbon Nanotubes

The Coulomb interaction consists of one attractive potential which binds the electron and hole together as an exciton. This attractive potential gives rise to the exciton state with a lower energy than the free electron-hole state, illustrated in figure 2.7a. This results in a red-shift of the optical band gap for the carbon

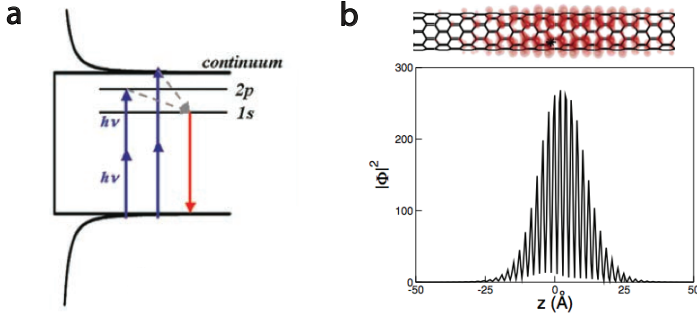


Figure 2.7: Excitons in carbon nanotubes. (a) With two-photon absorption measurements experimental evidence could be provided for the excitonic picture of optical transitions in carbon nanotubes. Figure adapted from [14]. (b) Simulated exciton wave functions for a (8,0) carbon nanotube. The total spatial extension of the exciton has a radius of about 2,5 nm. Figure adapted from [12].

nanotube [13]. The large exciton binding energy (as discussed above) can be visualized using a standard expression:

$$E_b = -13.6eV \frac{m^*}{m_0} \left(\frac{\epsilon_0}{\epsilon} \right)^2 \quad (2.5)$$

where m^* is the effective mass, m_0 the free electron mass, ϵ_0 is the permittivity of vacuum and ϵ the nanotube dielectric constant [11]. The dielectric constant expresses the screening of the Coulomb interaction. In a one-dimensional material such as carbon nanotubes this screening is weak, which increases the binding energy. Chapter 5 presents experimental results on determining the dielectric constant of a carbon nanotube.

Experimental evidence of the excitonic nature of the optical transitions in carbon nanotubes was realized with a two-photon absorption measurement [14], shown in figure 2.7a. The spatial radius of a carbon nanotube exciton, at FWHM, has been experimentally determined to approximately 1.2 nm for a (6,5) nanotube [14], in agreement with calculations, as seen in figure 2.7b [12].

Apart from the attractive potential the Coulomb interaction also has a repulsive contribution. This repulsive electron-electron interaction is a many-body effect not included in the simple single particle picture. This electron-electron interaction causes a blue-shift of the optical band gap of the carbon nanotube [13]. These two components of the Coulomb interaction also gives rise to the optical selection rules for carbon nanotubes, as discussed below.

2.3 Carbon Nanotube p-n Junctions

When studying light-matter interaction in carbon nanotubes we must choose a platform on which to carry out the work. One could think of several approaches to do such a study, however, the most straight forward approach would be to use a key component from the semiconductor world: the p-n junction.

The p-n junction will be our workhorse throughout this thesis and we will therefore now shortly describe the principle of a standard semiconducting p-n junction. Later we will describe how this structure can be incorporated into a carbon nanotube by means of electrostatic doping.

2.3.1 Semiconductor p-n Junctions

When a p-doped and a n-doped semiconductor are brought into contact, holes from the p-doped side will diffuse to the n-doped side and electrons will diffuse in the opposite direction. The charge carriers will leave behind negatively (on the p-side) and positively (on the n-side) charged ions, which are fixed in the crystal lattice, figure 2.8a. These ions are called space charges and as a result of these space charges an electric field occurs with a direction from positive to negative charge, see figure 2.8b-c.

At thermal equilibrium the Fermi levels of the p-doped and n-doped side line up and causes a band bending, as shown in figure 2.8d. The difference in electrostatic potential between the two sides is called the built-in potential, V_{bi} . The region containing the space charges is depleted of mobile carriers and hence named the depletion region.

When the p-n junction is forward-biased, V_F , the electrostatic potential across the junction becomes $V_{bi}-V_F$, and the width of the depletion region is increased. Contrary, if the p-n junction is reversed biased, V_R , the electrostatic potential becomes $V_{bi}+V_R$, and the depletion region width is reduced [15]. An example of an I-V curve for a p-n junction (in one of our carbon nanotubes) is shown in figure 2.9.

The IV characteristic of the p-n junction changes under illumination. If a photon is absorbed in the p-n junction its energy is used to promote an electron from the valence band to the conduction band. The power generated in the device can be calculated from the IV characteristic and will generate a power conversion efficiency of the device. More details about how to extract the power conversion efficiency can be found in chapter 6. When forward biased, the injected carriers can recombine and emit light, as electroluminescence [16, 17] or thermal light emission [18].

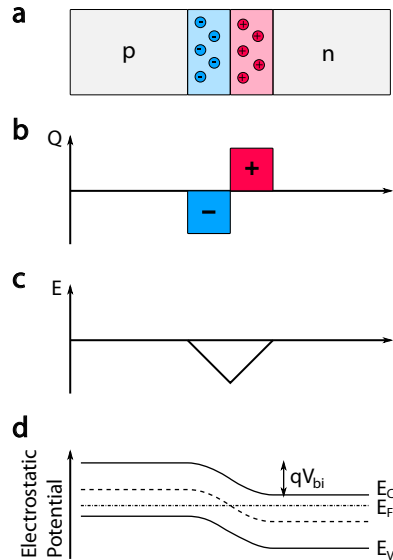


Figure 2.8: Semiconducting p-n junction. (a) When a p-doped and a n-doped material is brought in contact with one another the mobile carriers close to the junction will deplete the region and leave behind space charges in the lattice. (b) The charges are positive on the n-side and negative on the p-side. (c) The charges give rise to an electric field, pointing from the positive to the negative region, with a maximum in the middle of the junction. (d) At the junction a band bending in the electrostatic potential results from the electric field in the junction.

2.3.2 A p-n Junction in a Carbon Nanotube

A p-n junction in a carbon nanotube can be realized in many different ways, such as chemical functionalization [19,20] or by nanoparticle coating [21]. In this thesis we have chosen to use electrostatic doping. With a pair of metallic gates (see chapter 3 for details) located a distance away from the carbon nanotube the potential landscape of the nanotube can be tuned. By applying a voltage to the metallic gates the electrostatic potential will attract electrons in the nanotube (positive voltage) and cause a band bending in the nanotube such that the Fermi level ends up in the conduction band. The opposite is true for a negative potential, where the electrons in the nanotube are repelled by the potential on the gate and give rise to band bending such that the Fermi level ends up in the valence band.

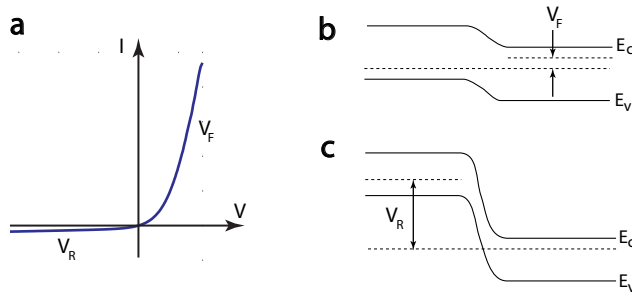


Figure 2.9: Biasing the p-n junction. (a) A representative I-V characteristic for a p-n junction. The data is measured on a semiconducting carbon nanotube p-n junction. (b) In forward bias, V_F , the band-bending at the p-n junction is reduced, the depletion region is widened and a current flows through the device. (c) In reverse bias, V_R , the band-bending is increased, the depletion width reduced and only a small reverse saturation current flows through the device.

If voltages of opposite polarity would be applied to the two gates one side of the nanotube would be n-doped and one side would be p-doped. In the interface between the two potential fields a p-n junction arise in the carbon nanotube. This has been illustrated in figure 2.10, where a positive (negative) gate voltage induces n-type (p-type) doping in the carbon nanotube, respectively. Electrostatic doping allows for a controllable and tunable doping level in the carbon nanotube. Figure 2.11 shows how tuning the gate voltage can realize different doping configurations in the carbon nanotube device.

2.4 Photocurrent in Carbon Nanotubes

Photoconductivity is a materials capability of converting an optical signal into an electrical signal. Upon illumination a photon can be absorbed in a material, electrons and holes generated and conducted through the material to the external circuit. Carbon nanotubes are promising systems for photoconduction applications as they have a direct band gap for every subband [22] and high carrier mobility [23].

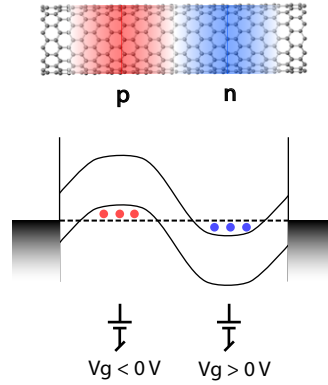


Figure 2.10: Carbon nanotube p-n junction. By applying a voltage to the metal gates a p-n junction can be created in the carbon nanotube, by means of electrostatic doping. A negative (positive) voltage gate introduces a p-type (n-type) doping and a p-n junction is formed at the interface.

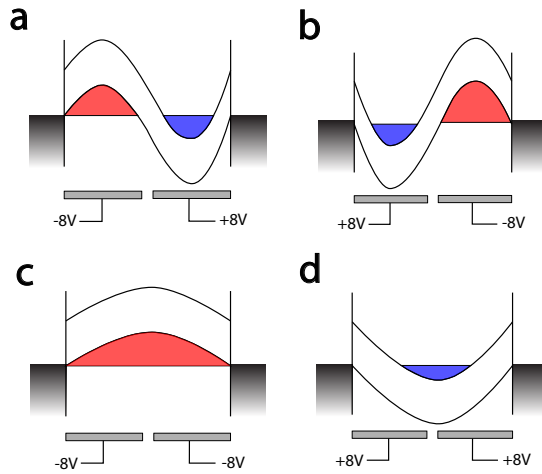


Figure 2.11: Electrostatic doping of a carbon nanotube. A negative voltage on the gates will induce a p-type doping in the carbon nanotube, while positive voltage will result in n-type doping. (a) With opposite polarity of the gate voltage a p-n junction (or n-p junction, (b)) can be created. (c) With the same polarity gate voltage a homogeneously p-doped (or n-doped, (d)) transistor channel can be realized.

2.4.1 Photocurrent Generation

When light is incident on a semiconductor the first thing that happens is the absorption of photons. Thereafter the energy of the absorbed photon goes into the creation of electron-hole pairs. An increased number of charge carriers in the material leads to an increased current. The increase in current, on top of the regular (dark) current flowing through the material is called the photocurrent. In order to generate photocurrent, illumination alone will not be sufficient. A uniform direction of the charge carriers is necessary to create a net photocurrent. This can be realized by altering the symmetry of the semiconductor, for example by introducing a p-n junction.

When a carbon nanotube is photoexcited, due to its one-dimensionality the electrons and holes almost exclusively create excitons, rather than free electron-hole pairs [11,14]. To break these excitons into free electrons and holes (in order for them to contribute to the current) an electric field, for example at a p-n junction, is necessary. (In chapter 7 we discuss an alternative way of generating photocurrent by hot electrons.)

2.4.2 Electron-Hole Pair Creation and Annihilation

The creation and annihilation processes of electrons and holes in carbon nanotubes are of significant importance for its optical properties. The creation of electron-hole pairs in carbon nanotubes were first described by Kane et al. [24]. In this electron-hole pair creation process there is a strong influence of carrier interaction. Considering only one electron theory the ratio between the first and second subband should be two. (For small diameter nanotubes this number can vary due to the curvature and triangular warping effects.) However, experimental results show that this ratio has a value closer to 1,75 [25]. This originates from a many-body process (shown in figure 2.12) where one electron hole-pair in the second subband can relax and create two electron-hole pairs in the first subband [24,26], according to:

$$e_2 + h_2 \rightarrow (e_1 + h_1) + (e_1 + h_1). \quad (2.6)$$

An electron-hole pair in a carbon nanotube can also undergo non-radiative recombination, such as Auger recombination. In this process the interaction between two electron-hole pairs results in the recombination of one of the electron-hole pairs, once the other retrieve kinetic energy to be excited to the second subband [26–28]:

$$(e_1 + h_1) + (e_1 + h_1) \rightarrow e_2 + h_2. \quad (2.7)$$

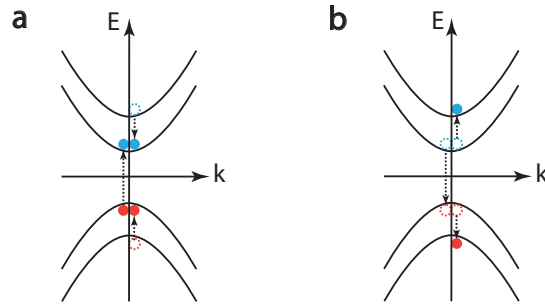


Figure 2.12: Carrier interaction. (a) Electron-hole pair creation through relaxation by an electron-hole pair from a higher subband. (b) Electron-hole pair annihilation through Auger recombination.

Upon photoexcitation an exciton is created in the carbon nanotube. In order to dissociate the exciton into free electrons and holes the exciton binding energy needs to be overcome. Electron-hole pair creation from exciton dissociation can occur for example with an electric field. The excitons in the carbon nanotube can also annihilate [29, 30], for example through Auger processes, before they have time to dissociate into free electrons and holes.

Bibliography

- [1] S. Iijima. Helical microtubules of graphite carbon. *Nature* **354**, 56 (1991).
- [2] S. Iijima and T. Ichihashi. Single-shell carbon nanotubes of 1-nm diameter. *Nature* **363**, 603 (1993).
- [3] D. S. Bethune *et al.* Cobalt-catalysed growth of carbon nanotubes with single-atomic-layer walls. *Nature* **363**, 605 (1993).
- [4] G. Gotz. *Single Electron-ics with Carbon Nanotubes*. Ph.D. thesis, Delft University of Technology (2010).
- [5] P. Jarillo-Herrero. *Quantum Transport in Carbon Nanotubes*. Ph.D. thesis, Delft University of Technology (2005).
- [6] E. D. Minot. *Tuning the Band Structure of Carbon Nanotubes*. Ph.D. thesis, Cornell University (2004).
- [7] M. S. Dresselhaus, G. Dresselhaus and R. Saito. Physics of carbon nanotubes. *Carbon* **33**, 883 (1995).
- [8] R. Saito, M. Fujita, G. Dresselhaus and M. S. Dresselhaus. Electronic structure of chiral graphene tubules. *Appl. Phys. Lett.* **60**, 2204 (1992).
- [9] M. S. Dresselhaus, G. Dresselhaus, R. Saito and A. Jorio. Exciton photophysics of carbon nanotubes. *Annu. Rev. Phys. Chem.* **58**, 719 (2007).
- [10] J. W. Janssen. *Spatially Resolved Spectroscopy on Carbon Nanotubes*. Ph.D. thesis, Delft University of Technology (2001).
- [11] F. Leonard. *The Physics of Carbon Nanotube Devices*. William Andrew Inc., Norwich (2009).
- [12] C. D. Spataru, S. Ismail-Beigi, L. X. Benedict and S. G. Louie. Excitonic effects and optical spectra of single-walled carbon nanotubes. *Phys. Rev. Lett.* **92**, 077402 (2004).
- [13] J. Lefebvre and P. Finnie. Excited excitonic states in single-walled carbon nanotubes. *Nano Letters* **8**, 1890 (2008).
- [14] F. Wang, G. Dukovic, L. E. Brus and T. F. Heinz. The optical resonances in carbon nanotubes arise from excitons. *Science* **308**, 838 (2005).
- [15] S. M. Sze. *Semiconductor Devices Physics and Technology*. Wiley, USA (2002).

- [16] L. Xie *et al.* Electroluminescence from suspended and on-substrate metallic single-walled carbon nanotubes. *Nano Lett.* **9**, 1747 (2009).
- [17] T. Mueller *et al.* Efficient narrow-band light emission from a single carbon nanotube p-n diode. *Nature Nanotechn.* **5**, 27 (2010).
- [18] D. Mann *et al.* Electrically driven thermal light emission from individual single-walled carbon nanotubes. *Nature Nanotechn.* **2**, 33 (2007).
- [19] C. Zhou, J. Kong, E. Yenilmez and H. J. Dai. Modulated chemical doping of individual carbon nanotubes. *Science* **290**, 1552 (2000).
- [20] Y. F. Li, R. Hatakeyama, J. Shishido, T. Kato and T. Kaneko. Air-stable p-n junction diodes based on single-walled carbon nanotubes encapsulating fe nanoparticles. *Appl. Phys. Lett.* **90**, 173127 (2007).
- [21] Y. Zhou *et al.* p-channel, n- channel thin film transistor and p-n diodes based on single wall carbon nanotube networks. *Nano Letters* **4**, 2031 (2004).
- [22] P. Avouris, M. Freitag and V. Perebeinos. Carbon-nanotube photonics and optoelectronics. *Nature Photon.* **2**, 341 (2008).
- [23] P. L. McEuen, M. S. Fuhrer and H. Park. Single-walled carbon nanotube electronics. *IEEE Trans. on Nanotechn.* **1**, 78 (2002).
- [24] C. L. Kane and E. J. Mele. Ratio problem in single carbon nanotube fluorescence spectroscopy. *Phys. Rev. Lett.* **90**, 207401 (2003).
- [25] M. J. O'Connell *et al.* Band gap fluorescence from individual single-walled carbon nanotubes. *Science* **297**, 593 (2002).
- [26] N. M. Gabor. *Extremely Efficient and Ultrafast: Electrons, Holes, and Their Interactions in the Carbon Nanotube pn Junction.* Ph.D. thesis, Cornell University (2011).
- [27] F. Wang, Y. Wu, M. S. Hybertsen and T. F. Heinz. Auger recombination of excitons in one-dimensional systems. *Phys. Rev. B* **73**, 245424 (2006).
- [28] L. Valkunas. Exciton-exciton annihilation in single-walled carbon nanotubes. *Phys. Rev. B* **73**, 115432 (2006).
- [29] K. Matsuda, T. Inoue, Y. Murakami, S. Maruyama and Y. Kanemitsu. Exciton dephasing and multiexciton recombinations in a single carbon nanotube. *Phys. Rev. B* **77**, 033406 (2008).
- [30] Y. Murakami and J. Kono. Existence of an upper limit on the density of excitons in carbon nanotubes by diffusion-limited exciton-exciton annihilation: Experiment and theory. *Phys. Rev. B* **80**, 035432 (2009).

Chapter 3

Device Fabrication and Measurement Techniques

In this chapter we describe the state-of-the-art fabrication techniques that have been used to fabricate the device structure for the carbon nanotube devices used in this thesis. The carbon nanotubes were grown in the final step of the fabrication, allowing them to stay ultra clean and free from disorder as a result of the absence of post-growth processing. This technique placed some restrictions on the device fabrication and choice of material. First the fabrication of the device structure will be outlined in detail, whereafter the growth technique of the carbon nanotubes will be discussed. Then the experimental setup used to electrically and optically characterize the individually suspended nanotubes will be described as well as the measurement techniques of photocurrent imaging and photocurrent spectroscopy will be discussed.

3.1 Fabrication of air-suspended carbon nanotube devices

The carbon nanotube devices were fabricated starting from a piece of Si wafer covered with 285 nm SiO_2 . Trench gates [1,2] were patterned using electron beam lithography followed by evaporation of 5 nm W and 25 nm Pt. The gates were 2 μm wide each and separated by 250 nm. Next, 1 μm of SiO_2 was deposited using PECVD and the oxide was thereafter etched away above the gates, creating an 800 nm deep and 2-4 μm wide trench. This left an insulating layer of SiO_2 on top of the gates. The source and drain contacts were defined on top of the SiO_2 mesas with electron beam lithography and metal evaporation (5 nm W and 25 nm Pt). A catalyst area was patterned with electron beam lithography on top of the metal contact and the catalyst solution for carbon nanotube growth was drop coated on to the sample and lifted off in hot acetone. This left a well defined area of Al_2O_3 nanoparticles and FeMo catalysts for the carbon nanotube synthesis. Each step in the fabrication will now be described in detail:

Sample cleaning

A 19 mm by 19 mm piece of Si p^{++} doped wafer with 285 nm thermal SiO_2 was used for the device fabrication. To clean the sample it was immersed for 5 minutes in HNO_3 . The beaker with HNO_3 was then placed in an ultrasonic bath. Thereafter the sample was rinsed first in H_2O and then in Iso-propanol. Finally it was blow dried with N_2 .

Gate contacts and markers

The first step is the fabrication of the buried gate structure and the e-beam markers to align the future layers to. A two layer e-beam resist is spun onto the clean sample surface. The two different resist layers react differently to the e-beam dose with the result that the bottom layer obtains a slightly larger opening than the top layer. This under-cut of the resist makes the lift off step easier. Electron beam lithography is used to pattern the gate structure, see figure 3.1a and the markers and the resist is developed and descummed (an O_2 plasma cleaning). The gate contacts are evaporated using an electron beam evaporator, as shown in figure 3.1b. A 5 nm W sticking layer is used under 25 nm Pt. Whereafter lift off is performed. The W/Pt material combination was chosen as it makes a nice p-type contact to carbon nanotubes. It is also one of the few material combinations that can sustain the 900°C carbon nanotube synthesis step without severe deformation. Unfortunately W is not an optimal sticking layer for Pt and can therefore only be used for relatively thin layers of Pt. After

evaporation, lift off was performed to remove the excess resist and metal. Leaving a well defined metallic gate structure, figure 3.1c.

Gate bond pads

It is advisable to spend the extra effort making hard bonding pads which overlap with the contacts. When wire bonding the samples it is advantageous to have a hard surface to solder the bonding wire to. If trying to wire bond to the Pt contact directly problems can occur with sticking of the soldering wire to the contact or the metal contact can peel off all together as a result of the force applied during wire bonding. To fabricate bond pads a two layer resist was spun onto the sample and patterned with e-beam lithography before being developed and descummed. The evaporation of the bond pads took place in two steps. First 10 nm Cr and 80 nm Pt was evaporated in a clean low-pressure evaporator. Thereafter the sample was moved to a dirtier evaporator for the final step. 20 nm of Si was evaporated on top of the Cr/Pt combination in order to make the bond pad extra hard. After evaporation lift off was performed. The materials will form an alloy during the final step of carbon nanotube synthesis when the sample is heated to 900°C.

Growth of oxide and etching of trench

To create the trench over which the carbon nanotubes will be suspended a 1 μm thick layer of SiO_2 was deposited, figure 3.1d, using plasma-enhanced-chemical-vapour-deposition (PECVD). After the deposition of the SiO_2 a two layer resist was spun on the sample, patterned with e-beam lithography, developed and descummed, see figure 3.1e. An 80 nm thick Al mask was evaporated on the source/drain contact regions, as shown in figure 3.1f, followed by lift off. Figure 3.1g shows the plasma etching which was performed to etch away ~ 800 nm of the deposited SiO_2 everywhere except at the source/drain contact regions. This left a ~ 200 nm thick insulating layer of SiO_2 on top of the gate electrodes at the bottom of the trench. The reason for this insulating layer is if the suspended nanotube obtains a bit of slack and touches the bottom of the trench, it should not short the electrical circuit. After the plasma etching the sample is placed in an Al etch to remove the remains of the Al etch mask, as seen in figure 3.1h. The result of the two etch steps is checked with a stepper.

Gate bond pads

After the deposition and etching of the SiO_2 layer a ~ 200 nm thick layer of SiO_2 remains on top of the gate bond pads. In order to remove this layer from the bond pads, a resist is spun on the sample and patterned with e-beam lithography and

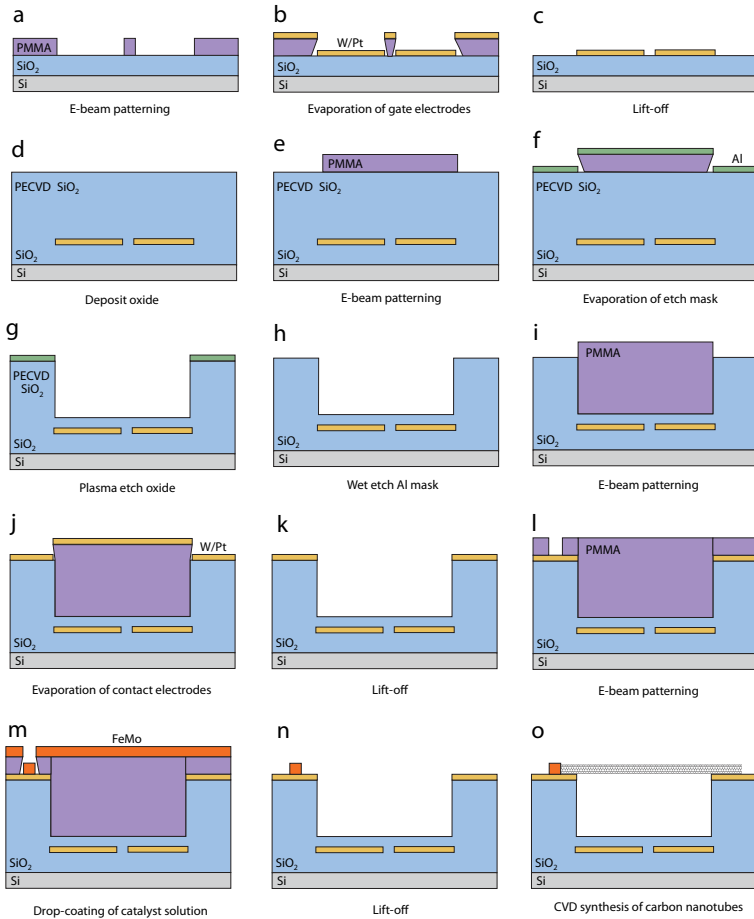


Figure 3.1: Device fabrication scheme. (a) Patterning of pmma with e-beam lithography. (b) Develop pmma and evaporate W/Pt. (c) Lift-off. Gate electrodes are created. (d) Deposit 1 μm of PECVD SiO₂. (e) Spin pmma and pattern with e-beam lithography. (f) Develop pmma and evaporate Al as an etch mask. (g) Lift-off and plasma etch of the PECVD SiO₂ to create the trench. A thin layer of oxide is left on top of the gate structure. (h) Strip the Al mask with a wet etch. (i) Spin pmma and pattern with e-beam lithography. (j) Develop pmma and evaporate W/Pt. (k) Lift-off. Source and drain electrodes created. (l) Spin pmma and pattern with e-beam lithography. (m) Develop and drop coat FeMo catalyst solution. (n) Lift-off. Catalyst islands created. (o) Grow carbon nanotubes from FeMo catalysts using CVD.

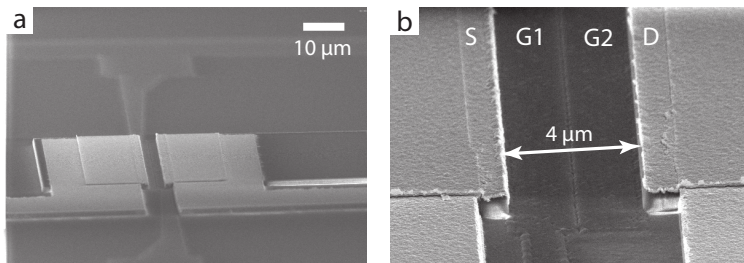


Figure 3.2: Scanning electron micrograph of the device structure. (a) SEM image of the source and drain electrodes and the two buried gates. The scale bar is 10 μm . (b) Close up image of the trench. The source and drain electrodes are separated by the 4 μm trench, and the two gate electrodes can be seen at the bottom of the trench.

then developed and descummed. This leaves an exposed area immediately above the gate bond pads. The sample is now immersed in buffered HF for etching of the SiO_2 above the gate bond pads. After the etch the resist is striped in hot acetone.

Source/drain contacts

Source and drain metal contacts were fabricated on top of the 800 nm tall SiO_2 mesas that resulted from the etching of the trench. The sample was spun with a resist layer, patterned with e-beam lithography, developed and descummed. 5 nm of W and 25 nm of Pt was evaporated for the electrodes, followed by lift off. The process is illustrated in figure 3.1i-k.

Source/drain bond pads

The bond pads for the source and drain contacts were fabricated the same way as the bond pads for the gate electrodes (see above). Figure 3.2 shows a scanning electron micrograph (SEM) image of the completed device structure.

Catalyst deposition

When growing the carbon nanotubes it is important to control the position and density of nanotubes. To do that we pattern a 2 μm by 2 μm area on top of the Pt source electrode. The patterning is done by spinning, writing, developing and descumming a resist using e-beam lithography, figure 3.1l. Our catalyst solution contains aluminum oxide (Al_2O_3) nanoparticles with iron(III) nitrate

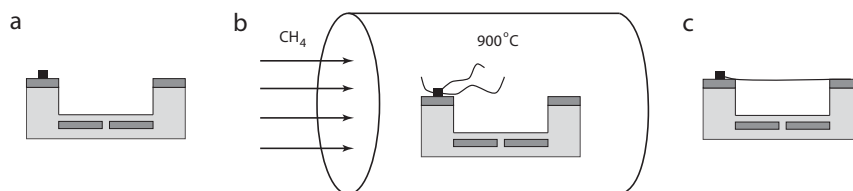


Figure 3.3: Carbon nanotube synthesis. (a) Fabricated sample with device structure. (b) The sample is placed in a CVD furnace and heated up to 900°C . The CH_4 precursor is decomposed by the catalyst and carbon nanotubes start to form from the catalyst site. (c) One of the carbon nanotubes fall across the trench and makes an electrical contact between the electrodes.

nonhydrate ($\text{Fe}(\text{NO}_3)_3 \cdot 9\text{H}_2\text{O}$) and molybdenum dioxide (MoO_2). One drop of the catalyst solution was drop coated on top of the patterned sample and baked for 10 minutes at 150°C , figure 3.1m. Lift off was performed in hot acetone in gentle ultrasound, resulting in figure 3.1n. Before carbon nanotube growth the sample and the catalysts were exposed to a thorough O_2 plasma cleaning.

3.2 Carbon nanotube synthesis

The carbon nanotubes were synthesized using chemical vapour deposition (CVD). A quartz tube was placed in a furnace and was first baked out at 900°C in air for 1-2 hours. Thereafter the sample with fabricated devices was placed inside the quartz tube and the system was heated up to 900°C under Ar flow. Figure 3.3 shows an overview of the carbon nanotube growth process. When the desired temperature was reached the Ar gas was turned off and CH_4 and H_2 gases were introduced into the quartz tube. The CH_4 carbon feedstock is decomposed by the FeMo catalyst particles and a carbon nanotube can be synthesized starting from the catalyst particle. During the growth the carbon nanotubes extends across the pre-defined trench and lands on the surface of the metal electrode on the opposite side. The carbon nanotube growth last a total of 10 minutes, after which the CH_4 gas was turned off and the sample was cooled down under H_2 and Ar gas flow. The continuous flow of H_2 while cooling down prevents formation of amorphous carbon on the sample. When the system has cooled down below 180°C the H_2 and Ar gases are turned off and the sample is removed from the quartz tube. This growth method is known to produce single-walled carbon nanotubes in the diameter range from approximately 1.2 - 4 nm [3]. A grown carbon nanotube suspended between the two metal electrodes can be seen in figure 3.4.

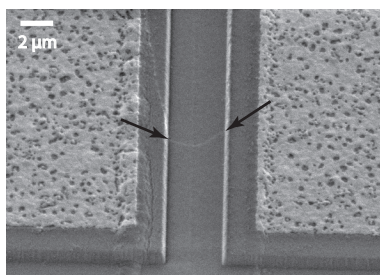


Figure 3.4: Suspended carbon nanotube. The nanotube has fallen across the trench during the growth process. The scale bar is $2\ \mu\text{m}$.

3.3 Experimental Setup

The optical experiments were performed in a homebuild scanning confocal microscope setup. The sample was loaded on an attocube piezo positioner stage in a Janis cryostat. The attocube stage allowed for very precise positional adjustments in the x,y and z directions. The cryostat could be cooled, using liquid helium, to 4 K and was also equipped with a Lakeshore temperature controller for temperature dependent measurements. The majority of the experiments in this thesis, however, was performed at room temperature, where the cryostat was used as a vacuum chamber. An Olympus IR coated objective was mounted on the inside of the lid of the cryostat. The objective had a NA of 0.8 and a working distance of 3 mm.

The telecentric system was build on a second level above the cryostat. Figure 3.5 shows a schematic illustration of the measurement setup and figure 3.6 shows a picture of the actual laboratory setup. The incoming excitation laser (can be fiber coupled or free space) enters a beamsplitter which could be varied between 50/50 or 90/10 depending on the experimental requirements. The laser thereafter enters the computer controlled scanning galvo mirrors. After the galvo mirrors the laser beam goes through two lenses before it enters the cryostat and the objective. Using the galvo mirrors the focused beam can be scanned across the sample surface. The reflected light from the sample returns through the same path until the beamsplitter, where it is directed to a Si photodiode. For white light imaging a pellicle beamsplitter can be flipped in immediately before the cryostat window. The white light image is detected with a sensitive CCD camera.

For basic measurements a green laser (532 nm) was used for excitation. The green laser has a energy of 2.33 eV which is much larger than the bandgap of our carbon nanotubes. For excitation close to the carbon nanotube bandgap a

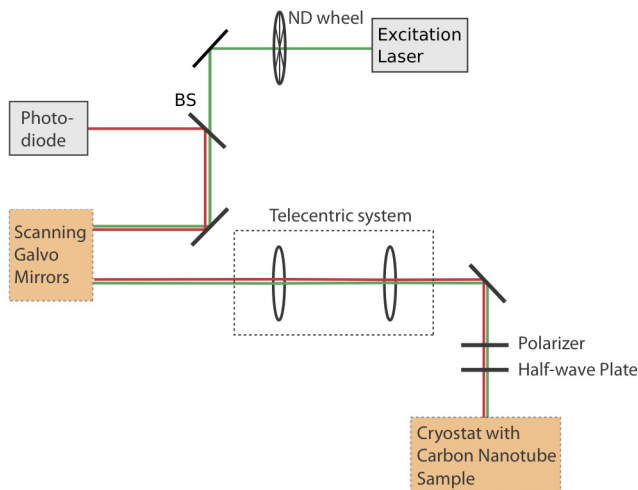


Figure 3.5: Schematic of measurement setup. Room temperature photocurrent setup. The excitation light (indicated in green) enters the setup and goes through a beam splitter and the computer controlled galvo mirrors. The telecentric system is used to translate the beam position on the sample surface. Right before the cryostat the polarization of the laser is adjusted (if applicable) before it enters the cryostat with the objective on the inside of the lid and excites the sample. The reflected light (indicated in red) follows the same path through the setup and after the beam splitter it is detected by a Si photodiode.

Fianium supercontinuum white light source, pulsed at 20 MHz, was used. The Fianium was coupled to an acousto-optic tunable filter (AOTF) which generated a collimated laser beam for wavelengths between 650 and 1100 nm with 5 nm bandwidth (crystal 1) and between 1100 and 2000 nm with 7 nm bandwidth (crystal 2).

3.4 Photocurrent imaging and spectroscopy

The suspended carbon nanotube devices were characterized by scanning the laser beam across a defined area of the sample [2, 4] by means of two computer-controlled scanning mirrors.

In photocurrent imaging the reflected light from the sample structure was collected by a photodiode, generating a reflection image of the sample, see figure 3.7a. Simultaneously the current through the carbon nanotube was mea-

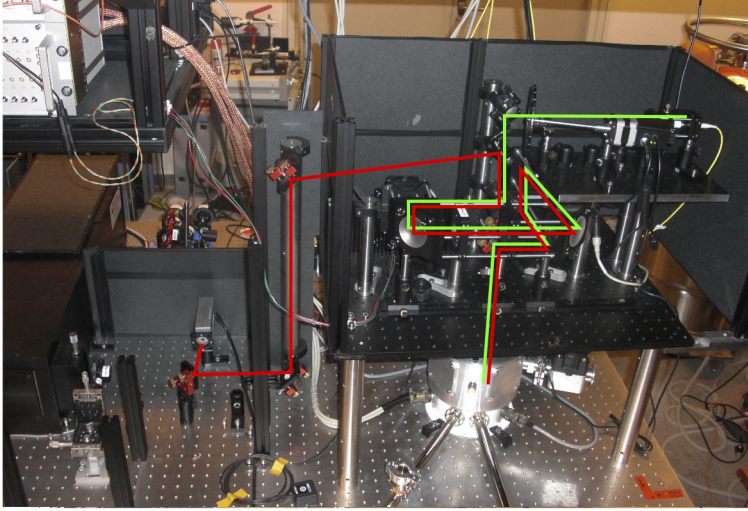


Figure 3.6: Measurement setup. A picture of the measure setup. The sample is placed in the cryostat at the bottom, which has optical access from the top. The objective is positioned on the inside of the lid of the cryostat. The excitation laser (green) goes through a pair of computer controlled galvo-mirrors, used to scan the laser spot across the sample. The reflected light (red) goes through the same optical path and is eventually reflected by the beam splitter and collected by the photodiode.

sured for every laser coordinate, generating a photocurrent image, figure 3.7b. The reflection and photocurrent images were superimposed creating the image in figure 3.7c of spatial photocurrent response in relation to the metallic device structure.

In photocurrent spectroscopy [5–7] the supercontinuum laser is positioned on the carbon nanotube p-n junction (coordinates found through photocurrent imaging, see figure 3.7c) and the frequency of the laser is tuned within the allowed ranges for each AOTF crystal. The photocurrent from the carbon nanotube p-n junction is recorded as a function of laser frequency, generating a spectral photocurrent response. Performing photocurrent spectroscopy allows for resolving the van Hove singularities in the joint-density-of-states in the carbon nanotube.

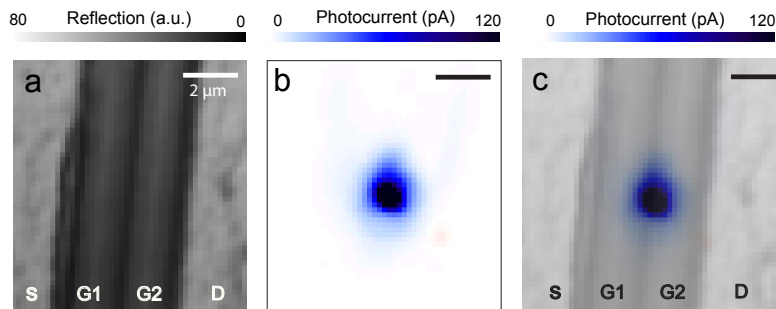


Figure 3.7: Scanning photocurrent microscopy. (a) A reflection image outlining the device structure. The source, drain and gate contacts have been indicated for clarity. (b) A photocurrent image showing the spatial photocurrent response as the laser spot is scanned over the device area. (c) The reflection image from (a) and the photocurrent image from (b) can be superimposed, generating an image of photocurrent response in relation to the device structure. All scale bars are $2\mu\text{m}$.

Bibliography

- [1] G. A. Steele, G. Gotz and L. P. Kouwenhoven. Tunable few-electron double quantum dots and klein tunneling in ultraclean carbon nanotubes. *Nature Nanotech.* **4**, 363 (2009).
- [2] G. Buchs, M. Barkelid, S. Bagiante, G. A. Steele and V. Zwiller. Imaging the formation of a p-n junction in a suspended carbon nanotube with scanning photocurrent microscopy. *J. Appl. Phys.* **110**, 074308 (2011).
- [3] J. Kong, H. T. Soh, A. M. Cassell, C. F. Quate and H. Dai. Synthesis of individual single-walled carbon nanotubes on patterned silicon wafers. *Nature* **395**, 878 (1998).
- [4] K. Balasubramanian, M. Burghard, K. Kern, M. Scolari and A. Mews. Photocurrent imaging of charge transport barriers in carbon nanotube devices. *Nano Lett.* **5**, 507 (2005).
- [5] J. U. Lee, P. J. Codella and M. Pietrykowski. Direct probe of excitonic and continuum transitions in the photocurrent spectroscopy of individual carbon nanotube p-n diodes. *Appl. Phys. Lett.* **90**, 053103 (2007).
- [6] M. Barkelid, G. A. Steele and V. Zwiller. Probing optical transitions in individual carbon nanotubes using polarized photocurrent spectroscopy. *Nano Lett.* **12**, 5649 (2012).
- [7] M. Freitag, Y. Martin, J. A. Misewich, R. Martel and P. H. Avouris. Photoconductivity of single carbon nanotubes. *Nano Lett.* **3**, 1067 (2003).

Chapter 4

Imaging the Formation of a p-n Junction in a Suspended Carbon Nanotube with Scanning Photocurrent Microscopy

Gilles Buchs, Maria Barkelid, Salvatore Bagiante, Gary A. Steele and Val Zwiller

We use scanning photocurrent microscopy (SPCM) to investigate individual suspended semiconducting carbon nanotube devices where the potential profile is engineered by means of local gates. In situ tunable p-n junctions can be generated at any position along the nanotube axis. Combining SPCM with transport measurements allows a detailed microscopic study of the evolution of the band profiles as a function of the gates voltage. Here we study the emergence of a p-n and a n-p junctions out of a n-type transistor channel using two local gates. In both cases the I - V curves recorded for gate configurations corresponding to the formation of the p-n or n-p junction in the SPCM measurements reveal a clear transition from resistive to rectification regimes. The rectification curves can be fitted well to the Shockley diode model with a series resistor and reveal a clear ideal diode behavior. ¹

¹This chapter has been published in *Journal of Applied Physics* **110**, 074308 (2011).

4.1 Introduction

The unique electronic properties of carbon nanotubes make them ideal systems for future large-scale integrated nanoelectronics circuits [1]. Due to their quasi-one-dimensional geometry, the electronic bands of carbon nanotubes can be engineered by means of electrostatic doping. In this context, p-n junction diodes [2–7] as well as tunable double quantum dots working in the single particle regime have been realized in suspended nanotube devices using local gates [8]. High spatial control and resolution of the electrostatic doping of semiconducting nanotubes will allow the realization of electronic and optoelectronic devices like diodes or phototransistors [9] with tunable properties, which is not possible for devices based on chemically doped semiconductors. Moreover, a controlled confinement of single carriers in combination with a p-n junction [10] in a semiconducting nanotube could potentially enable future applications such as electrically driven single photon sources in the burgeoning field of carbon nanotube quantum optics [11]. Here we report on a scanning photocurrent microscopy (SPCM) study of suspended semiconducting nanotube devices where the band profile is engineered by means of local gates in order to generate p-n junctions at controlled locations along the nanotube axis.

4.2 Experimental Setup

The devices consist of a nanotube grown between platinum electrodes over pre-defined trenches with a depth of $1\ \mu\text{m}$ and widths of 3 or $4\ \mu\text{m}$. Up to four gates are defined at the bottom of the trenches. A schematic and a scanning electron microscopy image of a typical device with four gates and a $3\ \mu\text{m}$ wide trench are shown in Figs. 4.1a and 4.1b, respectively. The fabrication began with a p^{++} silicon wafer used as a backgate covered by $285\ \text{nm}$ of thermal silicon oxide. On top of this, gate electrodes made of $5/25\ \text{nm}$ W/Pt were defined using electron-beam lithography, followed by the deposition of a $1100\ \text{nm}$ thick SiO_2 layer. A $1000\ \text{nm}$ deep trench was dry etched, leaving a thin oxide layer on top of the gates. A $5/25\ \text{nm}$ W/Pt layer was then deposited to serve as source and drain contacts, and nanotubes were grown at the last fabrication step at a temperature of 900°C from patterned Mo/Fe catalysts [8, 12]. In SPCM, photocurrent (PC) is recorded as a laser spot is scanned across a sample. PC appears when photo-generated electrons and holes are separated by local electric fields in the device, such as those present at metal/nanotube interfaces [13, 14], defect sites [14], or p-n junctions [5]. Our SPCM setup consists of a confocal microscope with a $\text{NA} = 0.8$ objective illuminated by a $\lambda = 532\ \text{nm}$ laser beam. The diffraction limited spot is scanned using a combination of two galvomirrors and a telecentric

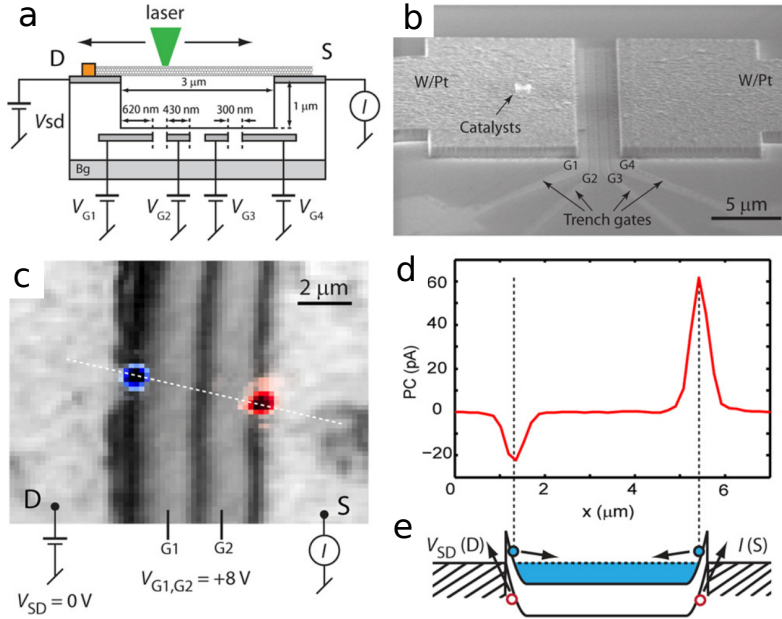


Figure 4.1: (a) Schematic of a device with four trench gates G1-G4. A diffraction-limited laser spot ($\lambda = 532$ nm) is scanned across the device and PC is recorded between source (S) and drain (D) contacts. (b) Scanning electron microscope image of a four trench gates device. (c) Superimposition of the PC image and the reflection image for a device with two trench gates separated by 250 nm, measured with $V_{G1} = V_{G2} = \pm 8$ V and $V_{SD} = 0$ V. A single semiconducting nanotube is highlighted with a dashed line. (d) PC line profile recorded along the dashed line in panel (c) corresponding to the nanotube axis. (e) Corresponding band diagram with photogenerated carrier separation at the metal/nanotube interfaces.

lens system while the dc PC signal and the reflected light intensity are recorded simultaneously in order to determine the absolute position of the detected PC features. Typical light intensities of 3 kW/cm^2 are used in this work.

4.3 Scanning Photocurrent Microscopy of a Tunable p-n Junction

Figure 4.1c shows the superimposition of the PC and reflection images of a device with two gates labeled G1 and G2 separated by 250 nm in a $4 \mu\text{m}$ wide trench, measured in vacuum ($\approx 10^{-4}$ mbar) at room temperature. The applied

voltages are $V_{G1} = V_{G2} = +8$ V and $V_{SD} = 0$ V. The PC image in combination with the measured transfer characteristics reveal the presence of a single semiconducting nanotube crossing the trench, whose axis is indicated by a dashed line. Figure 4.1d shows the PC line profile recorded along the dashed line in panel c with two PC spots at the edge of the trench revealing the local electric field generated at the metal/nanotube interface. The corresponding band diagram is depicted in e with an illustration of the photogenerated carrier separation at the contacts. The asymmetry in the PC is due to different resistances for carriers at the source and drain contacts, for instance here a thinner Schottky barrier for electrons at the drain contact (D) [13]. In Fig. 4.2, we demonstrate the imaging of a p-n junction, whose position and polarity can be tuned with the local gates. We use a four trench gate device similar to the one shown in Fig. 4.1b. The measurements are performed at room temperature in air. With the same potential applied to all four gates, two PC spots appear at the trench edges with polarities depending on the gates potential, similar to those shown for the two gate device in Fig. 4.1c. For opposite potentials ($+8$ V/ -8 V) applied to groups of adjacent gates with configurations G1-G2, G3-G4 (panel (a)), G1-G2-G3, G4 (panel b), and G1, G2-G3-G4 (panel c), p-n junctions are created and clear PC spots appear at the electric field maxima corresponding to depletion regions. The images demonstrate that we can both move the position of the p-n junction and change its polarity using the local gates. Note that the metal/nanotube interface does not show PC signals due to the potential barrier formed at the depletion region that blocks one of the photogenerated carriers, as illustrated in panel d. The patterns around the maximum intensity PC spots are due to diffraction effects from the structure of the gates. Gaussian fits to the PC signals along the nanotube axis (dashed lines) show that the center of the depletion regions is positioned close to the center of the spacing between two gates with opposite potentials.

4.4 Imaging the Formation of a p-n Junction

In Fig. 4.3 we study a two trench gates device illustrated in the schematic in Fig. 4.3a ($4 \mu\text{m}$ wide trench and gate separation 250 nm). The measurements have been performed at room temperature in vacuum. A single semiconducting nanotube was found to cross the trench establishing an electrical contact between source and drain electrodes. Using the technique described in Refs. [13] and [15], we estimate the bandgap to be $E_g \approx 400$ meV, corresponding to a diameter of about 1.7 nm [16], and we find that the Fermi level at the contacts lies at about one third of the bandgap below the conduction band. A transition from a fully n-type or n-n channel to p-n (n-p) configuration is studied in panels a-c (d-f) by applying a constant potential of $+8$ V to G2 (G1) and sweeping G1 (G2) from $+8$ V to -8 V. For each value of V_{G1} (V_{G2}), the laser spot is scanned along the

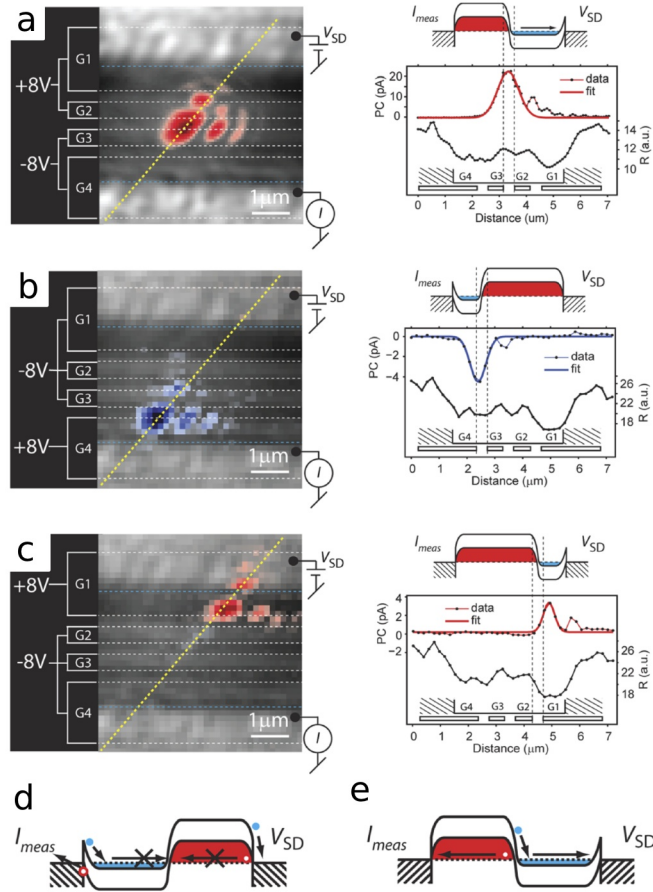


Figure 4.2: Tuning the position and polarity of a p-n junction using local gates. (a)-(c) Left column: Superimposition of the PC and reflection images and the configurations of the potentials applied to the trench gates. The dashed line corresponds to the nanotube axis. Right column: Corresponding band diagrams with PC and reflection intensities (R) recorded along the dashed line as well as the position of the gates. Each PC line profile is fitted with a Gaussian discarding the diffraction-induced patterns. (d)-(e) Band diagrams illustrating the behavior of the photogenerated carriers at different positions: metal/nanotube interfaces and depletion region, respectively.

nanotube axis and the PC is recorded, Fig. 4.3b (Fig. 4.3e). For the range V_{G1} (V_{G2}) > 0 V, the PC shows two contributions at the Schottky barriers. Below 0 V the negative (positive) PC signal starts to move its position toward the center of the trench and the positive (negative) PC signal vanishes. Both effects are due to a transition of the band profile from pure n-n to the configuration depicted with the label i-n (n-i) where the drain (D) (source (S)) side of the n channel begins to pinch off and prevents electrons generated at the source (S) (drain (D)) Schottky barrier from reaching the drain (source) contact. The negative (positive) PC signal continues to move into the trench until it is suppressed below $V_{G1} = -1$ V ($V_{G2} = -0.8$ V) and then recovers around $V_{G1} = -3$ V ($V_{G2} = -2$ V). This low PC intensity likely indicates a shallow potential profile in which the electric field is not large enough to separate the photogenerated carriers. At $V_{G1} \approx -3$ V ($V_{G2} \approx -2.5$ V), the PC signal increases drastically up to about -22 pA (30 pA) and shifts slowly toward the center of the trench at V_{G1} (V_{G2}) = -8 V. This strong PC signal is the consequence of hole doping of the drain (source) side of the device, resulting in a p-n (n-p) junction with a large electric field in its depletion region, depicted in the band diagram corresponding to $V_{G1}(V_{G2}) = -8$ V in panel (b) (panel (e)). In addition to PC imaging, we also perform I - V measurements (dark current) for values of V_{G1} (V_{G2}) indicated by labels 1-7 (1'-6') in panel (b) (panel (e)). A progression from ohmic regime at V_{G1} (V_{G2}) = +8 V with a measured resistance of about 40 M Ω (68 M Ω) to a clear rectification behavior starting below V_{G1} (V_{G2}) = -2 V corresponding to I - V curves 4-7 (4'-6') with the forward current increasing with $|V_{G1}|$ ($|V_{G2}|$) is observed. The rectification curves 4-7 (4'-6') can be fitted well to the Shockley diode model $I = I_0(e^{V_{SD}/n \cdot V_T} - 1)$ with a series resistor [3],

$$I = I_0 \left[\frac{nV_T}{I_0 R} W \left(\frac{I_0 R}{nV_T} e^{\frac{V_{SD} + I_0 R}{nV_T}} \right) - 1 \right] \quad (4.1)$$

where I_0 is the saturation current at reverse bias, n is the ideality factor, V_T is the room temperature thermal voltage of 26 mV, R is the series resistance, W is the Lambert W-function, and V_{SD} is the source-drain voltage. For a measured saturation current of about $I_0 = 4 \times 10^{-13}$ A ($I_0 = 4 \times 10^{-13}$ A), we find the best fit with $n = 1$ and $R_4 = 25$ G Ω , $R_5 = 2$ G Ω , $R_6 = 690$ M Ω , and $R_7 = 200$ M Ω ($R_4' = 25$ G Ω , $R_5' = 4$ G Ω , and $R_6\Omega = 1.2$ G Ω). The decreasing value of R with $|V_{G1}|$ ($|V_{G2}|$) is in good agreement with the band profiles model depicted on the right side of panel b (panel e), implying a decrease in width of the tunneling barrier for hole injection in the segment of the nanotube located above $G1$ ($G2$) when $|V_{G1}|$ ($|V_{G2}|$) increases. The higher current in forward bias for the p-n configuration compared to n-p is due to an asymmetry in the resistance at the source and drain contacts. We note that the estimated bandgap from the turn-on voltage ($V_{SD} \approx 150$ mV) is not consistent with the value estimated from the

transfer characteristic ($E_g \approx 400$ mV). In addition to the systematic error from the estimation of the bandgap from the transfer characteristic using the method of Refs. [13] and [15], this difference can also potentially be due to diffusion effects for the carriers, recently observed by another group [7]. Such discrepancies in our devices will be the subject of future investigations.

4.5 Conslusions

In summary, we have demonstrated the control of the position and polarity of a p-n junction in multigate suspended carbon nanotube devices. We created a p-n junction from a purely n-type channel and imaged its formation using SPCM. In the electrical characteristics, a corresponding transition is observed from the linear resistance of a transistor channel to the non-linear rectification of an ideal diode. The high degree of control of ideal p-n junctions using the local gates, combined with the precise photocurrent imaging of the p-n junction position, demonstrate the potential of carbon nanotubes and the SPCM technique in optoelectronics applications.

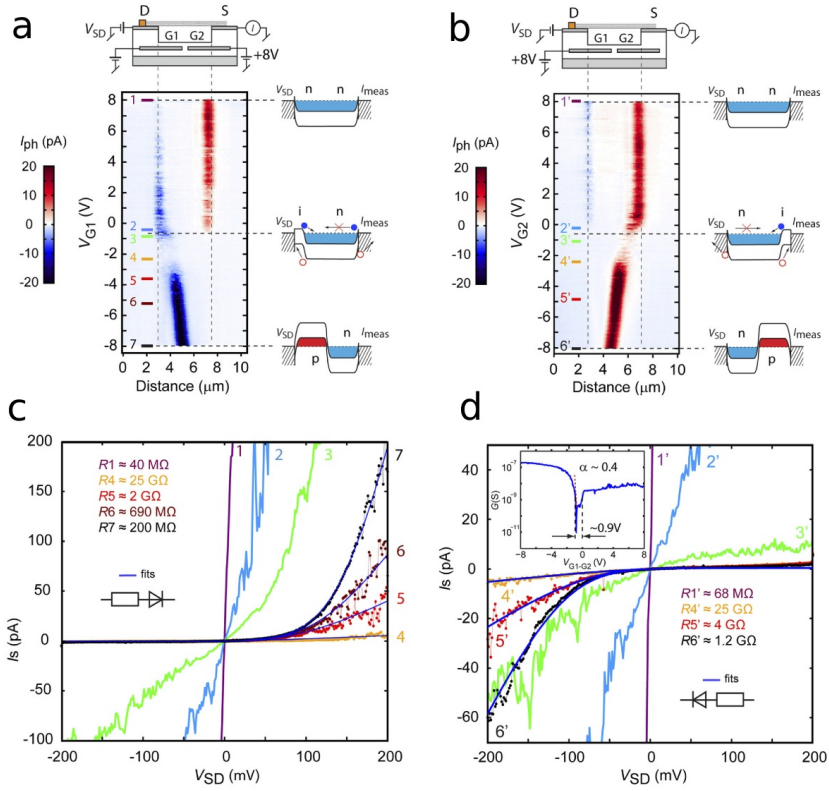


Figure 4.3: Imaging the emergence of a p-n junction. (a) Schematic of a device with two trench gates. G2 is set to ± 8 V and G1 is swept. (b) PC transition map recorded along the nanotube axis, with corresponding band diagrams for n-n, i-n, and p-n regimes. (c) I - V curves recorded at values of V_{G1} labeled 1-7 in (b). Inset: Values of the series resistances R1 for the linear n-n regime and R4-R7 for the rectification regime fitted with the Shockley diode model. (d) G1 is set to ± 8 V and G2 is swept. (e) PC transition map recorded along the nanotube axis, with corresponding band diagrams for n-n, n-i, and n-p regimes. (f) I - V curves recorded at values of V_{G2} labeled 1'-6' in (e). Inset bottom right: Values of the series resistances R1' for the linear n-n regime and R4'-R6' for the rectification regime fitted with the Shockley diode model. Inset up left: Transfer characteristics of the device, where V_{G1}/V_{G2} corresponds to the voltage applied simultaneously to G1 and G2. α is the estimated gate efficiency.

Bibliography

- [1] J.-C. Charlier, X. Blase and S. Roche. Electronic and transport properties of nanotubes. *Rev. Mod. Phys.* **79**, 677 (2007).
- [2] J. U. Lee, P. P. Gipp and C. M. Heller. Carbon nanotube p-n junction diodes. *Appl. Phys. Lett.* **85**, 145 (2004).
- [3] J. U. Lee. Photovoltaic effect in ideal carbon nanotube diodes. *Appl. Phys. Lett.* **87**, 073101 (2005).
- [4] K. Bosnick, N. M. Gabor and P. L. McEuen. Transport in carbon nanotube p-i-n diodes. *Appl. Phys. Lett.* **89**, 163121 (2006).
- [5] N. M. Gabor, Z. Zhong, K. Bosnick, J. Park and P. L. McEuen. Extremely efficient multiple electron-hole pair generation in carbon nanotube photodiodes. *Science* **325**, 1367 (2009).
- [6] T. Mueller *et al.* Efficient narrow-band light emission from a single carbon nanotube p-n diode. *Nature Nanotechn.* **5**, 27 (2010).
- [7] C.-H. Liu, C.-C. Wu and Z. Zhong. A fully tunable single-walled carbon nanotube diode. *Nano Lett.* **11**, 1782 (2011).
- [8] G. A. Steele, G. Gotz and L. P. Kouwenhoven. Tunable few-electron double quantum dots and klein tunneling in ultraclean carbon nanotubes. *Nature Nanotechn.* **4**, 363 (2009).
- [9] S. M. Sze. *Physics of Semiconductor Devices*. John Wiley and Sons, New York (1981).
- [10] A. Imamoglu and Y. Yamamoto. Nonclassical light generation by coulomb blockade of resonant tunneling. *Phys. Rev. B* **46**, 15982 (1992).
- [11] A. Hogele, C. Galland, M. Winger and A. Imamoglu. Photon antibunching in the photoluminescence spectra of a single carbon nanotube. *Phys. Rev. Lett.* **100**, 217401 (2008).
- [12] J. Kong, H. T. Soh, A. M. Cassell, C. F. Quate and H. Dai. Synthesis of individual single-walled carbon nanotubes on patterned silicon wafers. *Nature* **395**, 878 (1998).
- [13] Y. H. Ahn, A. W. Tsen, B. Kim, Y. W. Park and J. Park. Photocurrent imaging of p-n junctions in ambipolar carbon nanotube transistors. *Nano Lett.* **7**, 3320 (2007).

- [14] K. Balasubramanian, M. Burghard, K. Kern, M. Scolari and A. Mews. Photocurrent imaging of charge transport barriers in carbon nanotube devices. *Nano Lett.* **5**, 507 (2005).
- [15] S. Rosenblatt *et al.* High performance electrolyte gated carbon nanotube transistors. *Nano Lett.* **2**, 869 (2002).
- [16] T. W. Odom, J. L. Huang, P. Kim and C. M. Lieber. Atomic structure and electronic properties of single-walled carbon nanotubes. *Nature* **391**, 62 (1998).

Chapter 5

Probing Optical Transitions in Individual Carbon Nanotubes using Polarized Photocurrent Spectroscopy

Maria Barkelid, Gary A. Steele, Val Zwiller

Carbon nanotubes show vast potential to be used as building blocks for photodetection applications. However, measurements of fundamental optical properties, such as the absorption coefficient and the dielectric constant, has not been accurately performed on a single pristine carbon nanotube. Here we show polarization dependent photocurrent spectroscopy, performed on a p-n junction in a single suspended semiconducting carbon nanotube. We observe an enhanced absorption in the carbon nanotube optical resonances and an external quantum efficiency of 12.3 % and 8.7 % was deduced for the E11 and E22 transitions, respectively. By studying the polarization dependence of the photocurrent a dielectric constant of 3.6 ± 0.2 was experimentally determined for this semiconducting carbon nanotube. ¹

¹This chapter has been published in *Nano Letters* **12**, 5649-5653 (2012).

5.1 Introduction

Carbon nanotubes show attractive optical [1, 2] properties as a direct result of their quasi-one-dimensional geometry. This has triggered an active interest in developing carbon nanotubes for optoelectronic device applications [3], such as diodes [4, 5] and photodetectors [6]. For advanced device design a detailed knowledge about the fundamental physical properties of the system is required. Previous studies have already demonstrated a direct band gap and large exciton binding energies in carbon nanotubes [7]. Optical resonances in the joint density of states arise as a direct result of the quantized nature of the k-vector in the circumferential direction of the carbon nanotube. Optical absorption have been previously reported for carbon nanotube films [7–9], nanotubes in solution [10] and nanotubes confined in zeolite channels [11], but quantitative measurements of the absorption coefficient for an individual carbon nanotube without environmental influence has not been reported.

Here we show polarization dependence of photocurrent spectroscopy measurements [12, 13] on a single semiconducting carbon nanotube p-n junction. Using polarization, resonances of the same or of different indices can be separately addressed [7, 8, 14–16]. We use this polarization dependence to probe the E11 and E22 optical transitions [17] and study the enhanced absorption in these optical resonances. We obtain a quantitative number for the quantum efficiency and attribute this to a lower limit for the absorption coefficient in this semiconducting carbon nanotube, something which has not been previously reported for a single clean nanotube. In addition we obtain a value for the dielectric constant through experimental measurements. This property of a carbon nanotube has been theoretically predicted and is commonly used as a fitting parameter, however to the authors' best knowledge no experimental measurement has been reported for this parameter on a single nanotube level.

5.2 Device characterization

For this work we fabricated electrically contacted individual semiconducting carbon nanotubes. The nanotubes were synthesized using chemical vapor deposition [18] on a pre-fabricated device structure [19]. Growing the nanotubes in the final fabrication step ensured a pristine system for the photocurrent study. Figure 5.1a illustrates the carbon nanotube bridging a 4 μm wide trench in between two W/Pt contacts. In the bottom of the 800 nm deep trench two buried W/Pt trench gates were defined, separated by 250 nm. More information about the device fabrication can be found in the methods section. The local gate structure was used to engineer the potential landscape of the carbon nanotube [4, 19, 20].

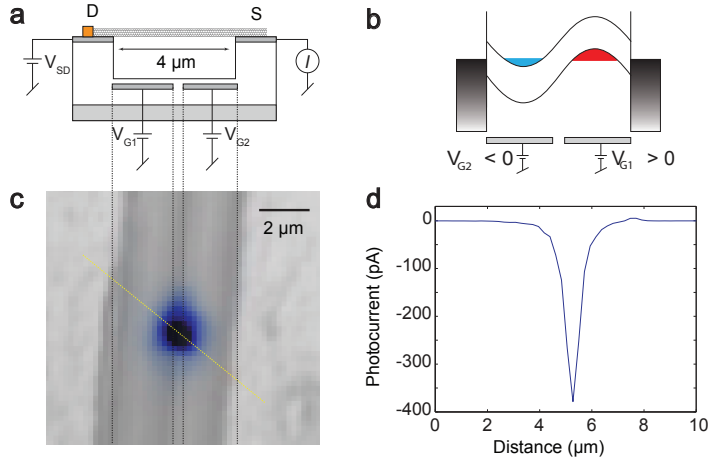


Figure 5.1: Photocurrent imaging of a suspended carbon nanotube. (a) Device schematic. The nanotube is suspended between two metal contacts, and the device structure contains two trench gates. (b) Schematic of the electrostatic potential of the gate-defined p-n junction. (c) Photocurrent imaging of the p-n junction, determining the location of the maximum electric field to be in the center of the trench. (d) Line profile of the photocurrent along the yellow dashed line in (c) showing the magnitude of the photocurrent signal.

The nanotube device is subject to electrostatic doping, accomplished by applying voltage to the trench gates. Voltage of opposite polarity applied to the two trench gates realizes a p-n junction in the carbon nanotube. Figure 5.1b shows a schematic of the electrostatic potential for the p-n junction.

The p-n junction was characterized at room temperature, under vacuum, using scanning photocurrent microscopy [21–24] ($\lambda = 532$ nm, power = 1.45 kW/cm²). Figure 5.1c shows a scanning photocurrent image of the carbon nanotube p-n junction (color) superimposed on a reflection image (gray) where the metallic contacts and gate structure are visible. The photocurrent image in figure 5.1c provides spatial information about the electric field in the depletion region. This shows that the photocurrent response indeed originates from the p-n junction which is formed in between the two trench gates. In figure 5.1d the corresponding line profile of the photocurrent image (along the yellow dashed line in figure 5.1c), indicates the magnitude of the photocurrent response. The full-width at half-max of the photocurrent peak measures 660 nm, which is close to our diffraction limited laser spot diameter.

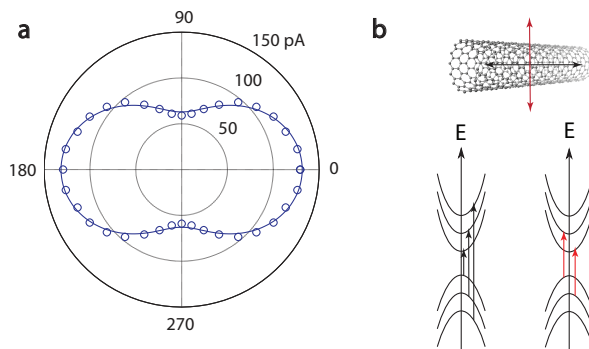


Figure 5.2: Effect of polarized light on a carbon nanotube. (a) The depolarization effect. Photocurrent measurements were performed at 1064 nm as a function of polarization angle of the incident laser light. The photocurrent is displayed in units of pA. (b) Nanotube selection rules, where light polarized parallel to the nanotube axis probes transitions between subbands of the same index and light polarized perpendicular to the nanotube axis addresses transitions between subbands whose index differ by 1.

5.3 Polarization dependence

We now position our laser on the p-n junction and study the effect of polarization on the photocurrent response of our nanotube device. When the excitation laser is polarized two effects are present in the carbon nanotube. One is the depolarization effect, displayed in figure 5.2a. The measured polarization dependence of the photocurrent, collected at 1064 nm (0.91 kW/cm^2) demonstrates the polarizability of our carbon nanotube [25]. This effect arises from the one-dimensional geometry of the carbon nanotube. It results in a smaller part of the incident electric field coupling in to the carbon nanotube for cross-polarized light.

The second effect that appears for polarized excitation of a carbon nanotube originates from the optical selection rules, schematically illustrated in figure 5.2b. Consider the matrix element for an optical transition E_{ij} , as predicted by Ajiki and Ando [25,26], for light polarized parallel to the nanotube axis optical transitions take place between subbands of the same index ($i=j$), which has the same symmetry for the electron wavefunction. For light polarized perpendicular to the nanotube axis the angular momentum operator changes the quantum number j by one unit. Thus, the allowed optical transitions occur between subbands whose index differs by 1.

5.4 Extracting the dielectric constant of a semi-conducting carbon nanotube

By studying the geometric effect of the polarization anisotropy we can determine the dielectric constant of this carbon nanotube. In figure 5.2a the energy of the laser is off resonance with any optical transition and hence the density of states in the nanotube is low. For a low density of states the contribution of the carbon nanotube selection rules to the polarization anisotropy is small and the dominating contribution comes from the depolarization effect. The recorded photocurrent signal can be used as a direct measure of the electric field in the device. We consider the laser excitation field, applied to the nanotube. The external electric field, E_e , fully penetrates the carbon nanotube when the polarization is aligned along the nanotube axis, and is probed using the photocurrent, $I_{parallel}$. For cross-polarized light, a smaller fraction of the electric field is coupling in to the nanotube [27]. The amount of the externally applied electric field that is coupling in to the carbon nanotube (the internal field, E_i) is again probed by the photocurrent, $I_{perpendicular}$. The dielectric constant can now be found using the relation:

$$E_i = \frac{2\epsilon_0}{\epsilon_{nanotube} + \epsilon_0} E_e \quad (5.1)$$

where ϵ_0 is the dielectric constant of the environment (in our case vacuum, giving $\epsilon_0 = 1$) and $\epsilon_{nanotube}$ is the dielectric constant of the carbon nanotube. Within this model we consider the carbon nanotube to be a cylinder of infinite length, with a diameter much smaller than the wavelength of the excitation light [27]. Using the detected photocurrent for parallel and perpendicular polarization, a dielectric constant of 3.6 ± 0.2 is found for this semiconducting carbon nanotube. Theory predicts the dielectric constant of a carbon nanotube to assume a value between 1 [28] and 4-5 [29] (without taking excitonic effects into account). Used as a fitting parameter, a dielectric constant of for example 2.5 [17] has been used for a carbon nanotube. Our experimentally measured value for the dielectric constant falls inside the boundaries of the theoretical predictions. The measurement was reproduced on a second semiconducting carbon nanotube device and a resulting dielectric constant of 3.4 was found.

5.5 Polarized photocurrent spectroscopy

Next we perform polarization dependent photocurrent spectroscopy with our laser positioned on the p-n junction using a supercontinuum white light source and a

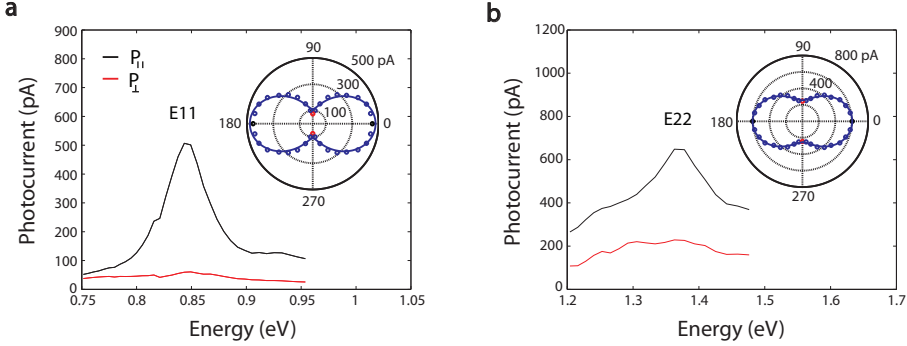


Figure 5.3: Polarized photocurrent spectroscopy on a p-n junction. **(a)** Light polarized parallel to the carbon nanotube axis (black) probes the E11 transition at 0.85 eV, and light polarized perpendicular to the carbon nanotube axis (red) suppresses the E11 optical transition. Inset: angular dependence of the photocurrent (units: pA) on the polarization angle of the excitation light. **(b)** Photocurrent spectroscopy of the E22 optical transition at 1.36 eV. The E22 is probed by parallel polarized light (black) and suppressed for perpendicular polarized light (red). Inset: angular dependence of the photocurrent (units: pA) on the polarization angle for E22.

tunable filter. See methods section for further details. Figure 5.3 displays the photocurrent spectra for light polarized parallel (black) and perpendicular (red) to the carbon nanotube axis. In figure 5.3a a clear peak for the E11 transition is visible at 0.85 eV. In agreement with the theoretical predictions [25, 26] and earlier work [7, 8, 14–16] this transition is probed with parallel polarized light and suppressed for perpendicular polarization. In figure 5.3b the E22 transition at 1.36 eV is, according to the same principle, addressed with parallel polarized light and suppressed with perpendicular polarized light. For these parts of the spectrum the spectral output power of the laser is flat with regards to the nanotube features (see figure 5.4).

The insets in figure 5.3a and b show the angular dependence of the photocurrent for E11 and E22 as a function of the polarization angle of the incident laser light. A polarization ratio of the carbon nanotube can be defined as $\rho = (I_{\parallel} - I_{\perp}) / (I_{\parallel} + I_{\perp})$. The depolarization effect alone gives a polarization ratio of 0.40 ± 0.02 . For the E11 transition a polarization ratio of 0.72 ± 0.08 is found, and for E22 the polarization ratio is 0.53 ± 0.05 . Calculations reported by Islam et al. [7] shows, similarly to our results, a smaller polarizability of E22 compared to E11, as a result of the smaller absorption cross section for the E22 transition. On a resonance the polarizability of the carbon nanotube is a result of both the depolarization effect and the optical selection rules. Knowing the dielectric con-

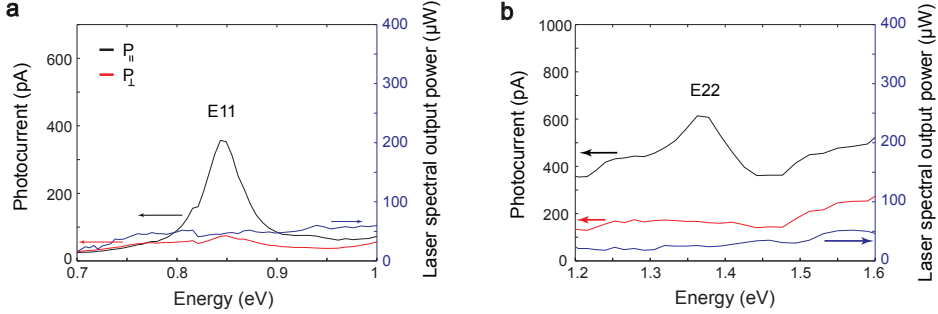


Figure 5.4: Polarization dependent photocurrent spectroscopy of a n-p junction. (a) The E11 optical transition is probed for parallel polarization (black) and suppressed for perpendicular polarization (red). (b) Same for the E22 transition. The blue line is the spectral output power of the laser.

stant these two effects could be decoupled. However, variations in the dielectric constant with frequency [29] makes it difficult to accurately predict the value of the dielectric constant of a carbon nanotube on an optical resonance. Theoretical calculations have been performed on this frequency variation [30–32], however further studies are required on a single nanotube level in the near infra-red part of the spectrum in order to quantify this variation and make an accurate prediction about the decoupling of the two contributions to the polarization anisotropy on an optical resonance.

For light polarized perpendicular to the carbon nanotube axis the E12/E21 transition is expected to show up on the low-energy side of the E22 resonance [15]. However, this transition is considerably suppressed as a result of the depolarization effect and therefore not visible in our measurements.

5.6 Quantitative absorption cross section of a semi-conducting carbon nanotube

A lower limit of the absorption coefficient for an individual suspended semiconducting carbon nanotube can be determined from the external quantum efficiency of the carbon nanotube device:

$$QE_{external} = \frac{\frac{I_{pc}}{e}}{\frac{P_{laser}}{E_{ph}} T_{obj} \frac{A_{nanotube}}{A_{laser}}} \quad (5.2)$$

where I_{pc} is the measured photocurrent (in A), e is the elementary charge, P_{laser} is the power of the incident laser beam (in W), E_{ph} is the energy of the incident photons, T_{obj} is the transmissivity of the objective and $A_{nanotube}/A_{laser}$ is a normalization with respect to the carbon nanotube surface area exposed to the incident laser beam. The external quantum efficiency is a combination of the absorption coefficient of the carbon nanotube and the internal quantum efficiency of the p-n junction. Hence this external quantum efficiency provides a lower limit of the absorption coefficient in this suspended semiconducting carbon nanotube. From equation 5.2 an external quantum efficiency of 0.123 electrons/photons was found for the E11 transition and a lower limit of the absorption coefficient is 12.3 %. Similarly for the E22 transition, the external quantum efficiency is 0.087 and a lower limit for the absorption coefficient is 8.7 %. These results agree well with values reported by Freitag et al. [6] where the authors estimate a quantum efficiency of > 10 % for their single nanotube FET device. For a wavelength off resonance, the extracted lower limit of the absorption coefficient is around 3 %, comparable to that measured for graphene samples [33]. This demonstrates the enhanced absorption for a carbon nanotube when the energy of the excitation laser is on resonance with an optical transition. Figure 5.5 shows the external quantum efficiency, calculated according to equation 5.2, as a function of incident laser power. The efficiency of the device is higher at lower laser powers for both the E11 and the E22 transition. The decreasing efficiency could be attributed to charge accumulation in the device at higher laser powers [34]. Another possible explanation for the decreasing quantum efficiency could be local heating of the nanotube induced by increased laser power. Heating could increase the charge carrier relaxation rate and hence decrease the internal efficiency of the p-n junction and thereby the external quantum efficiency. The absorption in the E22 is generally lower than the absorption in the E11, which is in agreement with previous findings [7].

5.7 Conclusions

In conclusion, polarization dependent photocurrent spectroscopy has been performed on a carbon nanotube p-n junction. The E11 and E22 optical transitions could be readily probed in parallel polarization and is suppressed for perpendicularly polarized light. The polarization anisotropy could be decoupled into the depolarization effect and the optical selection rules and a dielectric constant of 3.6 ± 0.2 could be extracted from the depolarization effect. An external quantum efficiency of 12.3 % and 8.7 % were measured for the E11 and E22 optical resonances, respectively, and this states a lower limit for the absorption coefficient for a single semiconducting carbon nanotube. Experimentally verified values for these physical properties of a carbon nanotube open up possibilities for develop-

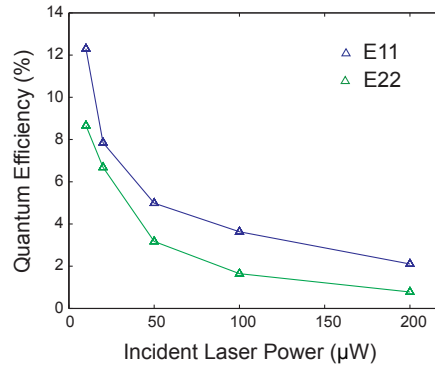


Figure 5.5: Calculated external quantum efficiency as a function of incident laser power. As the laser power is increased, the quantum efficiency decreases for both the E11 and E22 transition. The lines connecting the measurement points serve as a guide to the eye. This quantum efficiency serves as a lower limit for the absorption coefficient in the carbon nanotube device.

ment of future optoelectronic carbon nanotube devices, such as photodetectors and phototransistors, operating in the near infra-red part of the spectrum. A carbon nanotube with a suitable optical resonance could be used for designing photodetectors for telecommunication applications. In addition, this work also demonstrates polarization dependent photocurrent spectroscopy as a tool for probing selected optical transitions in individual carbon nanotubes.

Bibliography

- [1] M. S. Dresselhaus, G. Dresselhaus, R. Saito and A. Jorio. Exciton photophysics of carbon nanotubes. *Annu. Rev. Phys. Chem.* **58**, 719 (2007).
- [2] A. Jorio *et al.* Carbon nanotube photophysics. *Mater. Res. Soc. Bull.* **29**, 276 (2004).
- [3] P. Avouris, M. Freitag and V. Perebeinos. Carbon nanotube photonics and optoelectronics. *Nature Photon.* **2**, 341 (2008).
- [4] J. U. Lee, P. P. Gipp and C. M. Heller. Carbon nanotube p-n junction diodes. *Appl. Phys. Lett.* **85**, 145 (2004).
- [5] T. Mueller *et al.* Efficient narrow-band light emission from a single carbon nanotube p-n diode. *Nature Nanotechn.* **5**, 27 (2010).
- [6] M. Freitag, Y. Martin, J. A. Misewich, R. Martel and P. H. Avouris. Photoconductivity of single carbon nanotubes. *Nano Lett.* **3**, 1067 (2003).
- [7] M. F. Islam, D. E. Milkie, C. L. Kane, A. G. Yodh and J. M. Kikkawa. Direct measurement of the polarized optical absorption cross section of single-wall carbon nanotubes. *Phys. Rev. Lett.* **93**, 037404 (2004).
- [8] Y. Murakami, E. Einarsson, T. Edamura and S. Maruyama. Polarization dependence of the optical absorption of single-walled carbon nanotubes. *Phys. Rev. Lett.* **94**, 087402 (2005).
- [9] M. Ichida, S. Mizuno, Y. Tani, Y. Saito and A. Nakamura. Exciton effects of optical transitions in single-walled carbon nanotubes. *J. Phys. Soc. Jpn.* **68**, 3131 (1999).
- [10] S. H. Jeong *et al.* Optical absorption spectroscopy for determining carbon nanotube concentration in solution. *Synth. Met.* **157**, 570 (2007).
- [11] Z. M. Li *et al.* Polarized absorption spectra of single-walled 4 Å carbon nanotubes aligned in channels of an alpo(4)-5 single crystal. *Phys. Rev. Lett.* **87**, 127401 (2001).
- [12] J. U. Lee, P. J. Codella and M. Pietrykowski. Direct probe of excitonic and continuum transitions in the photocurrent spectroscopy of individual carbon nanotube p-n diodes. *Appl. Phys. Lett.* **90**, 053103 (2007).
- [13] A. Malapanis, D. A. Jones, E. Comfort and J. U. Lee. Measuring carbon nanotube band gaps through leakage current and excitonic transitions of nanotube diodes. *Nano Lett.* **11**, 1946 (2011).

- [14] F. Leonard. *The Physics of Carbon Nanotube Devices*. William Andrew Inc., Norwich (2009).
- [15] J. Lefebvre and P. Finnie. Polarized photoluminescence excitation spectroscopy of single-walled carbon nanotubes. *Phys. Rev. Lett.* **98**, 167406 (2007).
- [16] Y. Miyauchi, M. Oba and S. Maruyama. Cross-polarized optical absorption of single-walled nanotubes by polarized photoluminescence excitation spectroscopy. *Phys. Rev. B* **74**, 205440 (2006).
- [17] F. Wang, G. Dukovic, L. E. Brus and T. F. Heinz. The optical resonances of carbon nanotubes arise from excitons. *Science* **308**, 838 (2005).
- [18] J. Kong, H. T. Soh, A. M. Cassell, C. F. Quate and H. Dai. Synthesis of individual single-walled carbon nanotubes on patterned silicon wafers. *Nature* **395**, 878 (1998).
- [19] G. A. Steele, G. Gotz and L. P. Kouwenhoven. Tunable few-electron double quantum dots and klein tunneling in ultraclean carbon nanotubes. *Nature Nanotech.* **4**, 363 (2009).
- [20] K. Bosnick, N. M. Gabor and P. L. McEuen. Transport in carbon nanotube p-i-n diodes. *Appl. Phys. Lett.* **89**, 163121 (2006).
- [21] K. Balasubramanian, M. Burghard, K. Kern, M. Scolari and A. Mews. Photocurrent imaging of charge transport barriers in carbon nanotube devices. *Nano Lett.* **5**, 507 (2005).
- [22] Y. H. Ahn, A. W. Tsen, B. Kim, Y. W. Park and J. Park. Photocurrent imaging of p-n junctions in ambipolar carbon nanotube transistors. *Nano Lett.* **7**, 3320 (2007).
- [23] G. Buchs, M. Barkelid, S. Bagiante, G. A. Steele and V. Zwiller. Imaging the formation of a p-n junction in a suspended carbon nanotube with scanning photocurrent microscopy. *J. Appl. Phys.* **110**, 074308 (2011).
- [24] M. Freitag *et al.* Imaging the schottky barriers and charge depletion in carbon nanotube transistors. *Nano Lett.* **7**, 2037 (2007).
- [25] H. Ajiki and T. Ando. Aharonov-bohm effect in carbon nanotubes. *Physics B* **201**, 349 (1994).
- [26] T. Ando. Excitons in carbon nanotubes. *Jpn. J. Appl. Phys.* **66**, 1066 (1997).

- [27] J. Wang, M. S. Gudiksen, X. Duan, Y. Cui and C. M. Lieber. Highly polarized photoluminescence and photodetection from single indium phosphide nanowires. *Science* **293**, 1455 (2001).
- [28] F. Leonard and J. Tersoff. Dielectric response of semiconducting carbon nanotubes. *Appl. Phys. Lett.* **81**, 4835 (2002).
- [29] S. Uryu and T. Ando. Exciton absorption of perpendicular polarized light in carbon nanotubes. *Phys. Rev. B* **74**, 155411 (2006).
- [30] F. J. Garcia-Vidal, J. M. Pitarke and J. B. Pendry. Effective medium theory of the optical properties of aligned carbon nanotubes. *Phys. Rev. Lett.* **78**, 4289 (1997).
- [31] T. Pichler, M. Knupfer, M. S. Golden and J. Fink. Localized and delocalized electronic states in single-walled carbon nanotubes. *Phys. Rev. Lett.* **80**, 4729 (1998).
- [32] X. Wu *et al.* Optical properties of aligned carbon nanotubes. *Phys. Rev. B* **68**, 193401 (2003).
- [33] F. Bonaccorso, Z. Sun, T. Hasan and A. C. Ferrari. Graphene photonics and optoelectronics. *Nature Photon.* **4**, 611 (2010).
- [34] C. Kittel. *Introduction to Solid State Physics*. John Wiley Sons, New York (1966).

Chapter 6

Single Carbon Nanotube Photovoltaic Device

Maria Barkelid, Val Zwiller

Here we present photocurrent measurements on a single suspended carbon nanotube p-n junction. The p-n junction was induced by electrostatic doping by local gates, and the E11 and E22 resonances in the nanotube could be probed using photocurrent spectroscopy. Current-voltage characteristics were recorded, revealing an enhanced optoelectronic response on resonance. The internal power conversion efficiency for the nanotube diode was extracted on and off resonance with the E11 and E22, and a large internal power conversion efficiency was observed. An internal efficiency of up to 23% is reported for the E11, showing the potential of carbon nanotubes to be used as the active element in photovoltaic devices. Finally, a photovoltaic device is proposed which exploits this enhanced efficiency.¹

¹This chapter has been published in *Journal of Applied Physics* **114**, 164320 (2013).

6.1 Introduction

Carbon nanotubes are one-dimensional materials with remarkable electrical and optical properties [1, 2]. They have shown promise for photodetection [3] and solar cell applications [4, 5]; however, the efficiency of the energy conversion has been very modest. Lately carbon nanotubes have been combined with Si p-n junctions [6] and composites [7] or integrated in organic solar cells [8], in order to achieve high efficiency photovoltaic devices. In these hybrid structures the carbon nanotubes are typically used for efficient collection of the photogenerated current, and not as the active material for photovoltaic. Besides, studies carried out on networks of carbon nanotubes find that the device efficiency suffer from the coexistence of semiconducting and metallic nanotubes in the network [8]. Therefore, it is important to study the intrinsic efficiency of the carbon nanotube itself in order to evaluate its prospect for photovoltaic devices. Studies on carbon nanotube thin-films addressed the question of their potential as the active material in solar cells [4, 9], but this has not been investigated on the single nanotube level. Large efficiencies have been predicted in the photoresponse of carbon nanotubes near the band edge [10], and recently the energy harvesting potential of carbon nanotubes have been shown to be related to their resonances in the optical spectrum [11].

Here we present photovoltaic measurements on a single carbon nanotube diode and compare the internal power conversion efficiency of the device for different excitation energies. We demonstrate an increased internal power conversion efficiency in the nanotube when excited on the E11 and E22 compared to off resonance excitation. We also found an optimal illumination power for the device, for when this is exceeded the diode becomes saturated and the electrons and holes recombine non-radiatively before they have time to escape the p-n junction.

6.2 Characterization

The carbon nanotubes were grown using CVD [12] on a pre-fabricated device structure. The individual semiconducting carbon nanotubes are grown to bridge a 4 μm wide and 800 nm deep trench. On each side the suspended carbon nanotube makes an electrical contact to W/Pt electrodes. Details about the device fabrication has been reported elsewhere [13, 14]. Two local gates at the bottom of the trench are used for electrostatic doping. A schematic representation of the device geometry can be found in the inset in Fig. 6.1a. By applying a voltage to the trench gates, a p-n junction can be created in the carbon nanotube. This allows for a dynamic device with tunable doping levels.

Electrical and optical measurements were performed on the carbon nanotube

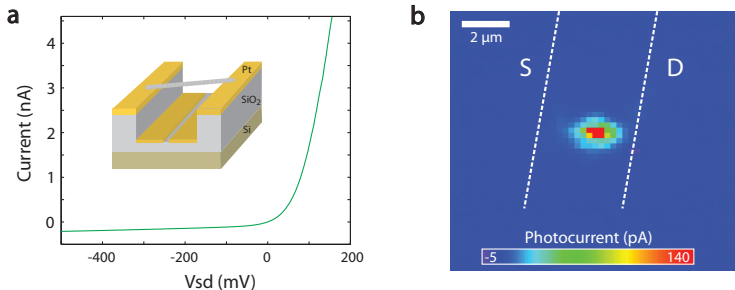


Figure 6.1: Single carbon nanotube diode. (a) An I-V characteristic of the device without illumination, showing a rectifying behavior, characteristic for a diode. A schematic of the device geometry is shown in the inset. $-8/+8$ V was applied to the trench gates to create the p-n junction. (b) Scanning photocurrent microscopy image of the single carbon nanotube p-n junction. The excitation laser (532 nm) was raster scanned over the device, generating a spatial image of the location of the optical response. The scale bar is 2 μm .

diode at room temperature and under vacuum in a home-built scanning confocal microscopy setup. The diode was excited with a supercontinuum white light source (Fianium) in combination with an acousto-optical tunable filter (AOTF). Fig. 6.1a shows the dark current- voltage characteristic of the carbon nanotube device. With $-8/+8$ V applied to the two trench gates the carbon nanotube shows a rectifying behavior, characteristic of a diode.

The p-n junction was spatially located using scanning photocurrent microscopy [13, 15, 16], where the excitation laser is raster scanned over the device and the photocurrent measured at every laser location. This generates the photocurrent image in Fig. 6.1b which shows the optical response from the carbon nanotube p-n junction to be located in the center of the trench.

6.2.1 Single Carbon Nanotube Photovoltaics

After locating the position of the nanotube diode, we performed photocurrent spectroscopy [3, 14, 17] to identify the optical transitions in the carbon nanotube. Fig. 6.2a shows the E11 transition at 0.84 eV. The photocurrent spectrum was measured with the polarization aligned along the nanotube axis [14, 18]. A plot of the photocurrent at E11 as a function of the polarization angle of the excitation laser can be found in the inset in Fig. 6.2a, showing the polarization dependence of the photocurrent signal.

Thereafter we investigated the diode's response to illumination. The I-V characteristic of the carbon nanotube was measured for on resonance excitation

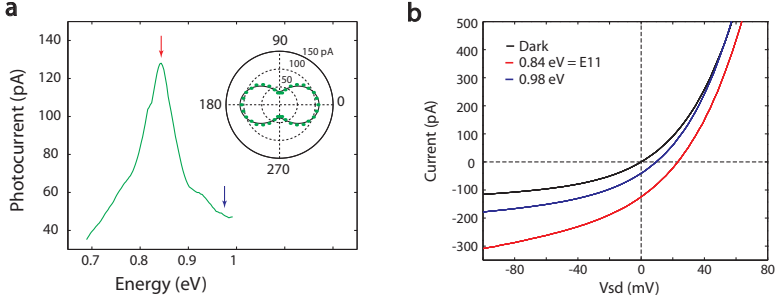


Figure 6.2: Photoresponse in a single carbon nanotube diode. **(a)** Photocurrent spectroscopy on the carbon nanotube p-n junction, showing the E11 optical resonance at 0.84 eV with the polarization aligned along the nanotube axis. The inset shows the polarization dependence of the photocurrent at the E11 transition. **(b)** I-V characteristics recorded without illumination (black), with 0.84 eV excitation (red arrow in **(a)**) and 0.98 eV excitation (blue arrow in **(a)**). The incident laser power was $64 \mu\text{W}$. We clearly see the increased photoinduced current in the device at the E11 energy (red) compared to off resonance (blue).

on the E11 (0.84 eV), as well as for off resonance excitation at 0.98 eV, indicated by arrows in Fig. 6.2a. The incident laser power was kept constant at $64 \mu\text{W}$. Fig. 6.2b shows the I-V characteristics for excitation on E11 (red) compared to the case of no illumination (black), and the photoinduced current in the device under illumination can be observed. We also observe a larger photoinduced current in the device when excited on E11 (red) compared to off resonance excitation (blue).

6.3 Energy Conversion Efficiency

The power conversion efficiency of a diode can be extracted using the open-circuit voltage (V_{oc}), the short-circuit current (I_{sc}), and fill factor (FF) [2, 4]. A V_{oc} of 23 mV and an I_{sc} of 119 pA could be extracted from Fig. 6.2b, for on resonance excitation, and a fill factor of 29% was calculated. The fill factor both on and off resonance showed a very weak dependence on excitation power. This low fill factor and V_{oc} are a result of the poor contact resistance of the device. The W/Pt electrodes make a good p-type contact to the carbon nanotube but work poorly for electron conduction. A device resistance in the order of 100 M Ω was measured, where the series resistance at the contacts is assumed to be dominating. The contact resistance could be improved by for example choosing a different contact metal; however, in our case the choice of metal was restricted by the elevated fabrication temperature.

The power conversion efficiency, η , can now be calculated according to

$$\eta = \frac{I_{sc}}{(P_{in} T_{obj} A)} V_{oc} \cdot FF \quad (6.1)$$

where P_{in} is the incident laser power (measured before the objective), T_{obj} is the transmissivity of the objective, and $A = A_{nanotube}/A_{laser}$, which ensures that we only take into account the photons that are incident on the nanotube surface. We here consider the geometrical cross section of the nanotube, in order to evaluate the absorption efficiency, instead of using the optical absorption cross section per carbon atom [19].

The calculated power conversion efficiency reaches 0.027 for excitation on the E11 and is one order of magnitude lower for off resonance excitation. In order to conclude that the difference in power conversion efficiency for the different excitation energies is not an effect of the increased absorption on the E11 resonance, the data were corrected for the absorption efficiency. The internal power conversion efficiency can be extracted by dividing the power conversion efficiency, η , with the absorption efficiency. A rough estimate of the lower limit of the absorption efficiency in the carbon nanotube can be extracted from the external quantum efficiency, ensuring a conservative estimate of the absorption. The external quantum efficiency has been previously measured for this device geometry [14] and was found for approximately 6 μW excitation power to be 12% on the E11 and approximately 3% for off resonance excitation. These values agree with other reported quantum efficiencies for carbon nanotube devices [3].

6.3.1 Internal Power Conversion Efficiency

Fig. 6.3 shows the resulting internal power conversion efficiency in the nanotube. The power dependence of the internal power conversion efficiency shows a clear increased efficiency on the E11, showing that this increase is not a result of the larger absorption efficiency on the E11, but also related to the separation efficiency of electrons and holes and their conductivity to the electrical contacts. The enhanced energy conversion efficiency on the E11 has been reproduced on one additional device with similar results.

The internal diode efficiency exhibits a peak when excited on the E11. It increases for low optical powers, up to around 6 μW , which can be understood as the photogenerated current having a linear dependence on optical power, for low powers [10]. Thereafter, the efficiency decreases for larger excitation powers. This could be an effect of the increased density of charge carriers in the p-n junction at higher powers. When multiple electrons and holes are present in the junction, they might recombine non-radiatively before having time to escape the

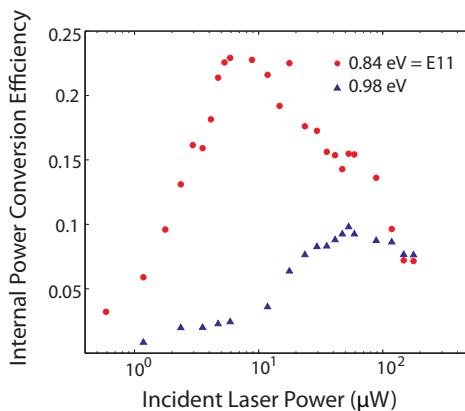


Figure 6.3: Internal power conversion efficiency on and off resonance as a function of excitation power. The internal power conversion efficiency was extracted as a function of excitation power for 0.84 eV (red circles) and 0.98 eV (blue triangles). A clear enhancement in efficiency can be observed on the E11 as well as a peak efficiency around 6 μW . The decrease for large optical power is due to the fact that the junction becomes saturated and not all of the generated electrons and holes have time to escape the junction before recombining.

junction and reaching the contacts [20]. The decreasing efficiency could also be a result of exciton-exciton annihilation [21, 22]. Fig. 6.3 clearly shows a proof of principle that the internal power conversion efficiency of the semiconducting carbon nanotube p-n junction is larger on the E11 than for off resonance excitation while the mechanism for exciton dissociation remains an open question in the field.

The internal power conversion efficiency of the E22 resonance at 1.36 eV was also investigated and found to (after compensating for the absorption efficiency in the nanotube, as described above) give a peak efficiency of 20%. Fig. 6.4 shows the internal power conversion efficiency of E22 and compares it to off resonance excitation. The increased efficiency also observed on the E22 supports our conclusion of enhanced energy conversion efficiency on resonance in our carbon nanotube diode.

6.4 Carbon Nanotube Photovoltaic Device

Considering the vast selection of nanotube chiralities, a solar cell device based on different carbon nanotube species could be designed to operate across the

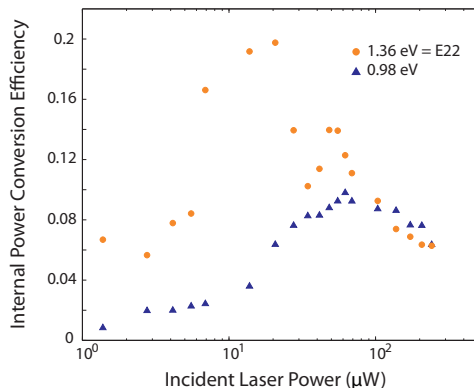


Figure 6.4: Power dependence of the internal power conversion efficiency on the E22 at 1.36 eV (orange circles), compared to off resonance excitation at 0.98 eV (blue triangles). An increased internal power conversion efficiency of the diode can be observed also on the E22.

solar spectrum. For wavelengths of 900 nm and longer a large selection of carbon nanotubes are available with E11 at these wavelengths. The FWHM of the E11 is typically of the order of 50 meV [17, 18], and the density of carbon nanotube chiralities with the E11 above 900 nm is sufficiently high, with respect to the absorption linewidth, to readily cover the infra-red part of the solar spectrum.

For the visible part of the solar spectrum one would need to rely on the E22 or higher resonances, as not enough nanotubes exist with the E11 in the visible range. It is also worth mentioning that although the nanotubes have an enhanced energy conversion efficiency at the resonances their efficiency at higher energies is not zero. The absorption coefficient for light off resonance is approximately 3% [14], and the efficiency of converting this energy into electrical current is 5%-10% (see blue triangles in Figs. 6.3 and 6.4).

Different techniques could be used to tune the E11 to desired energy. For example strain has been demonstrated as a tool to tune the band gap of carbon nanotubes [23], where 1% strain would alter the carbon nanotube band gap ~ 100 meV. Tuning the carbon nanotube band gap could aid in using the more efficient E11 for energy conversion across a larger energy range.

This points to the potential of using carbon nanotubes for photovoltaic. To realize a solar cell of a selection of chirality specific carbon nanotubes, cheaper chirality selection methods are needed. A deeper understanding of the exciton dissociation mechanism in carbon nanotubes would also be necessary in order to design efficient energy harvesting devices. In addition, chirality specific growth

on a predetermined location would truly enable the design of a purely carbon based solar cell, covering the entire solar spectrum.

6.5 Conclusion

In summary, we have demonstrated an enhanced internal power conversion efficiency in a single carbon nanotube diode on resonance with the E11 and E22 optical transitions. Efficiencies of up to 23% were measured in this nanotube diode. This shows the potential of carbon nanotubes for photovoltaic applications and that the optical resonances not only enhance the light absorption in carbon nanotube diodes but also exhibit a larger intrinsic power conversion efficiency. By tailoring a carbon nanotube photovoltaic device such that the E11 coincides with wavelengths of interest, very efficient conversion between light and matter could be realized using carbon nanotubes.

Bibliography

- [1] J.-C. Charlier, X. Blase and S. Roche. Electronic and transport properties of nanotubes. *Rev. Mod. Phys.* **79**, 677 (2007).
- [2] F. Leonard. *The Physics of Carbon Nanotube Devices*. William Andrew Inc., Norwich (2009).
- [3] M. Freitag, Y. Martin, J. A. Misewich, R. Martel and P. H. Avouris. Photoconductivity of single carbon nanotubes. *Nano Lett.* **3**, 1067 (2003).
- [4] J. U. Lee. Photovoltaic effect in ideal carbon nanotube diodes. *Appl. Phys. Lett.* **87**, 073101 (2005).
- [5] D. J. Bindl and M. S. Arnold. Efficient exciton relaxation and charge generation in nearly monochiral (7,5) carbon nanotube/c60 thin-film photovoltaics. *J. Phys. Chem. C* **117**, 2390 (2013).
- [6] Y. Jung, X. Li, N. K. Rajan, A. D. Taylor and M. A. Reed. Record high efficiency single-walled carbon nanotube/silicon p-n junction solar cell. *Nano Lett.* **13**, 95 (2013).
- [7] X. Dang *et al.* Virus-templated self-assembled single-walled carbon nanotubes for highly efficient electron collection in photovoltaic devices. *Nature Nanotechn.* **6**, 377 (2011).
- [8] L. Liu, W. E. Stanchina and G. Li. Effects of semiconducting and metallic single-walled carbon nanotubes on performance of bulk heterojunction organic solar cells. *Appl. Phys. Lett.* **94**, 233309 (2009).
- [9] M. J. Shea and M. S. Arnold. 1films. *Appl. Phys. Lett.* **102**, 243101 (2013).
- [10] D. A. Stewart and F. Leonard. Energy conversion efficiency in nanotube optoelectronics. *Nano Lett.* **5**, 219 (2005).
- [11] D. D. Tune and J. G. Shapter. The potential sunlight harvesting efficiency of carbon nanotube solar cells. *Energy Environ. Sci.* **6**, 2572 (2013).
- [12] J. Kong, H. T. Soh, A. M. Cassell, C. F. Quate and H. Dai. Synthesis of individual single-walled carbon nanotubes on patterned silicon wafers. *Nature* **395**, 878 (1998).
- [13] G. Buchs, M. Barkelid, S. Bagiante, G. A. Steele and V. Zwiller. Imaging the formation of a p-n junction in a suspended carbon nanotube with scanning photocurrent microscopy. *J. Appl. Phys.* **110**, 074308 (2011).

- [14] M. Barkelid, G. A. Steele and V. Zwiller. Probing optical transitions in individual carbon nanotubes using polarized photocurrent spectroscopy. *Nano Lett.* **12**, 5649 (2012).
- [15] Y. H. Ahn, A. W. Tsen, B. Kim, Y. W. Park and J. Park. Photocurrent imaging of p-n junctions in ambipolar carbon nanotube transistors. *Nano Lett.* **7**, 3320 (2007).
- [16] K. Balasubramanian, M. Burghard, K. Kern, M. Scolari and A. Mews. Photocurrent imaging of charge transport barriers in carbon nanotube devices. *Nano Lett.* **5**, 507 (2005).
- [17] J. U. Lee, P. J. Codella and M. Pietrykowski. Direct probe of excitonic and continuum transitions in the photocurrent spectroscopy of individual carbon nanotube p-n diodes. *Appl. Phys. Lett.* **90**, 053103 (2007).
- [18] J. Lefebvre and P. Finnie. Polarized photoluminescence excitation spectroscopy of single-walled carbon nanotubes. *Phys. Rev. Lett.* **98**, 167406 (2007).
- [19] A. Malapanis, V. Perebeinos, D. P. Sinha, E. Comfort and J. U. Lee. Quantum efficiency and capture cross section of first and second excitonic transitions of single-walled carbon nanotubes measured through photoconductivity. *Nano Lett.* **13**, 3531 (2013).
- [20] N. M. Gabor, Z. Zhong, K. Bosnick and P. L. McEuen. Ultrafast photocurrent measurement of the escape time of electrons and holes from carbon nanotube p-i-n photodiodes. *Phys. Rev. Lett.* **108**, 087404 (2012).
- [21] K. Matsuda, T. Inoue, Y. Murakami, S. Maruyama and Y. Kanemitsu. Exciton dephasing and multiexciton recombinations in a single carbon nanotube. *Phys. Rev. B* **77**, 033406 (2008).
- [22] Y. Murakami and J. Kono. Existence of an upper limit on the density of excitons in carbon nanotubes by diffusion-limited exciton-exciton annihilation: Experiment and theory. *Phys. Rev. B* **80**, 035432 (2009).
- [23] E. D. Minot *et al.* Tuning carbon nanotube band gaps with strain. *Phys. Rev. Lett.* **90**, 156401 (2003).

Chapter 7

Photocurrent Generation in Semiconducting and Metallic Carbon Nanotubes

Maria Barkelid, Val Zwiller

The fundamental mechanism underlying photocurrent generation in carbon nanotubes [1–3] has long been an open question. In photocurrent generation, the temperature of the photoexcited charge carriers determines the transport regime by which the electrons and holes are conducted through the nanotube. Here, we identify two different photocurrent mechanisms for metallic and semiconducting carbon nanotube devices with induced p-n junctions [4–7]. Our photocurrent measurements as a function of charge carrier doping demonstrate a thermal origin [8, 9] for metallic nanotubes, where photo-excited hot carriers give rise to a current. For semiconducting nanotubes we demonstrate a photovoltaic mechanism [10–12], where a built-in electric field results in electron-hole separation. Our results provide an understanding of the photoresponse in carbon nanotubes, which is not only of fundamental interest but also of importance for designing carbon-based, high-efficiency photodetectors and energy-harvesting devices. ¹

¹This chapter has been published in *Nature Photonics*, **8**, 47-51 (2014). The authors would like to thank M. S. Rudner for discussions.

7.1 Introduction

To develop sophisticated photonic devices [13–15], the physical processes governing the electro-optical response must be understood. The process of photocurrent generation has been widely studied in both supported [4, 5] and suspended [6, 7] carbon nanotubes, but its origin remains controversial. Two mechanisms compete in carbon nanotubes, the photovoltaic effect [10–12], where photocurrent arises from an electric field, and the photothermal effect [8, 9], where the photocurrent results from a difference in Seebeck coefficients.

Recent studies have established a fingerprint technique for distinguishing between the photothermal and photovoltaic effects in graphene [16–18]. This technique assigns a six-fold-symmetric pattern in the doping-dependent photocurrent response to the photothermoelectric effect and a two-fold symmetry to the photovoltaic effect. Here, we perform doping-dependent photocurrent measurements on individually suspended carbon nanotube devices to investigate the generation of photocurrent.

Figure 7.1a illustrates a nanotube suspended between two metal electrodes, where two local gates were used for remote electrostatic doping [6, 19] (experimental details have been presented elsewhere; chapter 4 and 5). Measurements were performed on three metallic and five semiconducting individual carbon nanotube p-n junctions at room temperature under vacuum.

7.2 Photocurrent response from a metallic and a semiconducting carbon nanotube

Scanning photocurrent microscopy (SPCM) [4, 10, 11] images of semiconducting and metallic nanotube p-n junctions (gate voltage, ± 8 V), with zero source-drain bias, were obtained with a 532 nm (1.45 kWcm^{-2}) laser. The photocurrent and reflection images were superimposed, generating Fig. 7.1b and c. The semiconducting nanotube in Fig. 7.1b shows photocurrent generated at the p-n junction formed between the two gates. The photocurrent from the metallic nanotube p-n junction in Fig. 7.1c has a much broader distribution, possibly a result of inefficient coupling to phonons [20], resulting in a thermal gradient extending along the nanotube due to the long electron cooling length [21]. The transfer characteristics of the two nanotubes are shown in Fig. 7.1d,e. With a bias of 10 mV across the semiconducting nanotube, both gate voltages were swept from negative to positive values. The electron conductance is 10 times lower than the hole conductance due to a poor n-type contact. In the metallic nanotube, with a bias of 1 mV, the conductance could be modulated by the gate voltage, but could not be quenched.

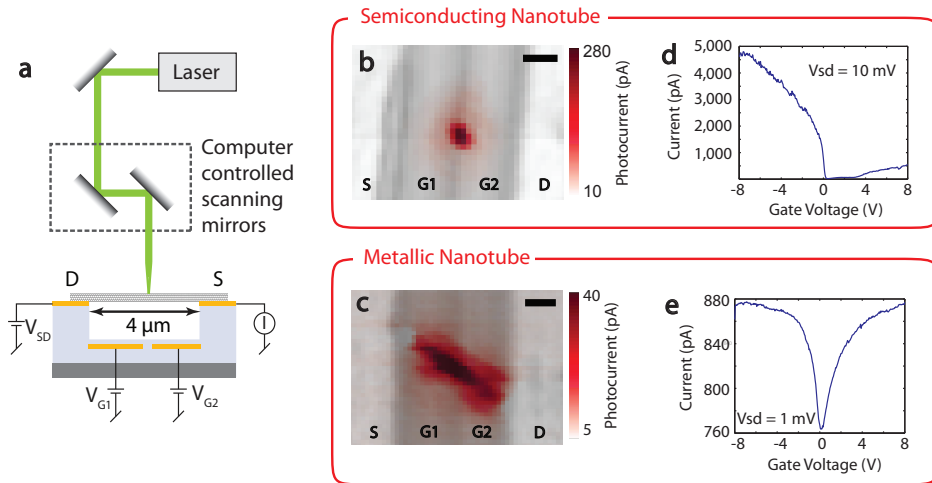


Figure 7.1: SPCM and electrical characterization of semiconducting and metallic carbon nanotube devices. (a), Schematic of the experimental set-up and device geometry, showing the electrical connections to the nanotube. (b), SPCM image (at 532 nm) of the semiconducting nanotube p-n junction. The photocurrent (red) and reflection (grey) images are superimposed and show photocurrent generation from the centre of the trench. (c), SPCM image of the metallic carbon nanotube p-n junction, showing the photoresponse from the whole body of the carbon nanotube. (d), Electrical transfer characteristic of the semiconducting nanotube, showing a clear pinch-off of the conductance. Data were recorded with 10 mV source-drain bias. (e), Transfer characteristic of the metallic nanotube recorded at 1 mV bias. The conductance cannot be completely quenched using gate voltage. Scale bars, 1 μm.

7.2.1 Identification of individual carbon nanotubes

The identification of carbon nanotubes for our study took place in several steps. First the transfer characteristic and the IV characteristic of the devices were measured. From the electrical measurements we can conclude if the device has a semiconducting or a metallic behavior, but not the number of nanotubes that were measured.

For this second step we employ the, by now standard, technique of scanning photocurrent microscopy (SPCM). We raster scan our laser across the complete device and can clearly image the device structure from the back-reflected light. From the photocurrent signal we obtain a spatial image of the locations where photocurrent is generated. (For a device with homogeneous doping this would occur at the Schottky barriers.) Hence the SPCM provides us information about where the nanotube contacts the electrodes and thereby its orientation across the

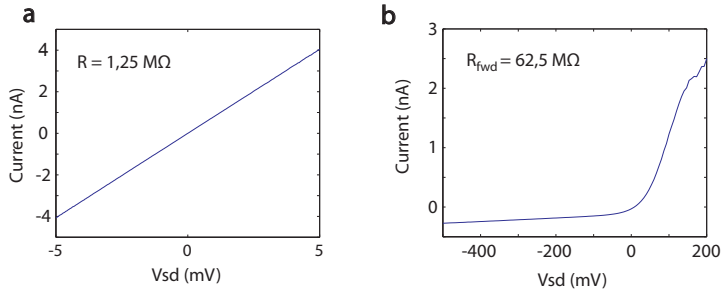


Figure 7.2: Current-Voltage characteristics at room temperature of (a), a metallic nanotube and (b), a semiconducting nanotube at room temperature. Both nanotubes were measured in a p-n doping configuration. The semiconducting nanotube shows clear rectification while the metallic nanotube exhibits a linear IV characteristics.

trench. Any nanotube which does not completely bridge the trench would not make an electrical contact and would therefore not show up in the SPCM. These nanotubes will also not influence our measurements.

Thus with the combination of electrical and optical techniques we can through multiple steps select the nanotubes of interest for our study.

7.2.2 Metallic vs. Semiconducting Carbon Nanotubes

The current-voltage characteristic of a metallic and a semiconducting carbon nanotube was measured at room temperature, under vacuum and in darkness. Figure 7.2a shows the IV for the metallic nanotube, in a p-n doping configuration (+8/-8 V applied to the trench gates). The IV has a linear characteristic and does not show any diode-like behavior. The resistance of the metallic nanotube was calculated to $1,25 \text{ M}\Omega$. The linear behavior indicates that at room temperature the nanotube in 7.2a behaves as a metal. The IV for the semiconducting nanotube in figure 7.2b shows clear rectification, typical for a p-n diode. The measurements were performed under the same conditions (+8/-8 V applied to the gates). The resistance of the semiconducting nanotube was calculated in the forward direction to be $62,5 \text{ M}\Omega$.

In order to investigate the metallic carbon nanotube more in-depth, temperature dependent measurements were performed. Figure 7.3a shows the IV measurement for the nanotube at a temperature of 50 K (and for comparison at 295 K). The applied gate voltage is +/- 8 V and the nanotube still exhibits a linear IV characteristic and a typical metallic behavior. Gate traces for the metallic carbon nanotube were recorded from room temperature down to 50 K and are displayed in figure 7.3b. The curves have been offset for clarity. When sweeping

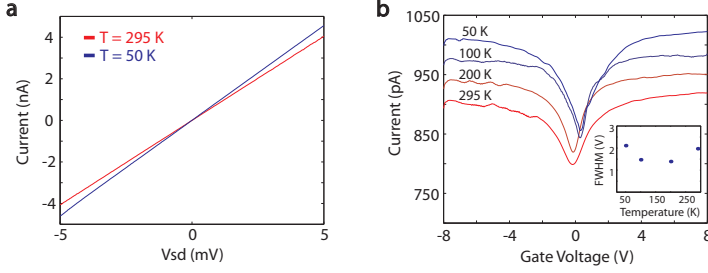


Figure 7.3: Temperature dependence of the metallic nanotube. (a), I-V characteristic of the metallic nanotube measured in a p-n doping configuration at 50 K (blue). An I-V curve at 295 K (red) is shown for comparison. (b), Gate traces of the metallic carbon nanotube recorded between room temperature and 50 K. The dip in conductivity shows a negligible change with temperature and the FWHM is displayed as a function of temperature in the inset. The curves have been offset for clarity.

the gate voltage the doping of the carbon nanotube changes homogeneously from p-type to n-type and the device will display a dip in the conductivity [1]. When the temperatures start to become comparable to the band gap this should show up as a change in the width of the conductivity dip. The FWHM of the conductivity dip is displayed as a function of temperature in the inset. The variation as a function of temperature is negligible, and we conclude that the nanotube behaves as a metal down to 50 K. From these results we can estimate an upper limit for the band gap of this carbon nanotube of approximately 4 meV. For the purpose of this work it can be concluded that the 'nominally' metallic carbon nanotube behaves like a metal for the measurement conditions used in this paper.

7.2.3 Scanning photocurrent microscopy of a metallic carbon nanotube

Individual metallic carbon nanotubes have previously been investigated using SPCM [10], however the focus has been on the contact interface between the nanotube and the metal electrode. Previous work on graphene demonstrated the ability to create a p-n junction in a zero band gap material [22] using electrostatic doping. In this work we have employed a similar technique of electrostatic doping using metal gates. By applying a positive or negative voltage on the gates, the metallic carbon nanotube could be tuned between different doping configurations.

In order to demonstrate the distinct difference between a homogeneously doped metallic nanotube and a p-n junction, SPCM on the metallic nanotube was performed for four different doping configurations, see figure 7.4. We can see that

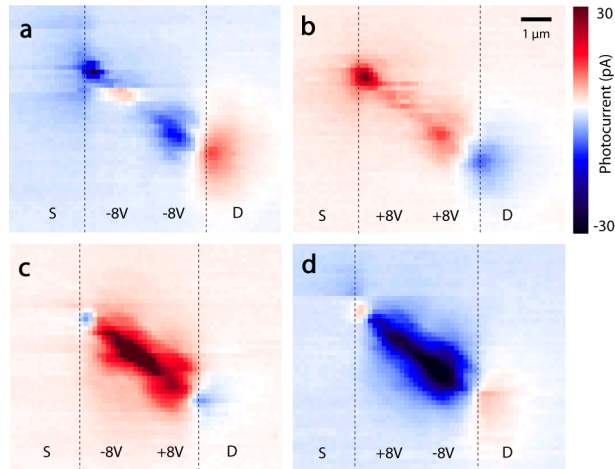


Figure 7.4: SPCM imaging of a metallic carbon nanotube for different doping configurations. Images are recorded at 532 nm. (a), Homogeneous p-type doping of the nanotube. The nanotube/electrode interface shows photocurrent together with two lobes of alternating sign along the nanotube axis. (b), Homogeneous n-type doping. For opposite doping the photocurrent at the nanotube/electrode interface changes sign together with the lobes along the nanotube axis. (c), For a p-n doping configuration the whole body of the nanotube is sensitive to light and dominates the photocurrent response. A relatively small photocurrent contribution can be seen from the nanotube/electrode interface. (d), Same for a n-p doping configuration. The scale bar in b of 1 μm is applicable to all panels.

for a homogeneously doped nanotube the photocurrent at the electrode/nanotube interface changes polarity (Fig. 7.4a and 7.4b), similar to a semiconducting carbon nanotube. A sign change in the photocurrent is observed along the axis of the nanotube, which is in agreement with previous findings [10, 23, 24].

In a p-n or n-p doping configuration the whole length of the suspended carbon nanotube generates photocurrent upon light absorption (Fig. 7.4c and 7.4d), in contrast to a semiconducting nanotube which shows a spatially well-defined photocurrent response from the p-n junction (Fig. 7.1b).

For the metallic nanotube a sign change of the photocurrent can be observed close to the contacts for p-n/n-p doping. The photothermal current, measured in figure 7.4, depends on both the difference in Seebeck coefficient at the interface between two regions and the temperature profile along the nanotube; $I_{Pt} = (S_2 - S_1)T$.

When positioning the laser at the contact/nanotube interface the metal contact will act as a heat sink and the effective temperature induced in the nanotube

will be smaller compared to when positioning the laser at the p-n junction.

The absolute Seebeck coefficient of Pt (S_{Pt}) at room temperature is $-5 \mu\text{V}/\text{K}$ [25]. The Seebeck coefficient of a metallic carbon nanotube can be tuned with gate voltage from approximately $+20 \mu\text{V}/\text{K}$ to $-20 \mu\text{V}/\text{K}$ at room temperature [26].

Close to the contacts the electric field from the gates is screened by the source and drain metal electrodes. Therefore the p- and n-doping of the nanotube close to the contacts will be very weak. A light doping implies a large value of the Seebeck coefficient. It is therefore possible, considering the relation for photothermal current, that the measured photocurrent will have opposite sign at the nanotube/electrode interface compared to the p-n junction.

7.3 Photocurrent maps of a semiconducting and a metallic carbon nanotube

After spatial imaging, the laser was positioned on the p-n junction and the photoresponse was recorded as a function of gate voltage ($\lambda = 532 \text{ nm}$, $P = 1.45 (2.9) \text{ kWcm}^{-2}$ for the semiconducting (metallic) nanotube). The metallic nanotube in Fig. 2a shows a clear six-fold pattern, characteristic of the photothermal effect. As predicted and demonstrated for graphene [16,17], this characteristic pattern arises from the dependence of the photocurrent on the Seebeck coefficient, S . In agreement with ref. [16], due to the close dependence on chemical potential the Seebeck coefficient has a non-monotonic dependence on gate voltage [16,26]. This results in several polarity reversals of ($S_{region2} - S_{region1}$). The photothermal current in the metallic nanotube arises from this difference in Seebeck coefficient in the two regions of the nanotube and hence displays multiple sign changes, giving rise to the six distinct regions in Fig. 7.5a. A line profile is presented in Fig. 7.5b, which demonstrates the multiple sign changes in the photocurrent. The thermally excited hot carriers decay through carrier multiplication into several low-energy electrons, leading to a local hot carrier distribution [27,28].

A photocurrent map was also recorded for the semiconducting nanotube (Fig. 7.5c), which displays a characteristic two-fold pattern indicative of the photovoltaic effect, where the direction of the photocurrent is parallel to the built-in electric field at the junction. An intense photocurrent signal is generated for p-n and n-p doping due to the presence of the electric field dissociating the excitons. For a homogeneously p-doped or n-doped nanotube the photocurrent is negligible, as the electric field is not sufficient to separate the exciton into free charge carriers. In the photovoltaic effect, when tuning the gate voltage, and thereby the charge carrier concentration, the sign of the electric field at the junction changes. For increasing gate voltage, the electric field only changes sign once, resulting in a single polarity change of the photocurrent. Figure 7.5d presents a

line profile of the photocurrent as a function of gate voltage. The sign changes in the photocurrent map in Fig. 7.5c do not occur exactly at zero gate voltage, as a result of the two trench gates not coupling equally to the nanotube or the semiconducting nanotube being slightly p-doped.

Our key observation from Fig. 7.5 is the existence of two distinctly different patterns in the photocurrent response in semiconducting and metallic nanotubes. This shows that the dominant mechanism for the generation of photocurrent differs in the two nanotubes. External factors could potentially suppress the contribution from one or both mechanisms [29, 30]. Accordingly, we defined a set of experimental conditions that justify a comparison between the metallic and semiconducting nanotubes (see section 7.3.1). All nanotubes were measured under identical conditions.

We compared the conductivity in the nanotubes with and without illumination. The resistance measurements in Fig. 7.5e,f, were obtained from current measurements with a bias of 1 mV and 10 mV, respectively. The resistance map of the metallic nanotube shows two highly resistive ridges. This dip in conductivity, similar to that in Fig. 7.1e, causes a change in the Seebeck coefficient. The photocurrent in Fig. 7.5a arising from the difference in the Seebeck coefficient displays a polarity change for the same gate voltages. One additional polarity change is seen along the diagonal in the photocurrent map, which does not have a counterpart in the resistance map. As the doping level is homogeneous, the Seebeck coefficient is uniform along the nanotube and cannot provide a directionality for the thermally excited carriers, and hence makes no net contribution to the photocurrent. For a homogeneously doped semiconducting nanotube, high conductivity is observed (Fig. 7.5f), but the photocurrent (Fig. 7.5c) is negligible. This is a result of the absence of a local electric field. For p-n and n-p doping the device exhibits a large resistance as well as a large photocurrent response due to the presence of an electric field at the junction.

7.3.1 Experimental conditions

In this study we chose a set of experimental conditions so as to make a fair comparison between semiconducting and metallic carbon nanotubes. The nanotubes were suspended to avoid heatsinking from the substrate, which suppresses the photothermal effect. The platinum contact metal was identical for all devices. To minimize the influence from defects, the nanotubes were grown in the final fabrication step and were not subjected to any post-growth fabrication. This resulted in negligible defects being present. The nanotubes were excited off-resonance. This enabled more comparable measurement conditions, as the resonances in the metallic nanotubes could not be probed. All measurements were performed at room temperature.

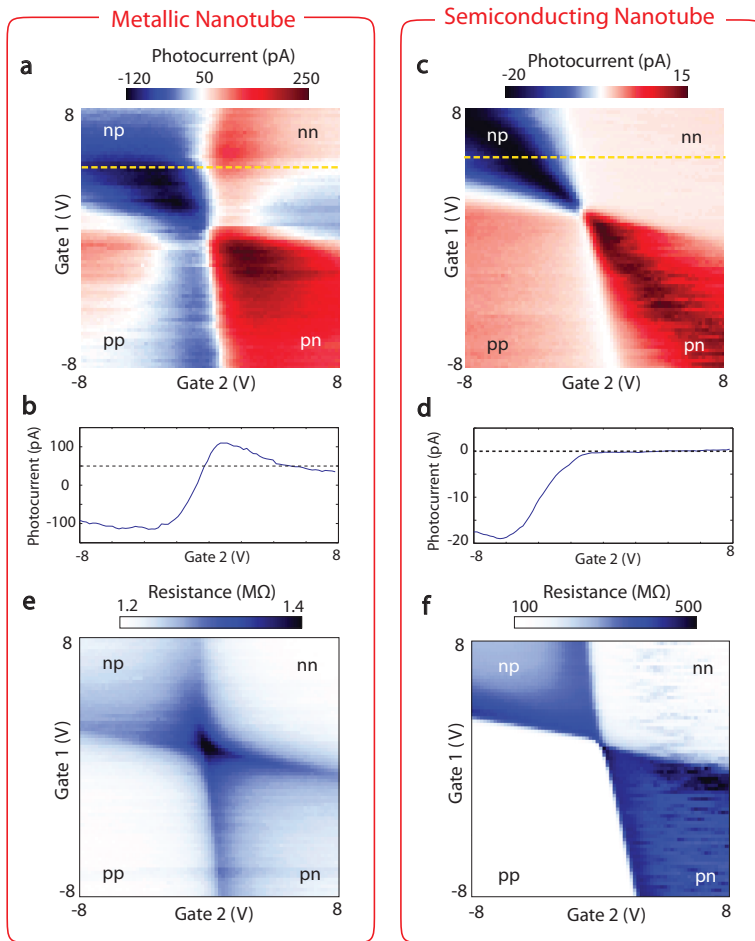


Figure 7.5: Gate-dependent conductivity. (a), Photocurrent map of a metallic nanotube, displaying a six-fold pattern characteristic of the photothermal effect. (b), Line profile of the photocurrent along the yellow line in (a), showing the multiple sign changes of the photocurrent as a function of gate voltage. (c), Photocurrent map of a semiconducting nanotube, displaying a two-fold pattern characteristic of the photovoltaic effect. (d), Line profile of the photocurrent along the yellow line in (c), clearly showing a single sign change of the photocurrent as a function of gate voltage. (e), Resistance as a function of gate voltage for the metallic nanotube. The high-resistance ridges agree with the vertical and horizontal sign changes in the photocurrent map in (a). (f), Resistance map for the semiconducting nanotube. The transition between high- and low-conductance regions corresponds to the transitions in the photocurrent map in (c).

7.4 Photocurrent response from nanotube / electrode interface

To support the existence of different photocurrent generation mechanisms, the photocurrent response along the nanotube axis was investigated as a function of doping. The device was tuned from homogeneous p-type to n-type while scanning the laser along the nanotube axis. The laser path is indicated in Fig. 7.6a for p-type doping of the semiconducting nanotube. Figure 7.6b shows the photocurrent shifting towards the centre of the nanotube with decreasing doping [11]. This arises from a shift in the maximum electric field at the Schottky barriers towards the centre of the nanotube, resulting from the extension of the depletion region with decreasing doping concentration [31]. A line profile of the photocurrent taken along the left green line in Fig. 7.6b is presented in Fig. 7.6c, and shows a continuous increase in photocurrent with increasing gate voltage. This is an effect of the electric field at the Schottky barrier changing sign.

The metallic nanotube (shown with p-type doping in Fig. 7.6d) has a much less pronounced shift in the photocurrent response, as can clearly be seen in Fig. 7.6e. The photocurrent, originating from the difference in Seebeck coefficient of the metallic nanotube and the metal electrode, is generated when the laser is positioned at the nanotube-electrode interface. We tuned the Seebeck coefficient of our metallic nanotube with the gate voltage, causing the photocurrent to change sign. Figure 7.6f presents a line profile (along the left green line in Fig. 7.6e), and shows a non-monotonic dependence on gate voltage, characteristic of the Seebeck effect. The photocurrent responses from the nanotube-electrode interfaces show behavior comparable to that of the photocurrent from the p-n junctions, consistent with our observations of the photothermal and photovoltaic effects dominating in metallic and semiconducting nanotubes, respectively.

7.4.1 Spatial dependence of the photocurrent response

We next studied the photocurrent profile as a function of position along the nanotube axis. The photocurrent from the semiconducting nanotube p-n junction is shown in Fig. 7.7 (blue). The electric field at the junction was probed by the incident laser with a Gaussian profile, which determines the profile of the photocurrent. The data were fitted to a Gaussian, and divided by a factor of four for clarity. The tails come from the laser spot not being perfectly diffraction-limited. The photocurrent from the metallic nanotube p-n junction is shown in red in Fig. 7.7. The photocurrent follows a triangular profile, centered at the p-n junction and extending $\sim 2 \mu\text{m}$ on each side. The broad triangular shape indicates that the photogenerated carriers are hot and follow a thermal distribution through the nanotube. At the electrode-nanotube interface the photocurrent

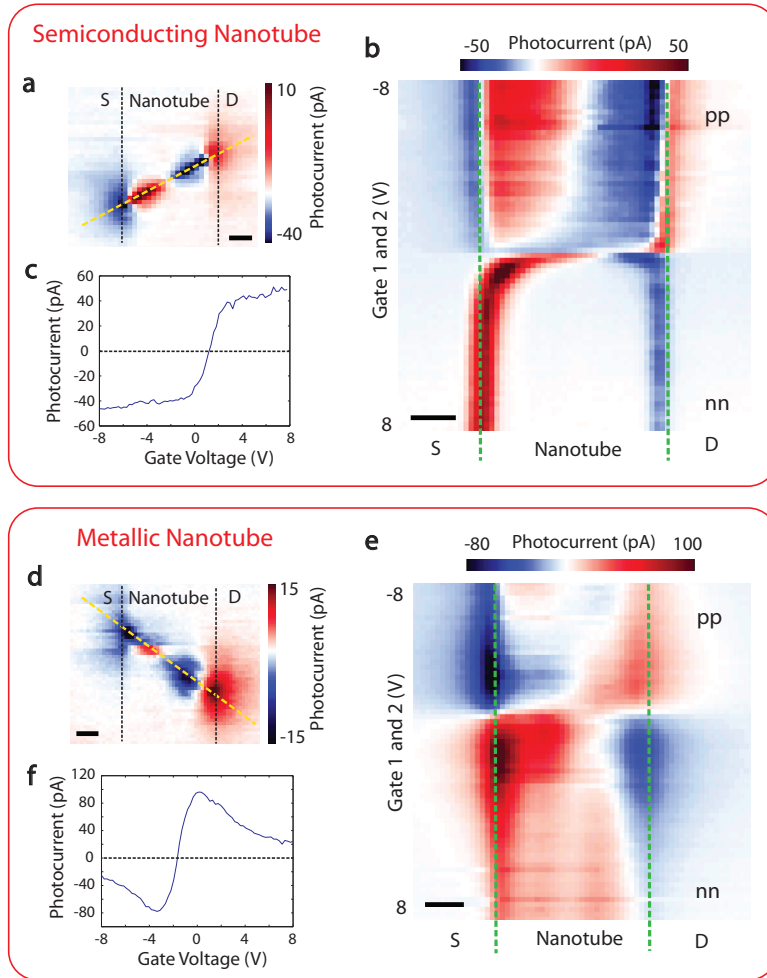


Figure 7.6: Photocurrent response for homogeneous doping. (a), SPCM image of the semiconducting nanotube with homogeneous p-doping. (b), The laser is scanned along the nanotube axis (yellow line in (a)) while changing the doping from p-type to n-type. The photocurrent response shifts towards the centre of the nanotube for low doping levels. (c), Line profile along the left green line in (b). The photocurrent increases with gate voltage, resulting from the sign change of the electric field at the Schottky barrier. (d), SPCM image of the metallic nanotube with p-doping. (e), The laser is scanned along the yellow line in (d), while tuning the gate voltage. The photocurrent from the nanotube-electrode interface shows no spatial shift with gate voltage. (f), Line profile along the left green line in (e). The photocurrent shows a non-monotonic trend originating from the Seebeck effect. Measurements were performed at 532 nm. All scale bars, 1 μm .

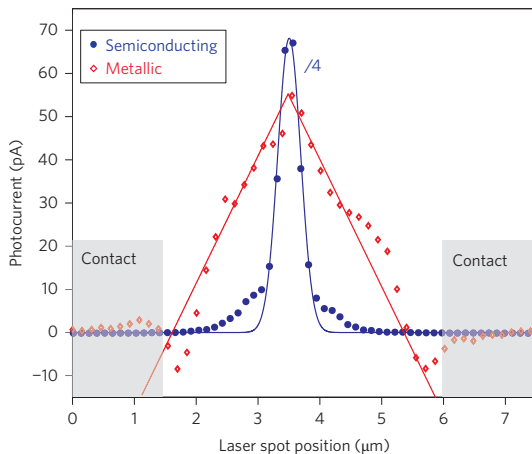


Figure 7.7: Spatial photocurrent response. Photocurrent as a function of position for the semiconducting and metallic carbon nanotube p-n junctions (blue and red, respectively). The photocurrent from the semiconducting nanotube has been fitted with a Gaussian profile, originating from the laser spot profile, which is probed by the electric field at the junction. The photocurrent response from the metallic nanotube follows a triangular profile, indicating that the charge carriers stay hot until they reach the contacts, in agreement with the photothermal effect. Measurements were recorded with a 532 nm laser.

changes sign, possibly a result of band bending at the contacts or a difference in the Seebeck coefficient between the electrode and the nanotube (see section 7.2.3). This difference in photocurrent features confirms that the photocurrent in semiconducting nanotubes results from an electric field and in metallic nanotubes is a thermal effect.

7.4.2 Laser induced temperature

An estimate of the temperature increase in a metallic carbon nanotube induced by the laser has been done using the relation [22]; $\Delta T \sim RI/S$. A resistance, R , of the metallic carbon nanotube of 1,2 M Ω was measured for an n-p doping configuration (Fig. 2e in the main manuscript). For an incident laser power of 100 μ W we estimate an absorption in the carbon nanotube of approximately 4 nW. The measured photocurrent for this absorbed laser power in a n-p doping configuration of the metallic nanotube is measured to be 100 pA (Fig. 7.5a in the main manuscript). A typical value of the Seebeck coefficient is taken to be 20

$\mu\text{V}/\text{K}$ from ref [26]. With this we estimate a laser induced temperature increase of 6 K. This temperature is 15 times larger than what was found for contacted metallic carbon nanotubes on a SiO_2 substrate [9].

7.5 Low temperature measurements

Photocurrent measurements have been performed at low temperature in order to investigate whether the photocurrent generation mechanism for a metallic carbon nanotube would differ at low temperature. This could for example occur if the metallic nanotube has a very small band gap, which could start to play a more important role in the photocurrent generation process at low temperatures.

Figure 7.8 shows the photocurrent maps at $T = 295 \text{ K}$ (7.8a) and at $T = 50 \text{ K}$ (7.8b). The six-fold pattern in the photocurrent maps is clearly visible and comparable both at 295 K and at 50 K. To facilitate the comparison two line profiles are displayed in Fig 7.8c and 7.8d. Both of the line profiles show the non-monotonic behavior of the photocurrent as a function of gate voltage. This behavior is unchanged at low temperatures.

At low temperature we see a drastic increase in the measured photocurrent compared to room temperature. The excitation power at 50 K (1 mW) is 10 times larger than at 295 K. The enhanced excitation power necessary at 50 K could be an indication of the decreasing Seebeck effect at low temperatures. At the same time, the charge carrier life time increases at low temperatures, which would give rise to the increase in photocurrent.

7.6 Pulsed and continuous-wave excitation

The photocurrent response of the carbon nanotubes were investigated for both pulsed and continuous wave (cw) laser excitation. The pulsed laser was a supercontinuum white light source (Fianium), pulsed at 20 MHz together with an acousto-optic tunable filter (AOTF) and the cw laser source was a Ti:sapphire laser. In order to demonstrate that the excitation scheme (pulsed or cw) does not affect the photocurrent generation mechanism, we here show a comparison between pulsed and cw laser excitation. Figure 7.9a shows the photocurrent response from a metallic nanotube under pulsed excitation at 700 nm and 100 μW incident averaged laser power (pulse width of 5 ps). In figure 7.9b the same metallic nanotube was excited with the cw laser (700 nm, 100 μW incident averaged power) under identical measurement conditions. We can clearly resolve the six-fold-symmetric photocurrent pattern for both measurements, confirming that the photothermal mechanism is independent of the type of excitation. This is in

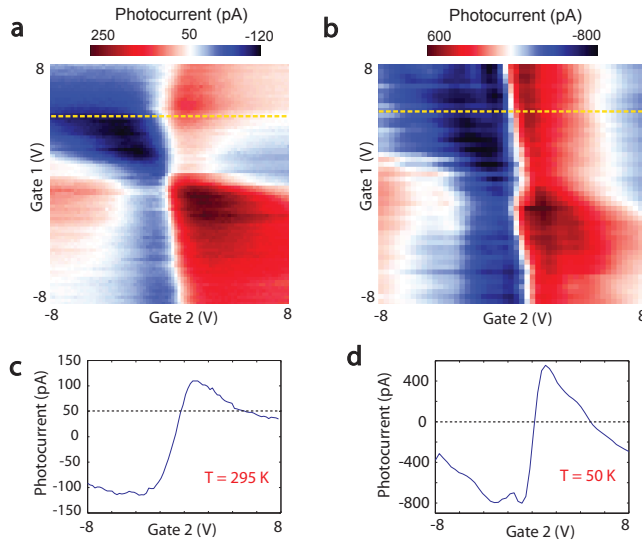


Figure 7.8: Low temperature photocurrent maps of a metallic carbon nanotube. (a), The room temperature photocurrent response ($\lambda = 532$ nm and $100 \mu\text{W}$ of incident laser power). This can be compared to the photocurrent response at 50 K in (b), with $\lambda = 532$ nm and $P = 1$ mW). (c) and (d) shows the line profiles taken along the yellow dashed line in (a) and (b) respectively. The non-monotonic profile of the photocurrent as a function of gate voltage is consistent at 50 K, confirming that the photothermal effect dominates the photocurrent generation in the metallic nanotube also at low temperatures.

contrast to results reported for graphene, where different photocurrent response was recorded for pulsed and cw excitation [32].

Figure 7.9c and 7.9d show the photocurrent response for a semiconducting carbon nanotube under pulsed and cw excitation at 700 nm and $100 \mu\text{W}$ averaged power. Also here it is clear that the photocurrent generation mechanism does not differ between pulsed and cw laser excitation, and the semiconducting nanotube displays clear evidence of the photovoltaic effect.

The semiconducting carbon nanotube shows an increased photocurrent magnitude with cw laser excitation. This could be explained by the fact that our cw laser is fiber coupled and exhibits a nice Gaussian shape. The pulsed laser we use is free space coupled and its beam size is such that about half of the measured power falls outside the aperture of the objective. Due to the AOTF and the free space coupling, the beam shape of the pulsed laser does not exhibit an equally nice Gaussian shape as the fiber coupled beam, hence resulting in a poorer focus

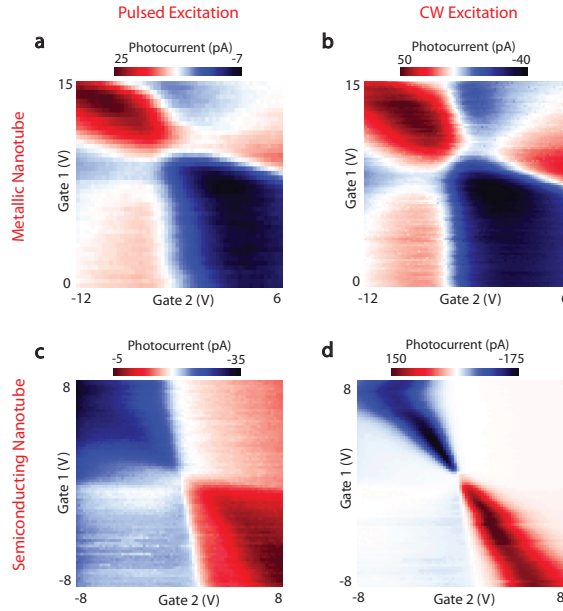


Figure 7.9: Photocurrent maps for pulsed and cw laser excitation. (a), A metallic carbon nanotube excited with a pulsed laser. (b), Same nanotube as in (a) excited with a cw laser. The signature of the photothermal effect is unchanged for the two measurements. (c), A semiconducting carbon nanotube excited with a pulsed laser. (d), Same nanotube as in (c) excited with a cw laser. The signature of the photovoltaic effect is not affected by the difference in excitation. All measurements were performed at 700 nm and 100 μ W averaged incident power.

on the sample. The metallic carbon nanotube also shows a slight increase in the photocurrent for cw excitation, however, not as drastic as the semiconducting nanotube.

The main focus of the study of different excitation schemes is to confirm that the photocurrent generation mechanism do not differ between pulsed and cw laser excitation. As can be seen from figure 7.9 the characteristic patterns in the photocurrent response remain photothermal for the metallic nanotube and photovoltaic for the semiconducting nanotube.

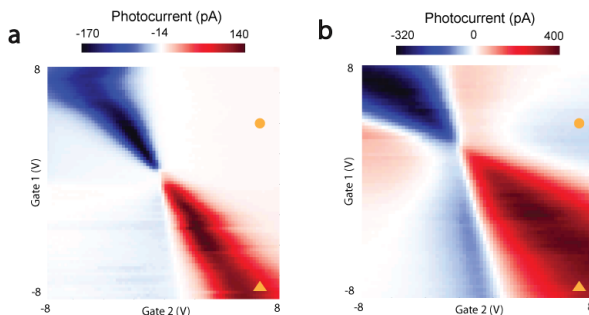


Figure 7.10: Gate-dependent photocurrent response from (a) a semiconducting carbon nanotube and (b) a metallic carbon nanotube. Measurements were performed on a total of five semiconducting and three metallic nanotubes. The devices were excited with a 532 nm laser with 50 μW of power (semiconducting devices) and 100 μW of power (metallic devices).

7.7 Additional devices

Figure 7.10 shows the photocurrent response as a function of gate voltage for a metallic and a semiconducting carbon nanotube investigated in this study. All the metallic nanotubes investigated show a characteristic pattern of six regions of alternating photocurrent sign, while the semiconducting nanotubes show 2 regions of photocurrent response for the p-n and n-p doping, but shows negligible photocurrent for homogeneous doping. This indicates that the photothermal effect is the dominating photocurrent generation mechanism in the metallic nanotubes, while the photovoltaic effect dominates in the semiconducting carbon nanotubes.

Although the qualitative difference between the photocurrent response for metallic and semiconducting nanotubes is clear from figure 7.10, we have tried to quantify this behavior. In order to establish a measurable parameter for comparison we have studied the amplitude of the photocurrent in the p-n doping configuration (marked with an orange triangle in 7.10a and b) as well as the amplitude in the n-n' doping configuration (orange circle in 7.10a and b). The n-n' region is where the distinct difference between the photothermal and photovoltaic effect is most pronounced.

Table 7.11 shows an overview of all the metallic and semiconducting nanotubes measured in this study and the corresponding absolute photocurrent amplitudes in the two different doping configurations. When comparing the photocurrent amplitude in the two regions it is clear that the metallic nanotubes exhibit a substantially larger current in the n-n' region compared to the semiconducting nanotubes. This behavior agrees with our conclusion that the photothermal effect

Device	$\left \text{Amp}_{\text{PC}}^{\text{p-n}} \right $	$\left \text{Amp}_{\text{PC}}^{\text{n-n}'} \right $	$\frac{\left \text{Amp}_{\text{PC}}^{\text{n-n}'} \right }{\left \text{Amp}_{\text{PC}}^{\text{p-n}} \right }$
Metallic A	116 pA	54 pA	0.47
Metallic B	16 pA	5 pA	0.31
Metallic C	361 pA	31 pA	0.09
Semiconducting A	14 pA	0.5 pA	0.04
Semiconducting B	103 pA	1 pA	0.01
Semiconducting C	692 pA	4 pA	0.006
Semiconducting D	1295 pA	2 pA	0.002
Semiconducting E	455 pA	15 pA	0.03

Figure 7.11: Device performance. The amplitude of the photocurrent for all the metallic and semiconducting carbon nanotubes were measured. The amplitude of the photocurrent in the p-n doped region and the n-n' doped region is listed. In the metallic nanotubes the photocurrent in the n-n' region is much more substantial compared to the p-n doping region, than in the semiconducting nanotubes. This behavior agrees with our conclusion of a dominating photothermal mechanism in metallic nanotubes and a dominating photovoltaic mechanism in semiconducting nanotubes.

dominates in the metallic nanotubes and the photovoltaic effect dominates in the semiconducting nanotubes.

7.8 Conclusions

In summary, we have presented clear evidence that different photocurrent generation mechanisms dominate the photocurrent response in metallic and semiconducting nanotubes. Metallic nanotubes exhibit a dominating photothermal effect, whereas the photovoltaic effect dominates the photocurrent response in semiconducting nanotubes. A detailed understanding of the physical processes that govern photocurrent generation in carbon nanotubes is the first important step towards optimizing the design of optoelectronic devices for photodetection and energy harvesting [33, 34]. This will enable highly efficient optical components based on carbon nanotubes to be engineered.

Bibliography

- [1] M. J. Biercuk, S. Ilani, C. M. Marcus and P. L. McEuen. Electrical transport in single-walled carbon nanotubes. *Topics Appl. Phys.* **111**, 455 (2008).
- [2] M. S. Dresselhaus, G. Dresselhaus, J. C. Charlier and E. Hernandez. Electrical, thermal and mechanical properties of carbon nanotubes. *Phil. Trans. R. Soc. Lond. A* **362**, 2065 (2004).
- [3] M. S. Dresselhaus, G. Dresselhaus, R. Saito and A. Jorio. Exciton photo-physics of carbon nanotubes. *Annu. Rev. Phys. Chem.* **58**, 719 (2007).
- [4] M. Freitag, Y. Martin, J. A. Misewich, R. Martel and P. H. Avouris. Photoconductivity of single carbon nanotubes. *Nano Lett.* **3**, 1067 (2003).
- [5] N. M. Gabor, Z. Zhong, K. Bosnick, J. Park and P. L. McEuen. Extremely efficient multiple electron-hole pair generation in carbon nanotube photodiodes. *Science* **325**, 1367 (2009).
- [6] J. U. Lee, P. P. Gipp and C. M. Heller. Carbon nanotube p-n junction diodes. *Appl. Phys. Lett.* **85**, 145 (2004).
- [7] M. Barkelid, G. A. Steele and V. Zwiller. Probing optical transitions in individual carbon nanotubes using polarized photocurrent spectroscopy. *Nano Lett.* **12**, 5649 (2012).
- [8] B. C. St-Antoine, D. Menard and R. Martel. Position sensitive photothermoelectric effect in suspended single-walled carbon nanotube films. *Nano Lett.* **9**, 3503 (2009).
- [9] A. W. Tsen, L. A. K. Donev, H. Kurt, L. H. Herman and J. Park. Imaging the electrical conductance of individual carbon nanotubes with photothermal current imaging. *Nature Nanotechn.* **4**, 108 (2008).
- [10] K. Balasubramanian, M. Burghard, K. Kern, M. Scolari and A. Mews. Photocurrent imaging of charge transport barriers in carbon nanotube devices. *Nano Lett.* **5**, 507 (2005).
- [11] Y. H. Ahn, A. W. Tsen, B. Kim, Y. W. Park and J. Park. Photocurrent imaging of p-n junctions in ambipolar carbon nanotube transistors. *Nano Lett.* **7**, 3320 (2007).
- [12] K. Balasubramanian, Y. Fan, M. Burghard and K. Kern. Photoelectronic transport imaging of individual semiconducting carbon nanotubes. *Appl. Phys. Lett.* **84**, 2400 (2004).

- [13] T. Mueller *et al.* Efficient narrow-band light emission from a single carbon nanotube p-n diode. *Nature Nanotechn.* **5**, 27 (2010).
- [14] P. W. Barone, S. Baik, D. A. Heller and M. S. Strano. Near-infrared optical sensors based on single-walled carbon nanotubes. *Nature Mat.* **4**, 86 (2005).
- [15] J. U. Lee. Photovoltaic effect in ideal carbon nanotube diodes. *Appl. Phys. Lett.* **87**, 073101 (2005).
- [16] J. C. W. Song, M. S. Rudner, C. M. Marcus and L. S. Levitov. Hot carrier transport and photocurrent response in graphene. *Nano Lett.* **11**, 4688 (2011).
- [17] N. M. Gabor *et al.* Hot carrier-assisted intrinsic photoresponse in graphene. *Science* **334**, 648 (2011).
- [18] D. Sun *et al.* Ultrafast hot-carrier-dominated photocurrent in graphene. *Nature Nanotechn.* **7**, 114 (2012).
- [19] G. Buchs, M. Barkelid, S. Bagiante, G. A. Steele and V. Zwiller. Imaging the formation of a p-n junction in a suspended carbon nanotube with scanning photocurrent microscopy. *J. Appl. Phys.* **110**, 074308 (2011).
- [20] E. Pop *et al.* Negative differential conductance and hot phonons in suspended nanotube molecular wires. *Phys. Rev. Lett.* **95**, 155505 (2005).
- [21] J. H. Strait *et al.* Very slow cooling dynamics of photoexcited carriers in graphene observed by optical-pump terahertz-probe spectroscopy. *Nano Lett.* **11**, 4902 (2011).
- [22] M. C. Lemme. Gate-activated photoresponse in a graphene p-n junction. *Nano Lett.* **11**, 4134 (2011).
- [23] J. H. L. Lee. Electronic-band-structure mapping of nanotube transistors by scanning photocurrent microscopy. *Small* **12**, 2038 (2007).
- [24] M. Freitag. Imaging of the schottky barriers and charge carrier depletion in carbon nanotube transistors. *Nano Lett.* **7**, 2037 (2007).
- [25] J. P. Moore and R. S. Graves. Absolute seebeck coefficient of platinum from 80 to 340 k and the thermal and electrical conductivities of lead from 80 to 400 k. *J. Appl. Phys.* **44**, 1174 (1973).
- [26] J. P. Small, K. M. Perez and P. Kim. Modulation of thermoelectric power of individual carbon nanotubes. *Phys. Rev. Lett.* **91**, 256801 (2003).

- [27] V. Perebeinos and P. Avouris. Impact excitation by hot carriers in carbon nanotubes. *Phys. Rev. B* **74**, 121410 (2006).
- [28] K. J. Tielrooij *et al.* Photoexcitation cascade and multiple hot-carrier generation in graphene. *Nature Phys.* **9**, 248 (2013).
- [29] M. Freitag, T. Low, F. Xia and P. Avouris. Photoconductivity of biased graphene. *Nature Photon.* **7**, 53 (2013).
- [30] M. Freitag, T. Low and P. Avouris. Increased responsivity of suspended graphene photodetectors. *Nano Lett.* **13**, 1644 (2013).
- [31] S. M. Sze. *Semiconductor Devices Physics and Technology*. Wiley, USA (2002).
- [32] C.-H. Liu, N. M. Dissanayake, S. Lee, K. Lee and Z. Zhong. Evidence for extraction of photoexcited hot carriers from graphene. *ACS Nano* **6**, 7172 (2012).
- [33] R. T. Ross and A. J. Nozik. Efficiency of hot-carrier solar energy converters. *J. Appl. Phys.* **53**, 3813 (1982).
- [34] M. Omari and N. A. Kouklin. Photothermovoltaic effect in carbon nanotubes: En route toward junctionless infrared photocells and light sensors. *Appl. Phys. Lett.* **98**, 243113 (2011).

Chapter 8

Resonant Photocurrent Response in a Semiconducting Carbon Nanotube

The photocurrent response in a suspended semiconducting carbon nanotube is studied under excitation on the E11 and E22. Numerous studies have investigated the photocurrent generation in nanotubes, however, in these studies the excitation of the nanotube is usually performed at energies several times larger than the band gap. Here we present photocurrent measurement with optical excitation comparable to the band gap of the carbon nanotube and discuss how the photocurrent generation depends on the excitation wavelength and intensity. The photocurrent is also investigated with increased thermal coupling between the nanotube and the environment. ¹

¹This chapter is in preparation.

8.1 Introduction

Photocurrent generation in carbon nanotubes has been extensively studied in varying device geometries [1–3]. For all of these studies the excitation of the nanotubes is performed with energies many times that of the band gap. It is well known that the optical spectra in carbon nanotubes is dominated by excitonic effects [4]. It is therefore instructive to study the photocurrent response of a semiconducting carbon nanotube at energies comparable to the nanotube band gap.

The photocurrent in carbon nanotubes arise as a result of two different mechanisms, the photovoltaic effect or the photothermal effect [5] (see chapter 7). The photovoltaic mechanism has a signature of a two fold symmetry in the gate-dependent photocurrent response and a single sign-change of the photocurrent with gate voltage. Contrary, the photothermal mechanism has a characteristic six-fold photocurrent response with multiple sign-changes in the photocurrent as a function of gate voltage [6, 7]. Off resonance excitation has shown that the dominating mechanism in semiconducting carbon nanotubes is the photovoltaic effect (chapter 7). It can however be instructive to validate this model for low energy excitation.

Previous work on photocurrent in graphene has shown that experimental conditions can alter the relative strengths of the photocurrent generation mechanism [8–10]. For carbon nanotubes the van Hove singularities are known to extensively influence the optoelectronic properties [11]. Thus we will here investigate the contributions from the photovoltaic and photothermal mechanisms in a semiconducting carbon nanotube for excitation on the E11 and E22.

8.2 Device characterization

For this experiment we use a semiconducting carbon nanotube, suspended between two metal electrodes. The carbon nanotube was grown with CVD [12] on a pre-fabricated device structure. Details about the fabrication has been reported elsewhere [5, 13, 14]. A schematic of the device geometry can be found in figure 8.1a. Located at the bottom of the 4 μm wide and 800 nm deep trench were two local gates. A p-n junction was created in the carbon nanotube by means of electrostatic doping. All measurements were performed at room temperature. Optical characterization was performed with a supercontinuum white light source, in combination with an acousto-optical tunable filter.

The semiconducting nature of the carbon nanotube was confirmed from the transfer characteristic of the device. With +/- 8V applied to the trench gates, the p-n junction in the nanotube was imaged using scanning photocurrent microscopy,

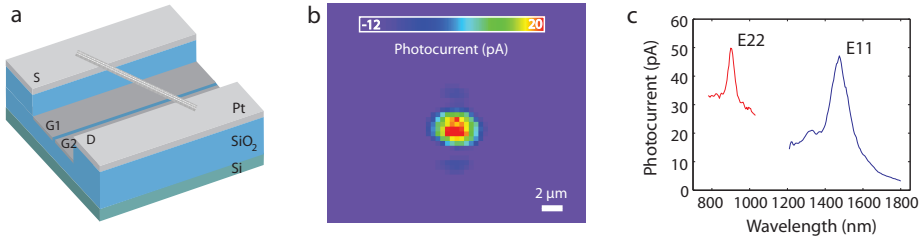


Figure 8.1: Device characteristics. (a) Schematic of the suspended carbon nanotube across the $4\ \mu\text{m}$ wide trench. The electrodes and the gates are made of W/Pt. (b) Scanning photocurrent microscopy image of the p-n junction in the carbon nanotube with $\pm 8\ \text{V}$ applied to the trench gates. The nanotube was excited at $0.84\ \text{eV}$ corresponding to the E11. (c) Photocurrent spectroscopy of the carbon nanotube p-n junction, with the polarization of the excitation laser aligned along the nanotube axis. The E11 and the E22 transitions can be observed at $1475\ \text{nm}$ and $910\ \text{nm}$ respectively.

SPCM, with an excitation energy of $0.84\ \text{eV}$, as shown in figure 8.1b. An energy of $0.84\ \text{eV}$ corresponds to the E11 optical transition in this carbon nanotube, which was confirmed by photocurrent spectroscopy measurements shown in figure 8.1c.

8.3 Photocurrent response from the E11 and E22

The photocurrent signal from the E11 in figure 8.1c is relatively large compared to the E22. It could be instructive to investigate the relative contributions from the photothermal and photovoltaic effects on the E11 and E22 respectively.

Figure 8.2b shows the photocurrent response from the E11, obtained by focusing the laser in the center of the trench (where the p-n junction is created) and fixing the excitation energy to $0.84\ \text{eV}$. The polarization of the excitation laser is aligned parallel to the nanotube axis. The voltage of the trench gates were scanned from negative to positive values and the photocurrent response could be mapped as a function of doping configuration. The photocurrent response from the E11 shows a large photocurrent for the p-n and n-p doping, while n-type and p-type doping show a negligible photocurrent response. This clear two-fold symmetry is indicative of a dominating photovoltaic effect.

For excitation on the E22 we also observe a dominating photovoltaic effect, as can be seen in figure 8.2a. This results agree well with the results from chapter 7 where the dominating photocurrent generation mechanism in semiconducting carbon nanotubes are determined to be the photovoltaic effect.

For excitation wavelengths close to the resonances ($1300, 1200, 1000$ and $800\ \text{nm}$) the dominating photocurrent generation mechanism is also found to be the

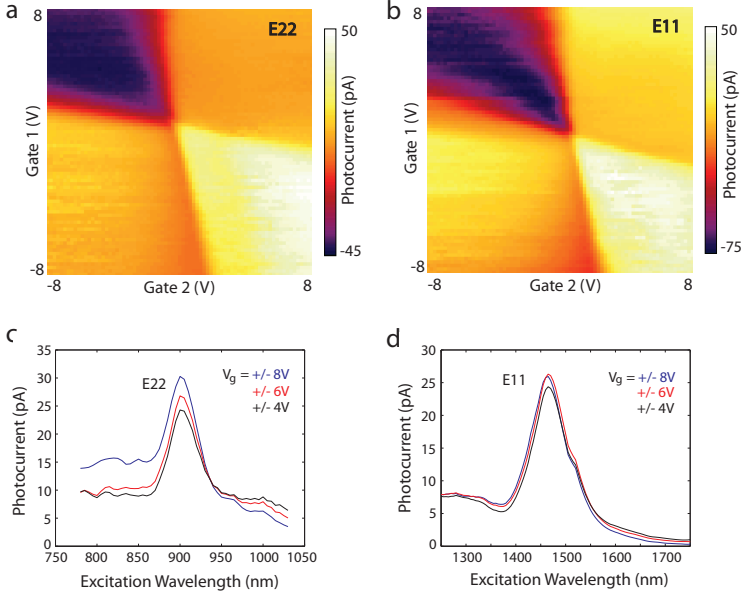


Figure 8.2: Photocurrent as a function of doping concentration. (a) Photocurrent response from the E22. The two-fold symmetry, indicative of the photovoltaic effect, dominates the photocurrent response. (b) Photocurrent response from the E11, also showing a dominating photovoltaic effect. (c)-(d) Shows the photocurrent spectroscopy of the E22 and the E11 for various gate voltages. On the E11 the photocurrent signal is not altered by the change in gate voltage, however a small decrease of the photocurrent can be observed on the E22 for decreasing gate voltage. The excitation power used was $70 \mu\text{W}$.

photovoltaic effect. This concludes that the optical resonances in carbon nanotubes do not influence the underlying mechanism for photocurrent generation in semiconducting carbon nanotubes.

Figure 8.2c-d show the photocurrent spectrum for the E22 and E11, respectively, for different gate voltages. The data shown is the difference in photocurrent between parallel and perpendicular polarization of the excitation light with respect to the nanotube axis ($I_{pc} = I_{pc,\parallel} - I_{pc,\perp}$). For both the E11 and the E22 the spectral position and the linewidth of the photocurrent signal is not noticeably altered by the change in gate voltage. A spectral shift of the resonant photocurrent response with gate voltage could be a signature of many-body interaction in the carbon nanotube, which has recently been suggested for higher subbands probed by Rayleigh scattering [15]. While an increase in the linewidth could be

a signature of intersubband scattering [16].

The fact that the maximum photocurrent for the E11 do not change with increasing gate voltage also suggests that the photocurrent arise from an electric field. Once the electric field is large enough to overcome the exciton binding energy a resulting photocurrent will show up upon laser excitation. Photocurrent generated from the presence of an electric field would not be expected to increase if the magnitude of the electric field increases.

For the E22 the photocurrent in figure 8.2c decreases slightly when the gate voltage is decreased. However, the signature measurement in figure 8.2a conclusively shows a dominating photovoltaic mechanism.

8.3.1 Power Dependence

By studying how the photocurrent changes with applied gate voltage and the excitation power, one could obtain information not only about the dominating photocurrent generation mechanism, but also about the E11 and E22 excitonic processes.

Figure 8.3 shows the photocurrent as a function of excitation power and gate voltage for excitation on the E11 and the E22. In figure 8.3a the photocurrent response from the E11 is observed as a function of laser spot position along the nanotube axis, for a range of gate voltages from +/- 0.5 V to +/- 8V. A larger gate voltage would result in a sharper p-n junction and a larger electric field at the junction. However, we do not observe any sizable increase in the magnitude of the photocurrent, nor does the photocurrent response become spatially narrower.

The maximum photocurrent from figure 8.3a is shown in figure 8.3b as a function of gate voltage. The photocurrent shows no increase with gate voltage for low excitation powers. Once the electric field in the p-n junction is sufficiently large to separate the exciton into free electrons and holes, a photocurrent can be observed and an increase in the electric field will not increase the photocurrent once the exciton has been dissociated. For larger excitation powers a slight increase in the photocurrent can be observed.

In figure 8.3c the photocurrent as a function of excitation power from the E11 shows a sublinear dependence on excitation power. This could be interpreted as the photocurrent resulting from dissociation of the E11 exciton [17]. The photocurrent in figure 8.3c is proportional to the exciton density in the carbon nanotube, where the slight saturation of the curve for larger excitation powers could be an effect of exciton-exciton annihilation [18,19].

Similar investigation was performed on E22, see figure 8.3d-e. The dependence of gate voltage of the photocurrent from the E22 was even smaller than from the E11 as shown by the negligible photocurrent increase in figure 8.3d. For very low powers the photocurrent even decreases slightly with increasing gate

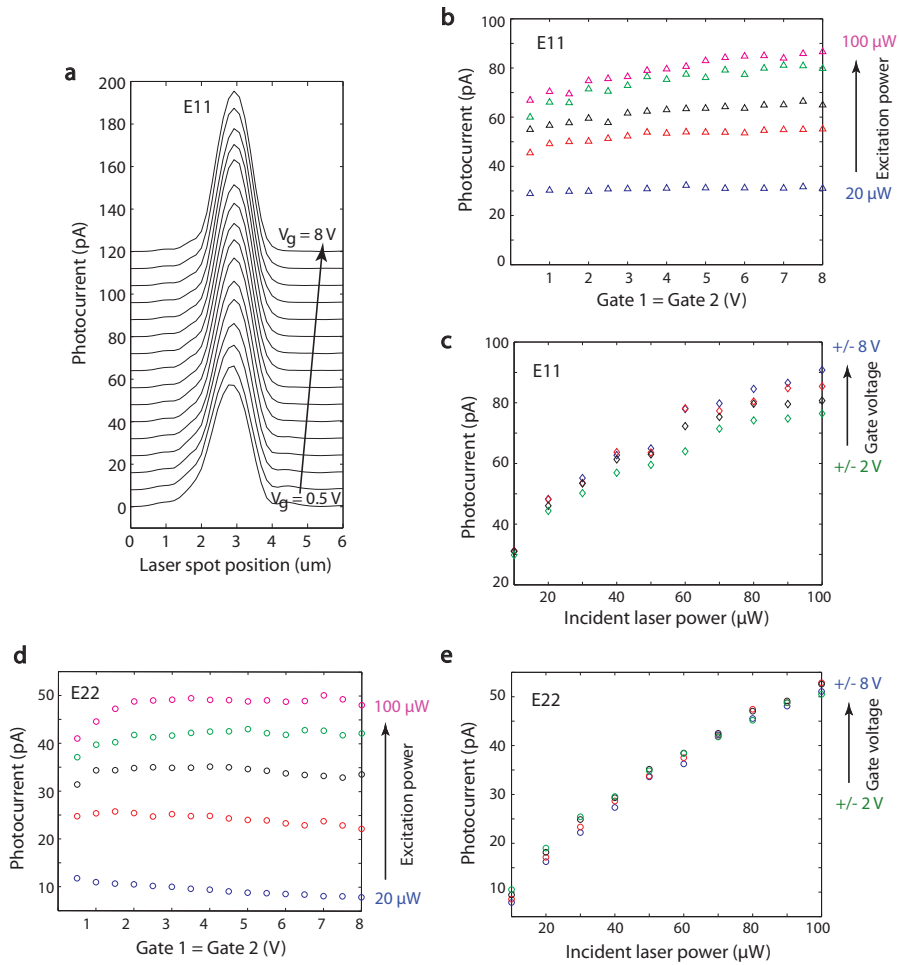


Figure 8.3: Power dependence and gate voltage dependence of the photocurrent. (a) Line profiles of the photocurrent on the E11. The gate voltage (positive and negative respectively on gate 1 and gate 2) was varied from ± 0.5 V to ± 8 V and the excitation power used was $60 \mu\text{W}$. The curves have been offset for clarity. (b) Gate voltage dependence and (c) power dependence of the maximum photocurrent at E11. (d)-(e) Shows the same measurement for E22.

voltage. For larger excitation powers the variation of the photocurrent with gate voltage is nearly negligible, apart from a small increase below 1 or 2 volts. When exciting the carbon nanotube on the E22 there are two possible scenarios. Either the E22 exciton can be directly dissociated into free electrons and holes, or it decays into an E11 exciton which is then dissociated. The power dependence in figure 8.3e shows a clear increase in the photocurrent with excitation power and a slightly sublinear trend, similar to the E11. This would indicate that the photocurrent at E22 also is proportional to the injected exciton density. The increase in photocurrent with excitation power is slightly larger on the E22 (a factor of 5) compared to the E11 (approximately a factor of 3).

8.3.2 Photocurrent response with thermal coupling to the environment

Environmental conditions has been found to effect the photocurrent response of graphene samples [8–10]. In order to here further investigate whether any contribution to the photocurrent from a thermal mechanism may exist in a semiconducting nanotube when excited on the E11 and E22, the photocurrent was studied as a function of gas pressure. If the photocurrent results from a thermal mechanism the magnitude of the photocurrent would depend on the thermal conditions during the measurement. With an exchange-gas in the measurement chamber, the heat sinking of the nanotube to the environment would be improved. By increasing the thermal coupling to the environment any photothermal contribution to the photocurrent would change in magnitude as a function of the exchange-gas pressure. Also, any contribution to the photocurrent from the photovoltaic effect would show negligible dependence on the exchange-gas pressure.

To investigate this hypothesis, we first measured the photocurrent maps on the E11 and E22 in vacuum. Thereafter, we introduced He gas in the measurement chamber. He gas has a thermal conductivity of $0.15 \text{ W m}^{-1} \text{ K}^{-1}$ at room temperature. The He gas in the measurement chamber would act as a heat sink to the carbon nanotube, similar to when a nanotube is in contact with a substrate. (Heat sinking of graphene samples through contact with substrates have shown to affect the thermal properties [9].) The photothermal properties of the carbon nanotube would hence be expected to be affected by the increased thermal coupling.

The photocurrent maps were remeasured with approximately 0.5 bars and 0.75 bars of He gas in the measurements chamber. The results are presented in figure 8.4. All photocurrent maps showed a resemblance of a two-fold pattern, representative for the photovoltaic effect. The magnitude of the photocurrent on the E11 decreases only slightly for increasing gas pressure, while the photocurrent magnitude on the E22 decreases by a factor of 2-3. The shape of the photocurrent

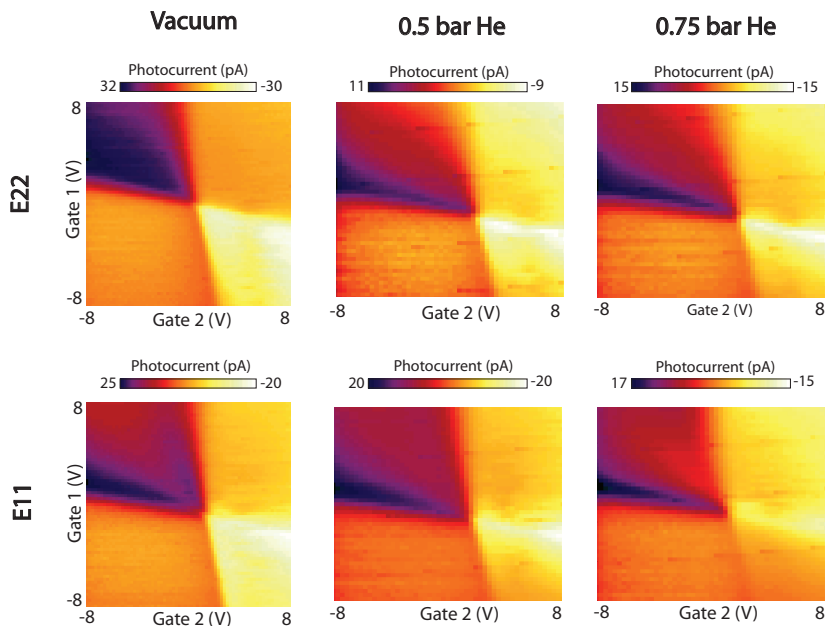


Figure 8.4: Gate dependent photocurrent response on the E11 and E22 with and without He exchange-gas. Photocurrent maps were measured in vacuum and with 0.5 and 0.75 bar of He exchange-gas introduced in the measurement chamber, in order to increase the thermal coupling of the carbon nanotube to the environment. The energy of the excitation laser was 1.36 eV and 0.84 eV, resonant with the E22 and E11 transitions, respectively. All photocurrent maps show a resemblance to the two-fold symmetry, representative of the photovoltaic mechanism. The polarization of the excitation laser was aligned along the nanotube axis and the excitation power used was $70 \mu\text{W}$.

maps is also slightly distorted from the traditional two-fold symmetry. However, we could still conclude that the photocurrent maps show a greater resemblance with the photovoltaic mechanism than with the photothermal mechanism.

8.4 Conclusions

In conclusion, the resonant photocurrent response from a semiconducting carbon nanotube has been investigated. We have found that the photovoltaic mechanism dominates the photocurrent response not only off resonance (as shown in chapter 7), but also when the semiconducting carbon nanotube is excited on

resonance with the E11 and E22. The effect of environmental conditions on the photocurrent was investigated by increasing the thermal coupling of the nanotube to the environment (analogous with having the nanotube in contact with a substrate). We found that the photovoltaic mechanism continued to dominate the photocurrent response both on the E11 and the E22 even with increased thermal coupling.

This concludes that the photovoltaic mechanism in semiconducting carbon nanotubes could not be tuned by the environmental parameters investigated in this study, nor was it altered by resonant excitation.

Bibliography

- [1] K. Balasubramanian, Y. Fan, M. Burghard and K. Kern. Photoelectronic transport imaging of individual semiconducting carbon nanotubes. *Appl. Phys. Lett.* **84**, 2400 (2004).
- [2] J. U. Lee, P. P. Gipp and C. M. Heller. Carbon nanotube p-n junction diodes. *Appl. Phys. Lett.* **85**, 145 (2004).
- [3] Y. H. Ahn, A. W. Tsen, B. Kim, Y. W. Park and J. Park. Photocurrent imaging of p-n junctions in ambipolar carbon nanotube transistors. *Nano Lett.* **7**, 3320 (2007).
- [4] F. Wang, G. Dukovic, L. E. Brus and T. F. Heinz. The optical resonances in carbon nanotubes arise from excitons. *Science* **308**, 838 (2005).
- [5] M. Barkelid and V. Zwiller. Photocurrent generation in semiconducting and metallic carbon nanotubes. *Nature Photon.* **8**, 47 (2014).
- [6] J. C. W. Song, M. S. Rudner, C. M. Marcus and L. S. Levitov. Hot carrier transport and photocurrent response in graphene. *Nano Lett.* **11**, 4688 (2011).
- [7] N. M. Gabor *et al.* Hot carrier-assisted intrinsic photoresponse in graphene. *Science* **334**, 648 (2011).
- [8] D. Sun *et al.* Ultrafast hot-carrier-dominated photocurrent in graphene. *Nature Nanotechn.* **7**, 114 (2012).
- [9] M. Freitag, T. Low and P. Avouris. Increased responsivity of suspended graphene photodetectors. *Nano Lett.* **13**, 1644 (2013).
- [10] M. Freitag, T. Low, F. Xia and P. Avouris. Photoconductivity of biased graphene. *Nature Photon.* **7**, 53 (2013).
- [11] M. S. Dresselhaus, G. Dresselhaus, R. Saito and A. Jorio. Exciton photo-physics of carbon nanotubes. *Annu. Rev. Phys. Chem.* **58**, 719 (2007).
- [12] J. Kong, H. T. Soh, A. M. Cassell, C. F. Quate and H. Dai. Synthesis of individual single-walled carbon nanotubes on patterned silicon wafers. *Nature* **395**, 878 (1998).
- [13] M. Barkelid, G. A. Steele and V. Zwiller. Probing optical transitions in individual carbon nanotubes using polarized photocurrent spectroscopy. *Nano Lett.* **12**, 5649 (2012).

- [14] G. Buchs, M. Barkelid, S. Bagiante, G. A. Steele and V. Zwiller. Imaging the formation of a p-n junction in a suspended carbon nanotube with scanning photocurrent microscopy. *J. Appl. Phys.* **110**, 074308 (2011).
- [15] Y. Miyauchi *et al.* Tunable electronic correlation effects in nanotube-light interactions. *arXiv:1308.5438* (2013).
- [16] K. Liu *et al.* High-throughput optical imaging and spectroscopy of individual carbon nanotubes in devices. *Nature Nanotechn.* (2013).
- [17] M. Y. Y. Kumamoto, A. Ishii, A. Yokoyama, T. Shimada and Y. K. Kato. Spontaneous exciton dissociation in carbon nanotubes. *arXiv:1307.5159* (2013).
- [18] K. Matsuda, T. Inoue, Y. Murakami, S. Maruyama and Y. Kanemitsu. Exciton dephasing and multiexciton recombinations in a single carbon nanotube. *Phys. Rev. B* **77**, 033406 (2008).
- [19] Y. Murakami and J. Kono. Existence of an upper limit on the density of excitons in carbon nanotubes by diffusion-limited exciton-exciton annihilation: Experiment and theory. *Phys. Rev. B* **80**, 035432 (2009).

Chapter 9

Large and Tunable Photothermoelectric Effect in Single-Layer MoS₂

Michele Buscema, Maria Barkelid, Val Zwiller, Herre S. J. van der Zant, Gary A. Steele, Andres Castellanos-Gomez

We study the photoresponse of single-layer MoS₂ field-effect transistors by scanning photocurrent microscopy. We find that, unlike in many other semiconductors, the photocurrent generation in single-layer MoS₂ is dominated by the photothermoelectric effect and not by the separation of photoexcited electron-hole pairs across the Schottky barriers at the MoS₂/electrode interfaces. We observe a large value for the Seebeck coefficient for single-layer MoS₂ that by an external electric field can be tuned between $-4 \cdot 10^2$ and $-1 \cdot 10^5 \mu\text{VK}^{-1}$. This large and tunable Seebeck coefficient of the single-layer MoS₂ paves the way to new applications of this material such as on-chip thermopower generation and waste thermal energy harvesting. ¹

¹This chapter has been published in *Nano Letters* **13**, 358-363 (2013).

9.1 Introduction

The experimental realization of graphene [1, 2] has opened the door not only to study exciting new phenomena but also to explore a whole new family of two-dimensional materials with complementary properties [3, 4]. For example, atomically thin semiconductor materials with a large bandgap are very interesting for electronic and optoelectronic applications where the lack of bandgap in graphene is hampering its applicability. Single-layer MoS₂ presents a large intrinsic bandgap (1.8 eV) [5–9], large in-plane mobility (200-500 cm²V⁻¹s⁻¹) [6] and remarkable mechanical properties [10, 11]. These properties are of great interest for sensors [12], flexible circuits [13, 14] and optoelectronic devices [15–17].

Recent works studying the optoelectronic properties of MoS₂ have shown that the photoresponse of externally biased MoS₂-based phototransistors is driven by the change in conductivity upon illumination [15–17]. The photovoltaic effect in MoS₂ devices has also been reported with metallic electrodes that generate large Schottky barriers (SBs) and poor electrical contacts [18, 19]. These previous works made use of either an externally applied or a built-in electric field to separate the photogenerated carriers.

Here, we employ scanning photocurrent microscopy to study the photocurrent generation mechanism in single-layer MoS₂ transistors with no Schottky barriers and no external bias. We demonstrate that in contrast to previous studies the photo-thermoelectric effect dominates the photoresponse in our devices. From our observations, we estimate the electric-field modulation of the Seebeck coefficient for single-layer MoS₂, finding a large value that can be tuned by more than 2 orders of magnitude.

9.2 Sample preparation and characterization

The devices consist of a single-layer MoS₂ flake, deposited onto a Si/SiO₂ (285 nm) substrate by mechanical exfoliation [3]. Electrical contacts have been fabricated by standard electron-beam lithography and subsequent deposition of a Ti(5 nm)/ Au(50 nm) layer. A combination of atomic force microscopy (AFM), Raman spectroscopy, and optical microscopy [20] has been used to characterize the MoS₂ samples. Figure 9.1a shows an AFM image of a field effect transistor (FET) fabricated with a single-layer MoS₂ flake. The line trace in Figure 9.1b shows that the height of the flake is around 0.9 nm in agreement with values previously reported in the literature [20]. Raman spectroscopy was also employed to further characterize the deposited MoS₂ layers [21–23]. As reported by C. Lee et al. [21] the frequency difference between the two most prominent Raman peaks depends monotonically on the thickness and it can therefore be used to accurately

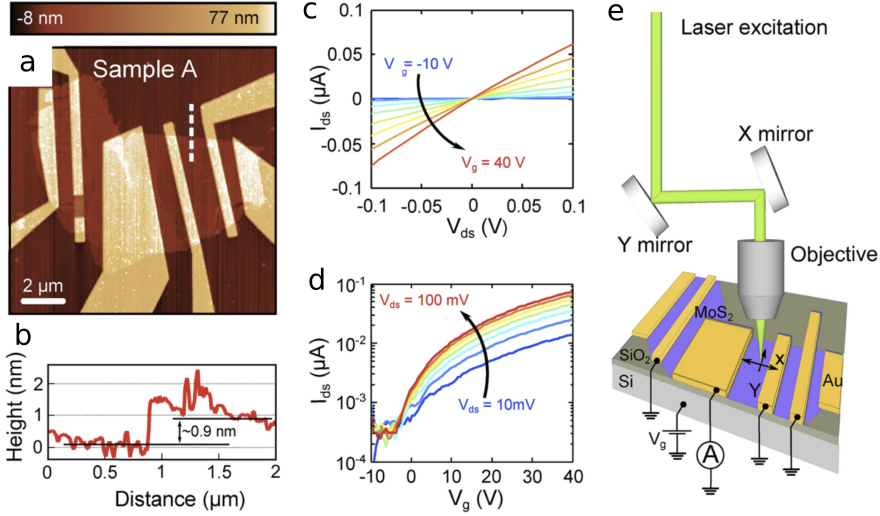


Figure 9.1: (a) Atomic force microscopy image of one of the studied devices, showing the MoS₂ flake and the electrodes used to make electrical contact. (b) Line profile over the dashed line in panel (a) showing the MoS₂ flake height. (c) Source-drain current versus source-drain bias characteristics measured at different gate voltages. (d) Electrical transport characteristic of a MoS₂-based FET device (source-drain current versus gate voltage) measured at different source-drain bias. For both panels (c) and (d), the channel length is 1.6 μm and width is 4.5 μm. (e) Schematic of the SPCM setup showing the excitation path and electric circuit used to perform SPCM measurements.

determine the number of MoS₂ layers. The Raman spectroscopy measurements confirm that our devices are single-layer MoS₂. In order to increase the quality of the electrical contacts, the samples were annealed at 300°C for two hours in a Ar/H₂ flow (500 sccm/100 sccm) [6]. Figure 9.1c shows source-drain characteristics of the single layer device at different gate voltages shown in Figure 9.1a. The current versus voltage relationship remains almost linear for a broad bias range, indicating that the conduction through the device is not dominated by Schottky barriers (SBs), which is in agreement with previous results by Radisavljevic et al. using similar electrode materials and annealing conditions [6]. Moreover, variable temperature transport experiments on MoS₂ using low work function electrodes (Ti and Sc) demonstrated a Schottky barrier height slightly larger than $k_B T$ at room temperature [24].

This is also consistent with recent density functional theory simulations and experimental work that demonstrate that Ti/MoS₂ interfaces provide ohmic contacts [25,26]. Figure 9.1d shows various gate traces measured at different source-

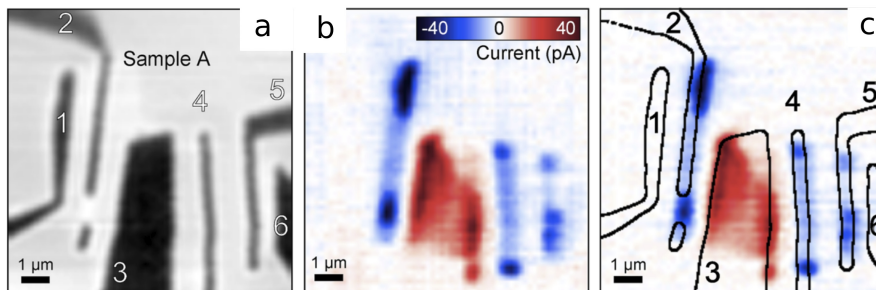


Figure 9.2: (a) Spatial map of the intensity of the reflected light from the device (white corresponds to low reflection). Electrodes have been numbered for clarity. (b) Photocurrent image of the MoS₂ FET. The colorscale in the inset gives the photocurrent value. (c) Superposition of the photocurrent map (from (b), same colorscale) and contours of the electrodes as obtained from the light reflection map. The scale bars are always 1 μm. Reflection and photocurrent measurements are performed simultaneously with electrode number 3 connected to a current to voltage amplifier while the other electrodes are connected to ground. Excitation is given by a CW laser, $\lambda = 532$ nm, $P = 1$ μW, spot waist radius ~ 400 nm. The region of the flake from the right edge of electrode 2 to the right edge of electrode 3 is composed by multiple layers of MoS₂ (see figure 9.5 for a more detailed description). No current is seen flowing from electrode 1 or 6 because of poor contact between those with the underlying MoS₂ flake.

drain voltages. The device shows a pronounced n-type behavior with a current on/off ratio exceeding 10^3 and a mobility of ~ 0.85 cm²V⁻¹s⁻¹, that is characteristic of single-layer MoS₂ FETs fabricated on SiO₂ surfaces [6, 12, 15, 26–28].

To spatially resolve the local photoresponse of the MoS₂-FET device, we performed scanning photocurrent microscopy (SPCM) in a home-built scanning confocal microscope (see Figure 9.1e) with excitation provided by a continuous wave green laser ($\lambda = 532$ nm) and a supercontinuum tunable source (at $\lambda = 750$ nm) [29]. In our experimental setup, the intensity of the reflected laser light (Figure 9.2a) and the photocurrent (Figure 9.2b) generated in the device are simultaneously recorded at every position during the scanning of the laser spot. It is thus possible to superimpose the two images to accurately determine where the photocurrent is generated (Figure 9.2c).

The gray scale image in Figure 9.2c shows the reflection image and the color-scale shows the simultaneously measured current flowing through the device at zero bias (electrode 3 is connected to a current-to-voltage amplifier while all other electrodes are connected to ground). As it can be seen (e.g., by looking at electrode 3), there is photogenerated current at zero bias even when the laser spot is placed inside the area of the electrodes, micrometers away from the electrode

edges, corresponding to distances up to 10 times larger than the full-width at half-maximum of the laser spot intensity profile. This is in striking contrast with several earlier findings on photocurrent on graphene [30, 31], which is localized at the interface between the graphene flake and the metal electrodes. In these previous works, the zero-bias photocurrent generation mechanism was attributed to the electron-hole separation at the SBs. This mechanism, however, cannot explain the presence of a photogenerated current when the laser is illuminating the metal electrodes, far from the electrode edges where SBs would be located.

The observation of photocurrent with the laser positioned deep inside the metal electrode suggests that the principal photocurrent generation mechanism in our device is different from photocurrent generation by the separation of photoexcited electron-hole pairs due to the localized electric field at the metal/semiconductor interface. This observation is also consistent with our conclusions from the data in Figure 9.1b that the SBs are not relevant for the transport characteristics of the device.

9.3 Photothermoelectric Effect in MoS₂

In order to gain a deeper insight into the photoresponse mechanism of single-layer MoS₂ FETs, we have performed scanning photocurrent measurements using different illumination wavelengths. Figure 9.3a shows a photoresponse map acquired with green ($\lambda = 532$ nm, $h\nu = 2.33$ eV) illumination. The photovoltage is obtained by dividing the measured photocurrent by the device resistance, measured under the same illumination conditions. A line profile of the photocurrent measured along the dashed green line in Figure 9.3a is presented in Figure 9.3b as open blue circles. The solid red line is a Gaussian fit to the data corresponding to a diffraction limited laser spot. Notice that there is a significant photocurrent tail generated when the laser is scanned over the electrode (arrow in Figure 9.3b). This is again inconsistent with a response shifted into the MoS₂ region, as would be expected for a photovoltaic response from Schottky barriers.

Figure 9.3c shows a photoresponse map acquired with red ($\lambda = 750$ nm, $h\nu = 1.65$ eV) illumination. The photovoltage is calculated as in Figure 9.3a. Note that the photovoltage under green illumination is larger because of the lower reflectance (and thus higher absorption) of the gold electrodes for this wavelength. The observation of photoresponse even for photon energies lower than the bandgap (Figure 9.3c) cannot be explained by separation of photoexcited electron-hole pairs (see Figure 9.3e, top panel). Moreover, previous photoconductivity measurements in MoS₂ transistors under large source-drain bias have not shown any significant photoresponse for excitation wavelength above 700 nm (or below 1.77 eV) [15, 32]. This indicates that sub-bandgap impurity states are either not present or do not contribute to photocurrents, even in the presence

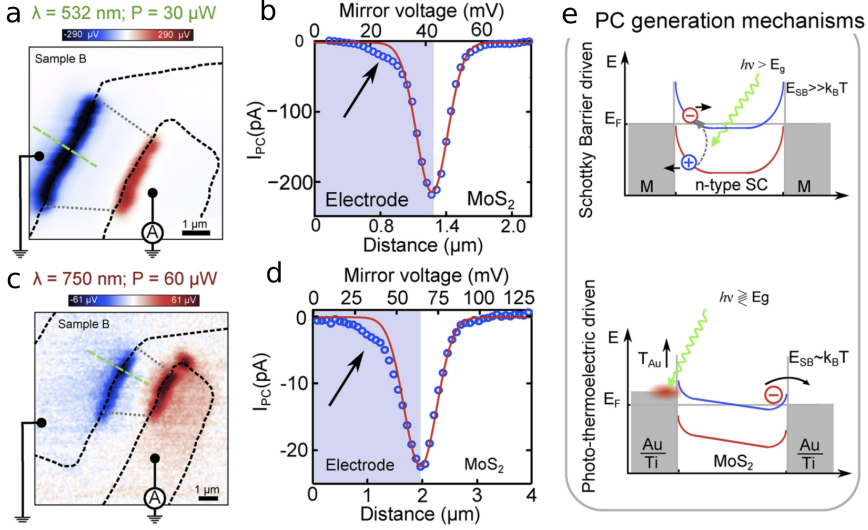


Figure 9.3: Photovoltage map of a single layer MoS₂ FET using an excitation wavelength of 532 nm (a) and 750 nm (c). (b,d) Photocurrent profile across the linecut in panels a,c (open blue circles). The solid red line is a Gaussian fit of the data and the arrow points at the photocurrent tail generated when the laser spot is scanned over the electrode. The shaded blue area represents the electrode area as determined by the reflection signal. (d) Schematic of photoresponse mechanism in a typical metal-semiconductor-metal device. (e) Schematic of the photoresponse mechanism in a device dominated by photothermoelectric effect. The conduction band is drawn in blue while the valence band is drawn in red.

of a large extraction bias, precluding sub-bandgap states as a possible source of photocurrent in Figure 9.3c. From these considerations, we conclude that the generation of photocurrent with excitation energies below the bandgap cannot be ascribed to a photovoltaic effect.

Interestingly, for above-bandgap illumination, where photovoltaic effects could play a role, the photocurrent images show characteristics that are qualitatively very similar to those for below bandgap illumination. A line profile of the photocurrent measured along the dashed green line in Figure 9.3c is presented in Figure 9.3d in the same fashion as in Figure 9.3b to facilitate the comparison. The qualitative agreement, and in particular the tail of photocurrent when the laser is focused over the metal, suggests that the photogeneration mechanism is not dominated by photovoltaic effects even for above-bandgap excitation. This hypothesis is also consistent with a lack of the gate dependence of the SPCM

images at above bandgap excitation energies ($\lambda = 532$ nm). In particular, the position of the maximum photocurrent in the photovoltaic effect would be expected to shift with the gate voltage, an effect also not observed in our devices (see Figure 9.6c). This also suggests that the main mechanism for photocurrent generation, even with above-bandgap illumination, is not the photovoltaic effect.

The negligible role of the SBs in the conductance of the devices, the strong measured photocurrent inside the area of the electrodes whose position is gate-independent and the observation of qualitatively identical photoresponse between sub and above-bandgap illumination all suggest that photovoltaic effects cannot be responsible for the photoresponse observed here. Instead, we propose that the photoresponse in our device arises from a strong photothermoelectric effect [33–37]. In the photothermoelectric effect (Figure 9.3e, bottom panel), a temperature gradient arising from light absorption generates a photothermal voltage across a junction between two materials with different Seebeck coefficient. This photothermovoltage can drive current through the device. This mechanism is consistent with our observation of strong photocurrents when the laser is focused on the metallic electrodes and also explains the presence of localized and intense photocurrent spots at the edges of the electrodes where the laser absorption is increased and the heat dissipation is reduced. Moreover, it would also explain the stronger photocurrent in the electrode area in Figure 9.2 where the MoS₂ underneath the electrode is more than one layer thick which reduces the thermal coupling with the substrate and thus increases the local temperature of the electrode (see section 9.3.1).

The photothermoelectric generation of current can be understood as follows: the local absorption of the laser creates a local heating of the junction between the gold and the MoS₂ layer. This local heating of the junction is translated into a voltage difference (ΔV_{PTE}), which will drive current through the device, by the difference between the Seebeck coefficients of the MoS₂ flake (S_{MoS_2}) and the electrodes (S_{TiAu}) and the local increase of the junction temperature (ΔT). This ΔT can be modeled as the temperature difference of the locally heated gold electrode (T_{Au}) and a part of the MoS₂ flake which is distant from the junction (T_{MoS_2}).

$$\begin{aligned} \Delta V &= (S_{MoS_2} - S_{TiAu})\Delta T \\ &= (S_{MoS_2} - S_{TiAu})(T_{MoS_2} - T_{TiAu}) \end{aligned} \tag{9.1}$$

9.3.1 Relationship between morphology and SPCM measurements

Figure 9.4 shows two optical micrographs of the studied MoS₂ FETs. The insets show the MoS₂ flakes as deposited on the SiO₂/Si substrate. The different con-

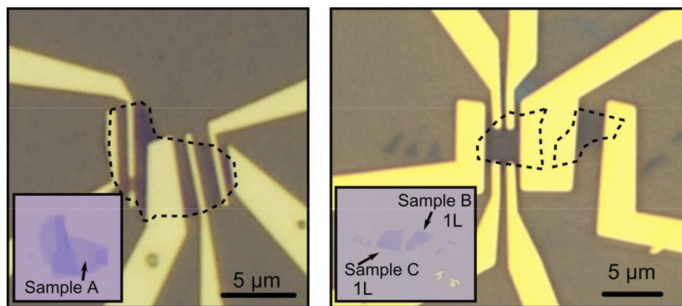


Figure 9.4: Optical micrograph of the 3 single-layer MoS₂ devices studied.

trast can be associated with different thicknesses in the same flake. The Ti/Au electrodes appear homogeneously reflective and this is an indication of good quality of the deposition and smoothness of the metallic surface.

Figure 9.5 shows the relationship between the morphology of the MoS₂ flake and the measured photocurrent. From panel (a) to (d) clockwise, the flake is contoured to show which regions are single layered (1L) or multi layered (>1L), then the electrodes from the optical image in Figure 9.4 are superimposed to the flake, then the SPCM data from Figure 9.2(b) are aligned with the electrodes and the flake. Finally the electrodes are removed. This process allowed to precisely determine which regions of the flake correspond to which value of measured PC. It is clearly visible that multilayer regions covered by the electrode have higher PC. This is due to the fact that multilayer MoS₂ is thermally decoupled from the substrate, allowing for a higher increase in temperature and, thus, a higher current (see Figure 9.2 and expression 9.2).

9.3.2 Gate dependent photocurrent spectroscopy

Figure 9.6(a) and (b) show a scanning photocurrent microscopy (SPCM) image (at zero source- drain bias) of one of the studied devices and a schematic of the electrical circuit used to measure the photocurrent, respectively. By performing SPCM measurements with gate voltages ranging from +30 V to -30 V, displayed in Figure 9.6(c), we determine that the position of the photocurrent peaks does not change (within experimental resolution) with respect to gate voltage. This is in contrast with earlier findings on devices in which the photocurrent is generated by the separation of photo-excited electrons and holes due to the electrostatic potential in p-n junctions or SBs whose extension depends on the charge carrier concentration. As the charge carrier density is reduced, the potential gradient would extend deeper into the material yielding a maximum photocur-

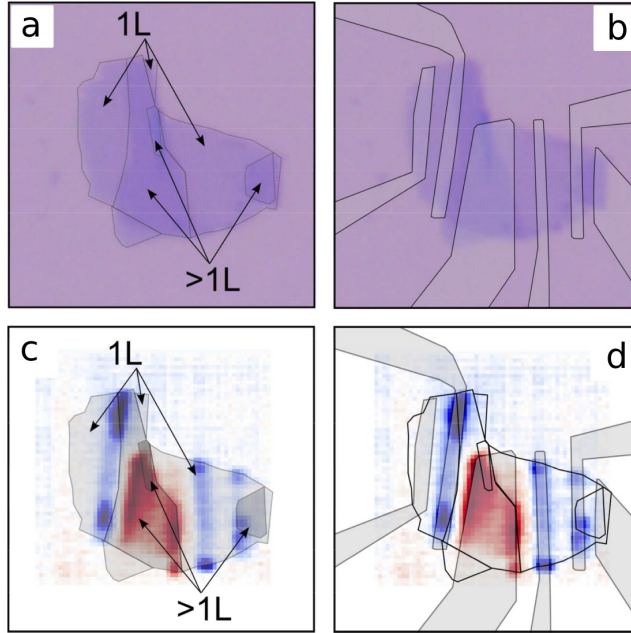


Figure 9.5: (a) MoS_2 flake with contours determined from the optical contrast indicating which regions are single layer (1L) or multilayers (>1L). (b) MoS_2 flake superimposed with the electrodes from Figure 9.4. (c) Data from SPCM superimposed to panel (b). (d) MoS_2 flake with contours indicating the number of layers and SPCM data obtained by removal of the electrodes.

rent further and further away from the electrode edges (see Figure 9.6(d)) [3–8]. Therefore, the absence of shift in the position of the measured photocurrent (see Figure 9.6(c)) demonstrates that the mechanism behind the generated photocurrent is not the separation of carriers by the built-in electrical potential along the SB near the electrodes and supports the proposed mechanism based on the photo-thermoelectric effect. As shown in Figure 9.6(e), the photo-induced temperature raise in the electrodes generates a voltage (ΔV_{PTE} , see expression 9.2) that can drive current through the device. This happens only when the laser is focussed onto the electrode surface as the absorption of laser light by the MoS_2 flake is negligible.

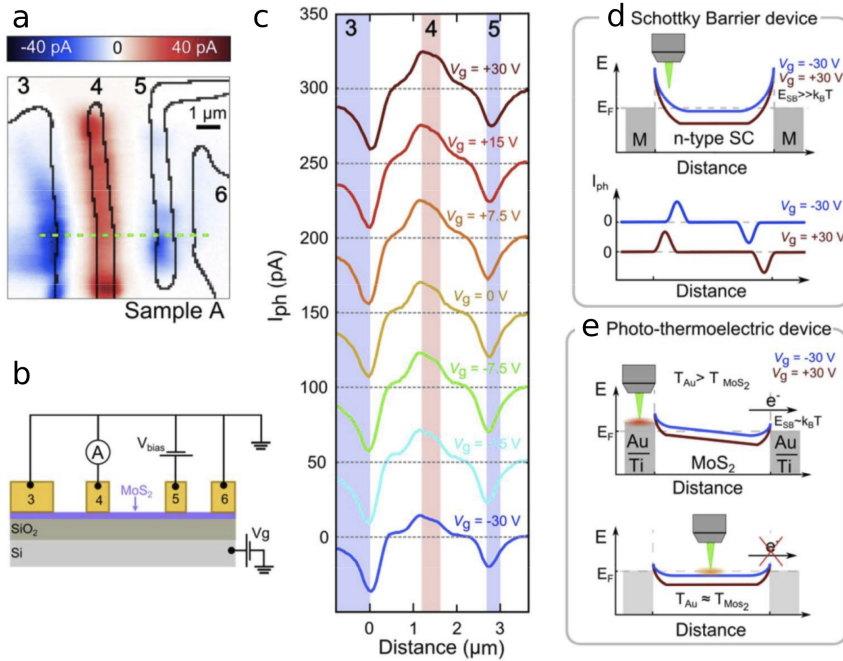


Figure 9.6: (a) Scanning photocurrent image of a single-layer MoS₂ FET taken at $\lambda = 532$ nm. Note that the current-to-voltage amplifier is connected to electrode 4, while electrode 3, 5 and 6 are connected to ground. (b) Schematic cross-section of the device, showing the electrical circuit used to perform the measurements. (c) Photocurrent line profiles (along the green dashed line in panel (a), $\lambda = 532$ nm) for gate voltages of +30, +15, +7.5, 0, -7.5, -15, -30 V from top to bottom. Consecutive lines are shifted by 50 pA for clarity. Shaded areas indicate the position and size of electrodes number 3, 4 and 5 as determined from the reflection signal; the colors of the shading indicates the sign of the photocurrent. (d) Schematic of the energy diagram of a typical Metal-Semiconductor-Metal device (top) and of the magnitude of a photocurrent line profile over such a device showing the expected gate-induced spatial shift in the photocurrent peak (bottom). (e) Schematic of the energy diagram of the single-layer MoS₂ device when the laser spot is incident on the electrode (top) and on the MoS₂ flake (bottom). In both panels (d) and (e) the conduction band is drawn at different gate voltages and the valence band is not shown for clarity.

9.4 Tunable Seebeck Effect in MoS₂

We have further studied the gate dependence of the photothermoelectric effect in single layer MoS₂ by measuring the electrical transport characteristics of single MoS₂ devices while the laser spot is placed at a location with high photoresponse. For illumination wavelengths with a photon energy higher than the bandgap, the threshold voltage is shifted toward very negative values (see Figure 9.7a) not reachable without leading to gate leakage. It is therefore preferable to use illumination wavelengths with photon energy below the bandgap to minimize this photoconductivity effect. Figure 9.7b shows the photothermoelectric voltage (ΔV_{PTE}) measured for a single-layer MoS₂ device at different gate voltages. The photothermoelectric voltage is the intercept with the voltage bias (V_{ds}) axis of the IV characteristic of the devices measured under sub-bandgap illumination. By decreasing the gate voltage below the threshold voltage, the photothermoelectric voltage shows a substantial increase. As the ΔV_{PTE} is proportional to the difference in the Seebeck coefficients and the temperatures of the AuTi electrodes and MoS₂ flake (expression 9.2), the observed behavior can be attributed to the expected gate dependence of the Seebeck coefficient of MoS₂.

At a microscopic level, the Seebeck effect is due to three microscopic processes that are in dynamic equilibrium with each other [38, 39]. The first process is the diffusion of electrons due to a steady state temperature gradient along a conductor; this process is proportional to the specific heat capacity of the electrons in the conductor. The second process is the variation of the chemical potential with temperature; this will modify the concentration of electrons along the temperature gradient and, therefore, induce a diffusive flux of electrons. The third process is the phonon-drag; as phonons diffuse from the warm side of the conductor to the cold side, they can scatter and drag along electrons. This process is proportional to the electron-phonon coupling and the specific heat of phonons. All these processes depend on or influence the density of states in the conductor. Therefore, they are bound to show a behavior which is dependent on an external gate electric field.

As it is difficult to experimentally determine microscopic properties such as the energy dependent density of states in a given sample, the Seebeck coefficient is often parametrized in terms of the conductivity of the sample using the Mott relation [40–43]

$$S = \frac{\pi^2 k_B^2 T}{3e} \left. \frac{d \ln(\sigma(E))}{dE} \right|_{E=E_F} \quad (9.2)$$

where k_B is the Boltzmann constant, T is the temperature, e is the electron charge, $\sigma(E)$ is the conductivity as a function of energy, and the derivative is evaluated at the Fermi energy E_F .

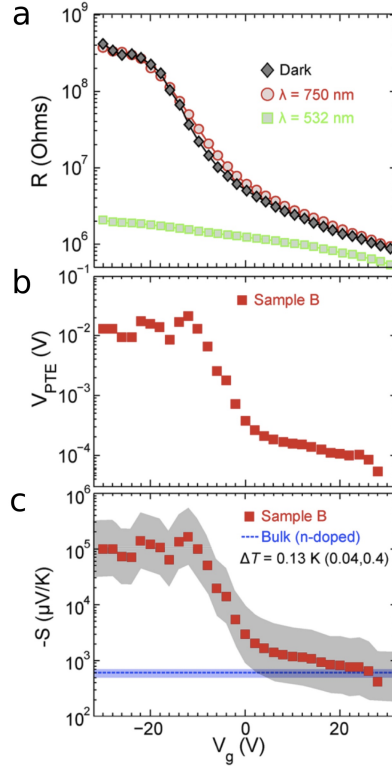


Figure 9.7: (a) Resistance of a single-layer MoS₂ device as a function of gate voltage in dark state and with the laser spot placed on the MoS₂/electrode interface. Two different illumination wavelengths have been used (532 and 750 nm). (b) Photothermoelectric voltage for a single-layer MoS₂ device measured with the laser spot ($\lambda = 750$ nm) placed on the MoS₂/electrode interface. (c) Estimated Seebeck coefficient versus gate voltage. The values are calculated from eq 1 using the measured photovoltage (symbols). The gray shaded area is the uncertainty due to the uncertainty in the estimation of the temperature gradient. The dashed light blue line corresponds to the Seebeck coefficient value of bulk MoS₂ with experimental uncertainty (shaded light blue area). The saturation effect at negative gate values is due to the high resistance of the device, leading to a current value below the noise floor of the current-to-voltage amplifier.

Using expression 9.2 we estimate the maximum Seebeck coefficient in our device to be on the order of $-0.2 \cdot 10^5 \mu\text{VK}^{-1}$, roughly an order of magnitude lower than the value we estimate from our measurements (see below). This discrepancy could arise from the fact that expression 9.2 is based on the assumption that the conductor is a metal or a degenerate semiconductor, which is not the case for a single flake of MoS₂ near depletion.

According to expression 9.2 the Seebeck coefficient of MoS₂ can be determined from ΔV_{PTE} and the estimate of the temperature gradient across the AuTi/MoS₂ junction. Notice that the Seebeck coefficient of AuTi is negligible with respect to that of MoS₂ and no gate dependence is expected. To estimate the increase of temperature induced by the laser illumination, we have performed a finite elements analysis calculation, taking into account the reflections losses in the objective and at the surface of the sample and the absorbed intensity through the material according to $I = I_0[1 - e^{-\alpha d}]$ where α is the absorption coefficient of the material and d is its thickness. With the employed laser excitation ($\lambda = 750 \text{ nm}$, $I_0 = 60 \mu\text{W}$, and $R_{spot} \approx 500 \text{ nm}$), if we assume that all the energy delivered by the laser is converted into heat we obtain $\Delta T_{AuTi/MoS_2} \approx 0.13 \text{ K}$. Figure 9.7c shows the estimated values; the experimental data are represented by squares while the shaded area represents the uncertainty in the estimation of the Seebeck coefficient deriving from an assumed uncertainty of a factor of 3 in the calculation of the temperature gradient (that is $\Delta T_{AuTi/MoS_2}$ in between 0.04 and 0.4 K). The Seebeck coefficient value for bulk MoS₂ (between ~ 500 and $\sim 700 \mu\text{VK}^{-1}$) is also plotted to facilitate the comparison [44]. A negative value of the Seebeck coefficient is expected for n-type semiconductors.

The obtained value for the Seebeck coefficient is remarkably large and varies strongly with the gate voltage from $-2 \cdot 10^2 \sim -1.5 \cdot 10^3 \mu\text{V/K}$ at high doping levels (high positive gate) to $-3 \cdot 10^4 \sim -3 \cdot 10^5 \mu\text{V/K}$ at low doping levels (high negative gate). Notice that at negative gate voltages, the Seebeck coefficient value saturates. This is due to the large resistance of the device at negative gate voltages that yields to a measured photocurrent that can be below the noise floor of the current amplifier (leading to the observed saturation in the estimated Seebeck coefficient).

The Seebeck coefficient that we observe for single-layer MoS₂ is orders-of-magnitude larger than that of graphene (± 4 to $100 \mu\text{VK}^{-1}$) [33, 34, 45–47], semi-conducting carbon nanotubes ($\sim -300 \mu\text{VK}^{-1}$) [48], organic semiconductors ($\sim 1 \cdot 10^3 \mu\text{VK}^{-1}$) [49] and even than materials regularly employed for thermopower generation such as BiTe ($\pm 150 \mu\text{VK}^{-1}$) [23, 50, 51]. On the other hand, the presented Seebeck coefficient is comparable with other materials such as MnO₂ powder ($20 \cdot 10^3 \sim 40 \cdot 10^3 \mu\text{VK}^{-1}$) [52] and Fe₂O₃ ($\pm 10 \cdot 10^3 \mu\text{VK}^{-1}$) [53]. In addition, the wide gate tunability of the Seebeck coefficient can be useful for applications such as on-chip power generation and thermoelectric nanodevices.

These applications include, but are not limited to, energy harvesting of waste thermal energy of other processes [54, 55] and to the possibility of developing autonomously powered devices [56, 57]. In all these applications, the tunability of the Seebeck coefficient represents an efficient way of optimizing device performances [56, 57].

9.5 Conclusions

In summary, using sub-bandgap illumination, we have demonstrated a clear and strong photothermoelectric effect arising from the large mismatch between the Seebeck coefficients of the MoS₂ and of the electrodes. Furthermore, the identical qualitative characteristics of the photocurrent images for above bandgap illumination suggests that the photothermal effect is also the dominant mechanism for photocurrent generation here as well, and that photovoltaic effects seem not to play a significant role. We estimated the Seebeck coefficient for single-layer MoS₂, finding a large value which can be tuned by an external electric field between $\sim -4 \cdot 10^2$ and $\sim -1 \cdot 10^5 \mu\text{VK}^{-1}$. This value is 70-25000 times larger than the values reported for graphene. From these results, we expect that single-layer MoS₂ could be an interesting complement to graphene in applications requiring a material with a large and tunable Seebeck coefficient, such as thermoelectric nanodevices or energy harvesting.

Bibliography

- [1] K. Novoselov *et al.* Electric field effect in atomically thin carbon films. *Science* **306**, 666 (2004).
- [2] K. Novoselov *et al.* Two-dimensional gas of massless dirac fermions in graphene. *Nature* **438**, 197 (2005).
- [3] K. Novoselov *et al.* Two-dimensional atomic crystals. *Proc. Natl. Acad. Sci. U.S.A.* **102**, 10451 (2005).
- [4] J. N. Coleman *et al.* Two-dimensional nanosheets produced by liquid exfoliation of layered materials. *Science* **331**, 568 (2011).
- [5] A. Ayari, E. Cobas, O. Ogundadegbe and M. S. Fuhrer. Realization and electrical characterization of ultrathin crystals of layered transition-metal dichalcogenides. *J. Appl. Phys.* **101**, 014507 (2007).
- [6] B. Radisavljevic, A. Radenovic, J. Brivio, V. Giacometti and A. Kis. Single-layer mos2 transistors. *Nature Nanotechn.* **6**, 147 (2011).
- [7] K. F. Mak, C. Lee, J. Hone, J. Shan and T. F. Heinz. Atomically thin mos2: A new direct-gap semiconductor. *Phys. Rev. Lett.* **105**, 136805 (2010).
- [8] A. Splendiani *et al.* Emerging photoluminescence in monolayer mos2. *Nano Lett.* **10**, 1271 (2010).
- [9] G. Eda *et al.* Photoluminescence from chemically exfoliated mos2. *Nano Lett.* **11**, 5111 (2011).
- [10] S. Bertolazzi, J. Brivio and A. Kis. Stretching and breaking of ultrathin mos2. *ACS Nano* **5**, 9703 (2011).
- [11] A. Castellanos-Gomez *et al.* Elastic properties of freely suspended mos2 nanosheets. *Adv. Mater.* **24**, 772 (2012).
- [12] H. Li *et al.* Fabrication of single- and multilayer mos2 film-based field-effect transistors for sensing no at room temperature. *Small* **8**, 63 (2012).
- [13] J. Pu *et al.* Highly flexible mos2 thin-film transistors with ion gel dielectrics. *Nano Lett.* **12**, 4013 (2012).
- [14] Q. He *et al.* Fabrication of flexible mos2 thin-film transistor arrays for practical gas-sensing applications. *Small* **8**, 2994 (2012).
- [15] Z. Yin *et al.* Single-layer mos2 phototransistors. *ACS Nano* **6**, 74 (2012).

- [16] H. S. Lee *et al.* Mos2 nanosheet phototransistors with thickness-modulated optical energy gap. *Nano Lett.* **12**, 3695 (2012).
- [17] W. Choi *et al.* High-detectivity multilayer mos2 phototransistors with spectral response from ultraviolet to infrared. *Adv. Mater.* **24**, 5832 (2012).
- [18] M. Fontana *et al.* Photovoltaic effect in gated mos2 schottky junctions. *arXiv:1206.6125* (2012).
- [19] M. Shanmugam, C. A. Durcan and B. Yu. Layered semiconductor molybdenum disulfide nanomembrane based schottky-barrier solar cells. *Nanoscale* **4**, 7399 (2012).
- [20] A. Castellanos-Gomez, N. Agrait and G. Rubio-Bollinger. Optical identification of atomically thin dichalcogenide crystals. *Appl. Phys. Lett.* **96**, 213116 (2010).
- [21] C. Lee *et al.* Anomalous lattice vibrations of single-and few-layer mos2. *ACS Nano* **4**, 2695 (2010).
- [22] T. Korn, S. Heydrich, M. Hirmer, J. Schmutzler and C. Schüller. Low-temperature photocarrier dynamics in monolayer mos2. *Appl. Phys. Lett.* **99**, 102109 (2011).
- [23] D. J. Late, B. Liu, H. S. S. R. Matte, C. N. R. Rao and V. P. Dravid. Rapid characterization of ultrathin layers of chalcogenides on sio2/si substrates. *Adv. Funct. Mater.* **22**, 1894 (2012).
- [24] S. Das, H.-Y. Chen, A. V. Penumatcha and J. Appenzeller. High performance multilayer mos2 transistors with scandium contacts. *Nano Lett.* **13**, 100 (2013).
- [25] I. Popov, G. Seifert and D. Tomańek. Designing electrical contacts to mos2 monolayers: A computational study. *Phys. Rev. Lett.* **108**, 156802 (2012).
- [26] S. Ghatak, A. N. Pal and A. Ghosh. Nature of electronic states in atomically thin mos2 field-effect transistors. *ACS Nano* **5**, 7707 (2011).
- [27] A. Castellanos-Gomez *et al.* Laser-thinning of mos2: On demand generation of a single-layer semiconductor. *Nano Lett.* **12**, 3187 (2012).
- [28] H. Liu and P. D. Ye. Mos2 dual-gate mosfet with atomic-layer-deposited al2o3 as top-gate dielectric. *IEEE Electron Device Lett.* **33**, 546 (2012).
- [29] G. Buchs, M. Barkelid, S. Bagiante, G. A. Steele and V. Zwiller. Imaging the formation of a pn junction in a suspended carbon nanotube with scanning photocurrent microscopy. *J. Appl. Phys.* **110**, 074308 (2011).

- [30] F. Xia *et al.* Photocurrent imaging and efficient photon detection in a graphene transistor. *Nano Lett.* **9**, 1039 (2009).
- [31] J. Park, Y. H. Ahn and C. Ruiz-Vargas. Imaging of photocurrent generation and collection in single-layer graphene. *Nano Lett.* **9**, 1742 (2009).
- [32] K. F. Mak, C. Lee, J. Hone, J. Shan and T. F. Heinz. Atomically thin mos2: A new direct-gap semiconductor. *Phys. Rev. Lett.* **105**, 136805 (2010).
- [33] X. Xu, N. M. Gabor, J. S. Alden, A. M. van der Zande and P. L. McEuen. Photo-thermoelectric effect at a graphene interface junction. *Nano Lett.* **10**, 562 (2010).
- [34] N. M. Gabor *et al.* Hot carrier-assisted intrinsic photoresponse in graphene. *Science* **334**, 648 (2011).
- [35] J. C. W. Song, M. S. Rudner, C. M. Marcus and L. S. Levitov. Hot carrier transport and photocurrent response in graphene. *Nano Lett.* **11**, 4688 (2011).
- [36] B. St-Antoine, C. Meñard and R. Martel. Photothermoelectric effects in single-walled carbon nanotube films: Reinterpreting scanning photocurrent experiments. *Nano Research* **5**, 73 (2012).
- [37] D. Sun *et al.* Ultrafast hot-carrier-dominated photocurrent in graphene. *Nature Nanotechn.* **7**, 114 (2012).
- [38] D. K. C. MacDonald. *Thermoelectricity: an introduction to the principles.* Wiley, New York (1962).
- [39] N. W. Ashcroft and N. D. Mermin. *Solid state physics.* Saunders College, Philadelphia (1976).
- [40] N. F. Mott and H. Jones. *The theory of the properties of metals and alloys.* The Clarendon Press, Oxford (1936).
- [41] B. Bhushan. *Springer Handbook of Nanotechnology.* Springer, New York (2007).
- [42] J. P. Heremans *et al.* Enhancement of thermoelectric efficiency in pbte by distortion of the electronic density of states. *Science* **321**, 554 (2008).
- [43] G. S. Nolas, J. Sharp and J. Goldsmid. *Thermoelectrics: Basic Principles and New Materials Developments.* Springer, New York (2001).
- [44] R. Mansfield and S. A. Salam. Electrical properties of molybdenite. *Proc. Phys. Soc. B* **66**, 377 (1953).

- [45] J. H. Seol *et al.* Two-dimensional phonon transport in supported graphene. *Science* **328**, 213 (2010).
- [46] K. L. Grosse, M.-H. Bae, F. Lian, E. Pop and W. P. King. Nanoscale joule heating, peltier cooling and current crowding at graphene–metal contacts. *Nature Nanotechn.* **6**, 287 (2011).
- [47] Z. Wang *et al.* Thermal transport in suspended and supported few-layer graphene. *Nano Lett.* **11**, 113 (2011).
- [48] J. P. Small, K. M. Perez and P. Kim. Modulation of thermoelectric power of individual carbon nanotubes. *Phys. Rev. Lett.* **91**, 256801 (2003).
- [49] K. P. Pernstich, B. Rossner and B. Batlogg. Field-effect-modulated seebeck coefficient in organic semiconductors. *Nature Mater.* **7**, 321 (2008).
- [50] J. P. Fleurial, L. Gailliard, R. Triboulet, H. Scherrer and S. Scherrer. Thermal properties of high quality single crystals of bismuth telluride—part i: Experimental characterization. *J. Phys. Chem. Solids* **49**, 1237 (1988).
- [51] A. L. Bassi *et al.* Thermoelectric properties of bi-te films with controlled structure and morphology. *J. Appl. Phys.* **105**, 124307 (2009).
- [52] S. FangFang, W. Liming and S. Liang. Giant seebeck coefficient thermoelectric device of mno₂ powder. *Nanotechnology* **23**, 085401 (2012).
- [53] R. F. G. Gardner, F. Sweett and D. W. Tanner. The electrical properties of alpha ferric oxide-i.: The impure oxide. *J. Phys. Chem. Solids* **24**, 1183 (1963).
- [54] L. E. Bell. Cooling, heating, generating power, and recovering waste heat with thermoelectric systems. *Science* **321**, 1457–1461 (2008).
- [55] I. Chowdhury *et al.* On-chip cooling by superlattice-based thin-film thermoelectrics. *Nature Nanotechn.* **4**, 235 (2009).
- [56] W. Liang *et al.* Field-effect modulation of seebeck coefficient in single pbse nanowires. *Nano Lett.* **9**, 1689 (2009).
- [57] H. Ohta *et al.* Field-modulated thermopower in srtio-based field-effect transistors with amorphous 12cao-7alo glass gate insulator. *Appl. Phys. Lett.* **95**, 113505 (2009).

Chapter 10

Conclusions and Outlook

In this chapter we will briefly summarize the results of this thesis and put them into a broader context. We will discuss future directions building on the knowledge we have retrieved or complementing the experiments presented in this thesis. Thereafter the current status of the field of carbon nanotube optoelectronics will be discussed and the future of this field reflected upon.

10.1 Summary and Conclusions

The experiments in this thesis were designed to gain an increased knowledge about light matter interaction in carbon nanotubes.

We employed the techniques of scanning photocurrent microscopy (SPCM) and photocurrent spectroscopy to probe the physics in a carbon nanotube p-n junction. The carbon nanotubes used were fabricated to be ultra-clean, in order to avoid disorder and impurity sites. The p-n junction was chosen as the device platform as it is a key component in applications where energy is transferred between photons and electrons, such as photodetectors, light-emitting-diodes and solar cells.

First we demonstrated the high degree of control we can achieve over our device with electrostatic doping and show how we can use SPCM to study the spatial evolution of the p-n junction. We continue to study the physical properties of semiconducting carbon nanotubes. Using photocurrent spectroscopy we can probe the optical resonances in the carbon nanotube. We show that the polarization dependence of the photocurrent gives information about the dielectric constant of the carbon nanotube, a fundamental property which up until now was commonly used as a fitting parameter could now be experimentally de-

terminated. By studying the photocurrent on and off resonance with the E11 and E22, a lower limit for a quantitative number for the absorption coefficient was obtained. The absorption coefficient in carbon nanotubes was previously addressed on a relative scale in units of cm^2/mole [1, 2]. These numbers were measured for nanotubes in solution and cannot be readily translated to individual suspended carbon nanotubes.

Thereafter we continue to exploit the optical resonances, as this is an extraordinary feature, differing carbon nanotubes from conventional optical systems such as quantum dots and nanowires. We now show that these resonances can be useful for developing applications based on carbon nanotubes, such as photovoltaic devices.

We then carry out a study on both semiconducting and metallic carbon nanotubes in identical device configurations and go to the bottom of the underlying mechanism for photocurrent generation in carbon nanotubes. By studying the photocurrent as a function of charge carrier doping two different mechanisms become apparent. In metallic carbon nanotubes the photocurrent is a result of a dominating photothermal effect, while in semiconducting carbon nanotubes it predominately arise from the photovoltaic effect.

We then continue to explore the photocurrent generation in a semiconducting nanotube and found that the photovoltaic mechanism continues to dominate the photocurrent response when the nanotube is excited on resonance with the E11 and E22. Additionally an increased thermal coupling between the nanotube and the environment did not show any signs of altering the dominant photocurrent generation mechanism in the semiconducting carbon nanotube.

Finally we expand our research to a different material system, MoS_2 . Photocurrent studies on a single layer MoS_2 device shows that in this system the photocurrent generation is due to the photothermal effect.

10.2 Future Directions

Here we give some suggestions for improvements on the existing device design and discuss a selection of future experiments which can be of interest in the field of carbon nanotube optoelectronics.

Improvements on Current Device Design

The current device design of a suspended contacted carbon nanotube with trench gates for electrostatic doping could be improved in a number of ways. For a start it could prove useful to increase the spacing between the trench gates. With a larger spacing (perhaps in the order of 500 nm to 1 μm) the junction would

become a p-i-n junction instead of a p-n junction. This would reduce band-to-band tunneling and could improve the diode characteristic of the device.

One could also consider to reduce the depth of the trench over which the carbon nanotube rests. The depth of the trench was designed to accommodate the slack of the carbon nanotube as such a long segment is air-suspended. However with a reduced trench depth the gates would have a stronger influence over the potential landscape of the carbon nanotube. One approach to realize this could be to use stamping of the carbon nanotubes [3, 4] onto a prefabricated device structure. This would minimize slack of the suspended carbon nanotube and the trench depth could therefore be reduced, bringing the nanotube in closer proximity to the gates.

Another important feature of improvement of the p-n device is the contacts. The quality of the contact is a major source of poor device characteristics. The contact material currently used is Pt which has a work function that lies in the valence band of the carbon nanotube. That means it makes a good p-type contact, but a poor n-type contact. It would be a good idea to use two different metals for the p- and n-contact. Suitable material for a n-type contact could for example be Ca [5], Sc [6] or Y [7].

To improve the contact resistance of our existing contacts a small amount of Pd could be introduced together with the Pt to make an alloy. If the amount of Pd is kept sufficiently small it could improve the quality of the contact (reduce the contact resistance) without reducing the ability for the metal to withstand high temperatures (as currently during the CVD process, see chapter 3).

The contact resistance may also be reduced through annealing [8, 9]. The best option would then be to have a four terminal device, such that a current can be passed through the metal electrodes, but not through the carbon nanotube. Local current annealing would be advantageous to global thermal annealing as it would only address the metal contacts and minimally affect the carbon nanotube.

Continued Exploration of the Photocurrent Generation Mechanism

The investigation of the underlying photocurrent generation mechanisms in carbon nanotubes (chapter 7) could be expanded further to for example include some of the ideas mentioned here, as well as probably many other aspects which we will see in the near future.

In carbon nanotubes the photothermal and the photovoltaic mechanism are both present, however one of the effects is responsible for the dominating contribution to the photocurrent generation in the respective nanotube species. It could be interesting to investigate the dominating photocurrent generation mechanism as a function of carbon nanotube diameter. For large band gaps the photovoltaic effect would dominate, however, as the nanotube band gap becomes comparable to kT the photothermal effect might start to play a role. Naturally the diameter

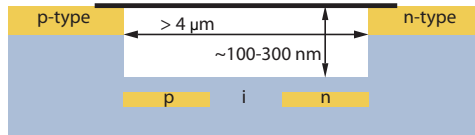


Figure 10.1: Schematic of improved device design. The contact material is selected to make one good p-type and one good n-type contact. The gates have a large separation so that the junction will turn into a p-i-n junction. The separation between the electrodes is long, to allow measurements of for example hot carrier cooling lengths and the depth of the trench is reduced in order to increase the coupling efficiency of the gates to the nanotube.

for when this change in photocurrent generation mechanism occurs will depend on measurement parameters such as the temperature.

Similarly, in a carbon nanotube with a small band gap, which shows signs of the photothermal mechanism at room temperature, it might show a change over to the photovoltaic mechanism when cooled down to a temperature where the small band gap becomes relatively large compared to kT .

With the help of a magnetic field a band gap could also be opened up in a 'nominally' metallic carbon nanotube [10] and a change from the photothermal (when the nanotube shows metallic characteristics) to the photovoltaic effect (when the band gap becomes large compared to kT) could be studied as a function of magnetic field.

Hot-Carrier Lifetime in Carbon Nanotubes

The life time of charge carriers can be probed using time-resolved measurements. Hot carriers in graphene is known to have a very long cooling length (approximately $5 \mu\text{m}$) and at the same time a long carrier life time (on the order of 100 ps) [11].

The lifetime of charge carriers in carbon nanotubes has been researched in the past and the measured decay times in lifetime measurements are in the order of picoseconds. However, as nanotubes suffer extensively from non-radiative recombination the actual lifetime of carriers after taking the quantum efficiency into account is in the order of nanoseconds.

In a metallic, or small bandgap, nanotube the photoexcited carriers become hot compared to the lattice. The lifetime of these hot carriers has not been measured in carbon nanotubes, but in graphene they have been found to stay hot for approximately $5 \mu\text{m}$ of traveling distance.

Pump-probe measurements could be performed on a metallic carbon nanotube

p-n junction. The ultimate limit of the cooling length of the hot carriers would be the presence of the contacts located $2 \mu\text{m}$ away from the junction (in the current device design). In order to measure the real cooling length of the hot carriers in metallic nanotubes the contacts of the device must be located far away from the junction.

It could also be interesting to study the charge carrier lifetime as a function of temperature. At low operating temperatures the Seebeck effect decreases, reducing the photocurrent, while the lifetime of the charge carriers increases, due to reduced scattering, which will increase the photocurrent. As we know that the photothermal effect dominates the photocurrent generation in our metallic nanotube down to 50 K (see chapter 7), we know that we are indeed probing hot carriers in our photocurrent measurements in the metallic carbon nanotube down to 50 K.

Exciton dissociation mechanism

The mechanism of exciton dissociation in carbon nanotubes is still an open question in the community. By now we have a lot of information about the exciton size, diffusion length and lifetime. However, the mechanism by which an excitation decomposes into free charge carriers is not clearly understood.

For this study it could prove informative to compare emission and absorption in the same nanotube and under the same measurement conditions. One way to do this is for example photocurrent and photoluminescence or electroluminescence measurements on the same carbon nanotube device. By studying the spectral shift, intensity or linewidth, important information could be obtained about the absorption and recombination processes of the excitons in carbon nanotubes.

Recent work by Y. Kato's group [12] on simultaneous photoluminescence and photocurrent experiments on a suspended carbon nanotube they find that a large fraction of injected excitons, through photoexcitation, undergo spontaneous dissociation into free electron-hole pairs.

Work by the groups of T. Heinz [13] and F. Wang [14] suggests that inter-subband scattering between the K and K' valley is another important factor to consider.

10.3 Current Status of the Field

The field of carbon nanotubes have developed rapidly since its discovery in 1991. Today, after more than 20 years of research, the field of carbon nanotube research show no sign of slowing down. One of the major research directions in the field is the synthesis of carbon nanotubes. A lot of effort is designated to improve the control of nanotube growth. Understanding the growth mechanism [15, 16]

is one aspect, and controlled chirality growth [17,18] is another. Here, optical techniques could be used in situ, as a probe, to study the synthesis [19].

Current 'hot' research questions are the implication of strain on the nanotube optical and electrical properties. Could strain be a problem or a possibility? In the optical community the absorption cross section of carbon nanotubes is a current matter of debate. This particular property has been measured by several research groups [1, 20, 21], everyone with a different result. Large systematic studies would be needed to answer the questions: "Is the absorption cross section chirality dependent? Should this parameter be expressed in terms of nanotube concentration or number of carbon atoms?" Finally, a large debate is ongoing concerning thermal effects in carbon nanotubes and how this would influence the electrical and optical properties.

The biggest challenge for carbon nanotubes, both from a research interpretation point of view, as well as for the step towards applications, is the (n,m) diversity. The multiple nanotube chiralities provide in equal measures a richness of the physics and complexity. Cloning carbon nanotubes in order to achieve consistent chirality [22] might in the future provide a viable approach for carbon nanotubes in applications.

In addition the field of nanotubes (and other carbon sciences) is starting to influence other research field, for example biology, where nanotubes, due to their small size can for example be used as sensitive probes for various usage.

10.4 Outlook

The field of carbon nanotube research is still moving forward at a rapid pace. What the future has in store one can only speculate in, however, a few calculated guesses will be described below:

Metrology will become increasingly important if nanotubes one day are going to attract the interest of industrial partners. This is also important for academic research in order to compare findings from different groups. We need to standardize techniques and analysis methods across the different disciplines, ranging from synthesis to electrical and optical characterization. If every research group applied a standardized method for Raman measurements or power efficiency calculations results from different groups could be more readily compared. A few standardized growth techniques for different purposes might generate an interest in using carbon nanotubes for application, rather than every research group using their own technique. This could pave the way for reliability and industrial quality of carbon nanotubes.

The challenges to this development is the difficulty in chirality control in the synthesis stage together with the nanotubes sensitivity to environmental effects and available instruments of sufficient resolution.

A relatively new branch of nanotube research which has emerged the last couple of years is double- and triple-walled carbon nanotubes (DWNT and TWNT). These structures provide a platform to study tube-tube interactions and are also interesting for application as they are more mechanically sturdy but behave similar to SWNTs. DWNT and TWNT can teach us a lot about intertube interaction as well as the physics of twisted layers. At the same time they add yet more flavors to the physics, in terms of combinations of metallic and semiconducting inner- and outer-tubes. What would be useful here (and is still lacking) is a Kataura plot for double- and triple-walled carbon nanotubes.

Another interesting future direction is how the deviation from the ideal carbon nanotube structure affects the optical and electronic properties of carbon nanotubes. For example what is the optical signature of certain defects? Or, how does the optical spectra change as a function of the environment surrounding the nanotube?

Yet one aspect which could enrich our knowledge about the fundamental properties and behaviours of carbon nanotubes is the combination of one or more measurements techniques. One step in that direction is the work in this thesis which combines optical and electrical measurements to study fundamental properties of carbon nanotubes. A second example which has generated some interest lately is opto-mechanics [23]. More exotic experiments might include gated-Raman spectroscopy or measurements with strain applied to the carbon nanotubes. One could also considering studying what influence features like Joule heating or C^{13} percentage have on the physical properties of carbon nanotubes.

A new aspect of carbon nanotube research which has started to emerge is injection of materials inside the carbon nanotubes. In this way nanotubes are exploited as tiny controlled laboratory environments, where research can be conducted. By this technique chirality specific nanotube have been synthesized [18], as well as diamond [24] and Eu nanowires [25].

New structures could be realized by combining carbon nanotubes and graphene and other nanoscale-materials into 'new' nano-materials and nanostructures.

For application of carbon nanotubes perhaps the most promising field is biomedicine. Rapid progress has been made in the group of H. Dai [26, 27] establishing biomedicine as the field where nanotubes has developed the furthest towards real life industrial use.

Bibliography

- [1] M. F. Islam, D. E. Milkie, C. L. Kane, A. G. Yodh and J. M. Kikkawa. Direct measurement of the polarized optical absorption cross section of single-wall carbon nanotubes. *Phys. Rev. Lett.* **93**, 037404 (2004).
- [2] S. Kuwahara, T. Sugai and H. Shinohara. Exact molar absorbance coefficients of single-wall carbon nanotubes. *Phys. Chem. Chem. Phys.* **11**, 1091 (2009).
- [3] F. Pei, E. A. Laird, G. A. Steele and L. P. Kouwenhoven. Valley–spin blockade and spin resonance in carbon nanotubes. *Nature Nanotechn.* **7**, 630 (2012).
- [4] C. C. Wu, C. H. Liu and Z. Zhong. One-step direct transfer of pristine single-walled carbon nanotubes for functional nanoelectronics. *Nano Lett.* **10**, 1032 (2010).
- [5] Y. Noshu, Y. Ohno, S. Kishimoto and T. Mizutani. n-type carbon nanotube field-effect transistors fabricated by using ca contact electrodes. *Appl. Phys. Lett.* **86**, 073105 (2005).
- [6] Z. Zhang *et al.* Doping-free fabrication of carbon nanotube based ballistic cmos devices and circuits. *Nano Lett.* **7**, 3603 (2007).
- [7] L. Ding *et al.* Y-contacted high-performance n-type single-walled carbon nanotube field-effect transistor: scaling and comparison with sc-contacted devices. *Nano Lett.* **9**, 4209 (2009).
- [8] J.-O. Lee *et al.* Formation of low-resistance ohmic contacts between carbon nanotube and metal electrodes by a rapid thermal annealing method. *J. Phys. D: Appl. Phys.* **33**, 1953 (2000).
- [9] Y. Woo, G. S. Duesberg and S. Roth. Reduced contact resistance between an individual single-walled carbon nanotube and a metal electrode by a local point annealing. *Nanotechnology* **18**, 095203 (2007).
- [10] H. Ajiki and T. Ando. Energy bands of carbon nanotubes in magnetic field. *J. Phys. Soc. Jpn.* **65**, 505 (1996).
- [11] N. M. Gabor. Photoresponse in graphene quantum devices: Hot dirac fermions and the emergence of nonlocality. *Workshop on Nanotube Optics and Nanospectroscopy* (2013).
- [12] Y. Kumamoto *et al.* Spontaneous exciton dissociation in carbon nanotubes. *doi:1307.5159v1* (2013).

- [13] Y. Miyauchi *et al.* Tunable electronic correlation effects in nanotube-light interactions. *arXiv:1308.5438* (2013).
- [14] K. Liu *et al.* High-throughput optical imaging and spectroscopy of individual carbon nanotubes in devices. *Nature Nanotechn.* (2013).
- [15] C. T. Wirth *et al.* The phase of iron catalyst nanoparticles during carbon nanotube growth. *Chem. Mater.* **24**, 4633 (2012).
- [16] V. Jourdain and C. Bichara. Current understanding of the growth of carbon nanotubes in catalytic chemical vapour deposition. *Carbon* **58**, 2 (2013).
- [17] M. He *et al.* Chiral-selective growth of single-walled carbon nanotubes on lattice-mismatched epitaxial cobalt nanoparticles. *Sci. Rep.* **3**, 1460 (2013).
- [18] H. EnLim. A chirality selective growth of carbon nanotubes via twisted graphene nanoribbons. *Fourteenth International Conference on Science and Applications of Nanotubes* (2013).
- [19] M. Picher *et al.* Influence of the growth conditions on the defect density of single-walled carbon nanotubes. *Carbon* **50**, 2407 (2012).
- [20] D. Y. Joh *et al.* Single-walled carbon nanotubes as excitonic optical wires. *Nature Nanotechn.* **6**, 51 (2010).
- [21] S. Berciaud, L. Cognet and B. Lounis. Luminescence decay and the absorption cross section of individual single-walled carbon nanotubes. *Phys. Rev. Lett.* **101**, 077402 (2008).
- [22] J. Liu *et al.* Chirality-controlled synthesis of single-walled carbon nanotubes using vapour-phase epitaxy. *Nature Commun.* **3**, 1199 (2012).
- [23] R. A. Barton *et al.* Photothermal self-oscillation and laser cooling of graphene optomechanical systems. *Nano Lett.* **12**, 4681 (2012).
- [24] J. Zhang *et al.* Synthesis and transformation of linear adamantane assemblies inside carbon nanotubes. *ACS Nano* **6**, 8674 (2012).
- [25] H. Shinohara. Carbon nanotube nanowires. *Fourteenth International Conference on Science and Applications of Nanotubes* (2013).
- [26] G. Hong *et al.* Multifunctional in vivo vascular imaging using near-infrared ii fluorescence. *Nature Medicine* **18**, 1841 (2012).
- [27] A. L. Antaris *et al.* Ultra-low doses of chirality sorted (6,5) carbon nanotubes for simultaneous tumor imaging and photothermal therapy. *ACS Nano* **7**, 3644 (2013).

Appendix A

Appendix to Chapter 7

This appendix addresses the influence of the chosen color scale on the photocurrent maps in chapter 7 of this thesis. We will here also examine the line profiles from all the five semiconducting nanotubes investigated in chapter 7. Finally we will present a more in depth study, containing new material, of the photocurrent response in a homogeneously doped semiconducting nanotube.

As explained in chapter 7, we do not rule out that photothermal and photovoltaic effects may simultaneously occur in carbon nanotubes, or that experimental conditions may influence which effect dominates the photocurrent response. A precise quantification of their relative contributions will require further work, that is beyond the scope this thesis. One experimental approach that can be applied to address this issue, is a study of the photocurrent in semiconducting nanotubes as a function of diameter (see chapter 10).

A.1 The effect of color scale choice on the photocurrent map

By tuning the color scale of the photocurrent map it may become apparent that a different mechanism dominates the photocurrent response. Figure A.1 shows the data from figure 7.5c displayed in two different color scales. It may be argued that figure A.1b shows evidence of a photothermal effect.

By considering the photocurrent pattern in figure A.1b we notice a weak color change in the bottom left quadrant. From a careful observation it appears as though this color change resembles a gradient rather than a six-fold symmetric pattern. We can therefore conclude that the dominating pattern in figure A.1b is two-fold symmetric (strong photocurrent from pn and np regions and negligi-

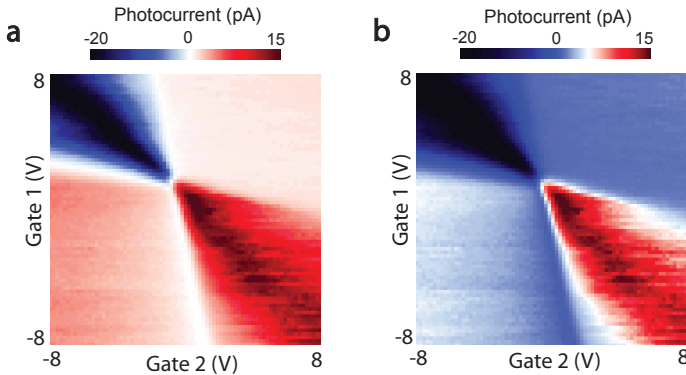


Figure A.1: Photocurrent map of the semiconducting carbon nanotube in figure 7.5c displayed in two different color scales. (a) Same color scale as in figure 7.5c. (b) A second color scale.

ble photocurrent from pp and nn regions). This is indicative of a photovoltaic mechanism.

Finally, it is also important to be careful when studying a color plot as it is easy to be mistaken by the strength of a signal. In order to get a clear idea of the magnitude of the signal one needs to study the line profiles.

A.2 Line profiles from the photocurrent response in a semiconducting carbon nanotube

In chapter 7 of this thesis a total of five semiconducting carbon nanotubes were investigated. For the sake of transparency we have here included four different line profiles from each one of the studied nanotubes, see figure A.2-A.6. The line profiles have been extracted from both the top and bottom of the photocurrent maps, showing the variation in photocurrent as a function of voltage on Gate 2, as well as vertical line profiles from the left and right side of the photocurrent maps, showing the variation in photocurrent as a function of voltage on Gate 1.

Close to the center of the photocurrent map the doping of the nanotube (induced by the fixed gate) would be negligible and any contribution to the electric field (or difference in Seebeck coefficients) from this gate would also be negligible. Therefore we do not extract the line profiles close to the center of the photocurrent maps.

We will now discuss each one of the semiconducting nanotubes in detail.

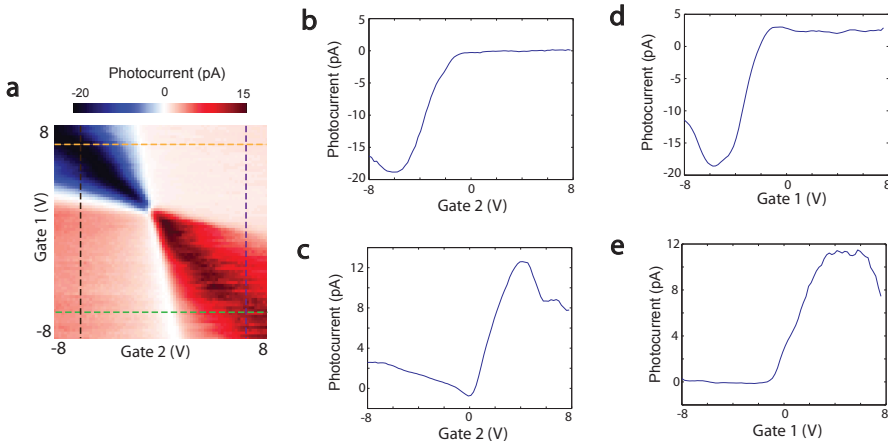


Figure A.2: Line profiles from semiconducting carbon **nanotube A**. Same figure as figure 7.5c of this thesis. (a) Photocurrent map. (b) Line profile along the yellow line. (c) Line profile along the green line. The photocurrent here shows a dip of 2 pA around zero gate voltage. (d) Line profile along the black line. (e) Line profile along the purple line.

A.2.1 Nanotube A

The photocurrent maps in figure A.2a shows a clear two-fold pattern, indicative of the photovoltaic effect. Figure A.2b-e show line profiles from the photocurrent map. The line profiles in (b),(d)-(e) show clear evidence of the photovoltaic mechanism as the photocurrent here only displays one polarity reversal. For a more detailed discussion about the signatures of the photovoltaic and photothermal mechanism, please see chapter 7 or [1–3].

The line profile in A.2c shows a dip in the photocurrent of approximately 2 pA around zero gate voltage. This data could be interpreted as an indication of the photothermal effect. However, when considering the magnitude of the signal and that there is no clear polarity change of the photocurrent, this could also be interpreted as an experimental fluctuation.

From the combination of the photocurrent pattern and line profiles we can conclude that the strongest effect in this nanotube (the dominating effect) is photovoltaic.

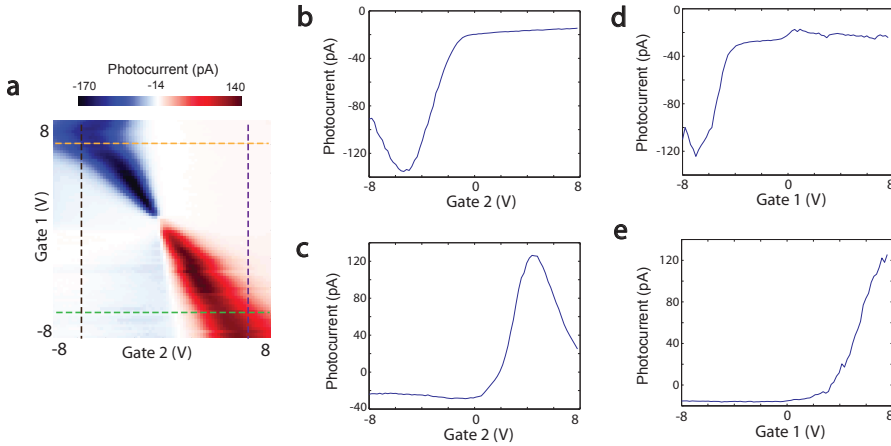


Figure A.3: Line profiles from semiconducting carbon nanotube **B**. (a) Photocurrent map. (b) Line profile along the yellow line. (c) Line profile along the green line. (d) Line profile along the black line. (e) Line profile along the purple line.

A.2.2 Nanotube B

In figure A.3 the photocurrent map shows a clear two-fold symmetry, indicative of the photovoltaic effect. All the line profiles in (b)-(e) shows a single polarity reversal, which is evidence of the photovoltaic effect. The conclusion from both the pattern in the photocurrent map and the four line profiles is therefore that the photovoltaic effect dominates the photocurrent response in this nanotube.

A.2.3 Nanotube C

Similarly in figure A.4 a very clear two-fold pattern can be observed in the photocurrent map. This pattern in the photocurrent provides evidence that the photocurrent generation mechanism is photovoltaic. From studying the line profiles presented in (b)-(c),(e) we can also see that the photocurrent only changes sign once. This single sign change has been derived as a fingerprint for the photovoltaic mechanism (see chapter 7 or [1] for details).

The line profile in figure A.4d could be interpreted as having a non-monotonic behavior. However, this effect is weak compared to the overlapping photovoltaic effect in the same line profile. Therefore we can conclude after considering both the pattern in the photocurrent as well as all four line profiles that the dominating effect in this nanotube is photovoltaic.

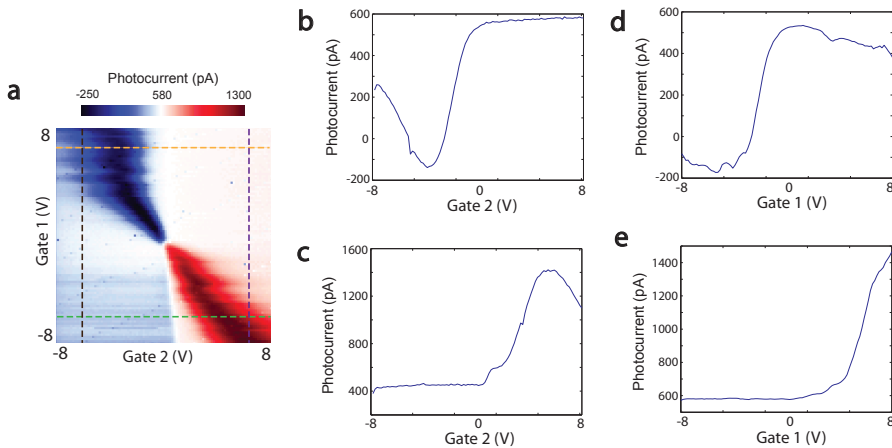


Figure A.4: Line profiles from semiconducting carbon **nanotube C**. (a) Photocurrent map. (b) Line profile along the yellow line. (c) Line profile along the green line. (d) Line profile along the black line. (e) Line profile along the purple line.

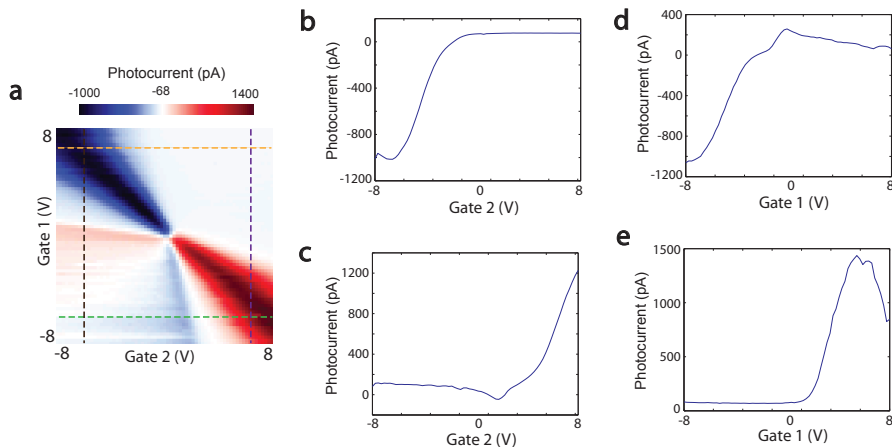


Figure A.5: Line profiles from semiconducting carbon **nanotube D**. (a) Photocurrent map. In the p-type doping regime a alternating polarity of the photocurrent is visible, which could be a sign of a photothermal mechanism. (b) Line profile along the yellow line. (c) Line profile along the green line. (d) Line profile along the black line. (e) Line profile along the purple line. In (c) and (d) we see that the sign change, which looked relatively strong in the color plot, has a relatively small magnitude compared to the photocurrent from the p-n and n-p regions.

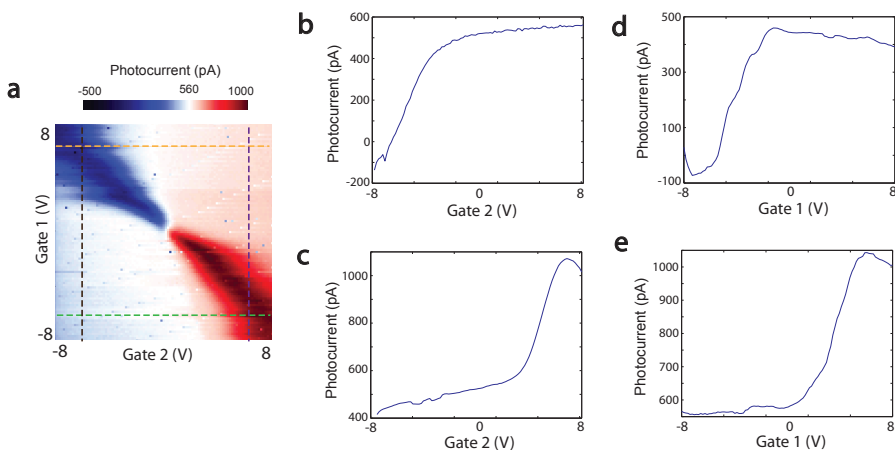


Figure A.6: Line profiles from semiconducting carbon **nanotube E**. (a) Photocurrent map. (b) Line profile along the yellow line. (c) Line profile along the green line. (d) Line profile along the black line. (e) Line profile along the purple line.

A.2.4 Nanotube D

In figure A.5a this nanotube shows alternating polarity of the photocurrent (in the p-type doping regime). This could be indicative of a possible photothermal mechanism. In order to quantify this contribution it is necessary to study the relative strengths of the signals. In figure A.5b-e the four line profiles from the nanotube are shown. The possible photothermal effect, which looked significant in the color plot of the photocurrent map, is shown as a dip (peak) around zero gate voltage in A.5c (d). We can now see that this contribution is rather small compared to the photocurrent from the p-n and n-p regions. We can therefore draw the conclusion that although present and possibly an indication of an overlapping photothermal effect, this dip/peak is not the dominating feature in A.5c-d.

Another important aspect to consider is that for a small band gap semiconducting carbon nanotube it is possible (and even expected) that a photothermal contribution will begin to show up and overlap with the photovoltaic effect. In order to investigate the relative contributions from the photovoltaic and the photothermal mechanisms one could for example study the photocurrent response for a range of different nanotube diameters (see chapter 10 for details).

A.2.5 Nanotube E

Figure A.6 shows the final nanotube investigated in this study. The photocurrent map shows clear evidence of a two-fold pattern, indicative of a photovoltaic effect. The line profiles in (b)-(c),(e) show a clear single polarity change in the photocurrent, which is evidence of a photovoltaic effect. The weak slope (between 0V and 8V) in the line profile in d could be interpreted as a weak photothermal effect overlapping with the photovoltaic effect. However, after considering all the line profiles as well as the pattern in the photocurrent map we can draw the conclusion that the photovoltaic effect dominates the photocurrent response from this nanotube.

A.3 Photocurrent from a homogeneously doped semiconducting carbon nanotube

We will now investigate the photocurrent generation mechanism in a homogeneously doped semiconducting nanotube (such as the one shown in figure 7.6a-c). A number of groups have been observing photocurrent features of changing polarity along the nanotube axis [3–5], but they were only recently addressed for the first time by DeBorde et al. [6]. DeBorde and coworkers have developed a model relating these features to a photothermoelectric effect in the carbon nanotube. We have therefore further investigated these photocurrent features in our device in light of this model.

A.3.1 Experiment

Figure A.7a shows a semiconducting carbon nanotube with a 2 μm wide trench, excited off resonance with a 532 nm c.w. laser. The polarization of the excitation light was first aligned parallel and then perpendicular to the nanotube axis, in order to eliminate any contributions to the photocurrent arising from heating the metal contacts [6]. The photocurrent map in figure A.7a shows the difference between the recorded photocurrent for parallel and perpendicular polarization ($I_{PC,\parallel} - I_{PC,\perp}$).

The gate voltage for the semiconducting nanotube was tuned from -15 V to +15 V in order to tune the doping of the nanotube from homogeneously p-type to homogeneously n-type. For every step in gate voltage the laser was scanned along the axis of the carbon nanotube. For p-type doping 4 regions of alternating polarity can be observed. While the two outermost regions of the photocurrent arise from focusing the laser at the nanotube / electrode interface, the two central regions show photocurrent generated as the laser is scanned along the axis of the p-doped nanotube. A line profile along the dashed green line is shown in

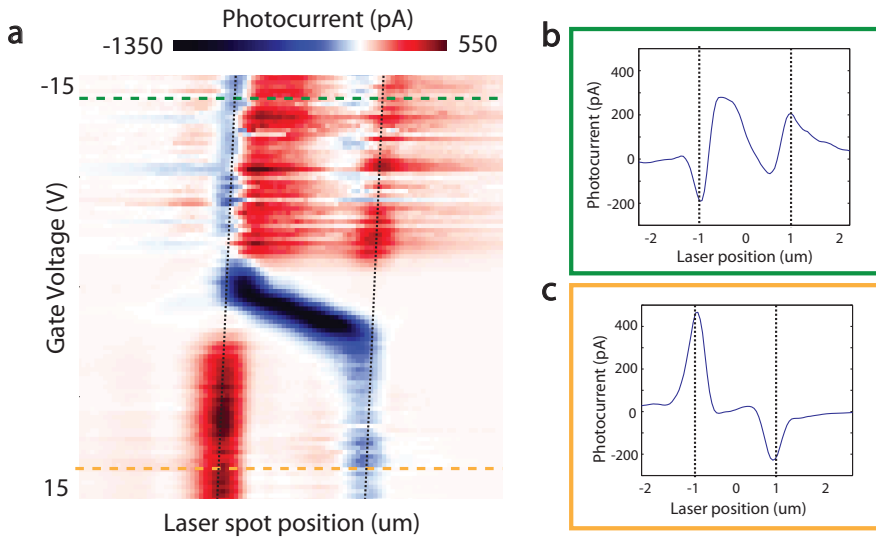


Figure A.7: Spatial and gate voltage dependent photocurrent response from a carbon nanotube FET structure. (a) The two trench gates, G1 and G2, are swept together from -15V to +15V. The excitation wavelength is off resonance, 532 nm, and the excitation power on the sample is $100 \mu\text{W}$. (b) A line profile along the dashed green line in (a). The device is here doped in a p-type configuration and shows 4 regions of alternating photocurrent polarity along the nanotube axis. (c) A line profile along the yellow dashed line in (a). The device is here doped in a n-type configuration and shows a photocurrent response from the nanotube/electrode interface.

figure A.7b. Here we can clearly see how the magnitude of the photocurrent contribution is comparable in magnitude between the four regions.

For n-type doping the photocurrent generated upon laser excitation at the nanotube / electrode interface dominates the photocurrent response. A line profile along the yellow dashed line is shown in figure A.7c. Here we can see how the photocurrent from the nanotube / electrode interface dominates. A very weak feature may be visible in the center of the n-doped nanotube in figure A.7c, however this signal is very weak compared to p-type doping. These photocurrent features in the center of the nanotube for n-type doping were only observed for an incident laser excitation of $300 \mu\text{W}$ (approximately $100 \mu\text{W}$ on the sample). For lower excitation powers these features could not be observed in the n-doped carbon nanotube.

A.3.2 Discussion

In the study by DeBorde et al. the photocurrent response from the homogeneously doped semiconducting nanotube displayed a photovoltaic mechanism both for n-type doping and for light p-type doping. This photocurrent response was generated when the laser was incident on the nanotube / electrode interface. For gate voltages larger than -3 V the photocurrent changed to the photothermal mechanism [6].

In our study we also observe a photovoltaic mechanism when the laser is incident on the nanotube / electrode interface, for n-type doping. This effect is then consistent as the doping configuration changes to p-type. We have applied heavy p-type doping (up to -15 V) and have yet not observed a change in the photocurrent from photovoltaic to photothermal (when the laser is incident on the interface). The current observation agrees with the conclusion from chapter 7 that the photocurrent generation mechanism at the nanotube / electrode interface, as a function of gate voltage for a homogeneously doped nanotube, is photovoltaic.

In the center of the semiconducting carbon nanotube in figure A.7a the photocurrent contribution has a different sign. It is possible that this photocurrent could arise from a photothermal mechanism. In the center of the homogeneously p-doped semiconducting nanotube there is no electric field which can separate the photoexcited carriers. Any contribution to the photocurrent from the photovoltaic effect would hence be quenched. This is an example where experimental conditions can suppress one of the photocurrent generation mechanisms.

The photothermal effect on the other hand is not suppressed. The Seebeck coefficient changes with doping and the induced doping in the nanotube by the gates is screened closed to the nanotube ends by the metal contacts. As a result the 'homogeneous doping of the nanotube may in fact not be completely homogeneous. This would provide a difference in the Seebeck coefficient between the ends and the center of the nanotube. This difference in Seebeck coefficient could give rise to a photothermal photocurrent showing up in the center of the nanotube where the photovoltaic effect is suppressed.

A.4 Conclusion

In conclusion the patterns in the photocurrent maps closely resemble the two-fold symmetric pattern which is the smoking-gun evidence of a photovoltaic effect [1]. The line profiles from the five investigated nanotubes predominantly shows a monotonic behavior with a single sign change as a function of gate voltage. In a homogeneously doped nanotube we find that the photovoltaic effect dominates at the nanotube/electrode interface.

The dominating photocurrent generation mechanism may be influenced by ex-

ternal factors [7, 8]. In this experiment the experimental conditions were chosen (see section 7.3.1 for details) such that neither the photovoltaic nor the photothermal mechanism would be suppressed and we could compare their relative contributions to the photocurrent.

For semiconducting nanotubes with a large band gap the photovoltaic effect would be expected to dominate, as it would be difficult to generate hot carriers with enough energy to overcome the band gap. As the band gap of the semiconducting nanotube becomes smaller and comparable to kT the photothermal effect might start to play a role and it could be possible to see an overlap of the two mechanisms. For yet smaller band gaps the photothermal mechanism would become dominant. In such a study it would also be important to determine how to classify small band gap semiconducting nanotubes versus metallic nanotubes.

An investigation of the relative strengths of the photovoltaic and photothermal effects in a semiconducting carbon nanotube is an important next step for the photocurrent community. An initial study investigating whether the photothermal and photovoltaic effect can occur simultaneously in a semiconducting nanotube is presented in chapter 8. These experiments did not provide positive proof for a dominant photothermal mechanism. However, these data do not exclude that, under different experimental conditions the photothermal mechanism may become dominant.

This important debate indicates the necessity for continued research in this field. Photocurrent in carbon nanotubes, as well as graphene and other 2D material, still has some open questions. This highlights the importance of continued careful investigation of if and how these two photocurrent generation mechanisms can be tuned and suppressed or enhanced.

Bibliography

- [1] J. C. W. Song, M. S. Rudner, C. M. Marcus and L. S. Levitov. Hot carrier transport and photocurrent response in graphene. *Nano Lett.* **11**, 4688 (2011).
- [2] N. M. Gabor *et al.* Hot carrier-assisted intrinsic photoresponse in graphene. *Science* **334**, 648 (2011).
- [3] M. Barkelid and V. Zwiller. Photocurrent generation in semiconducting and metallic carbon nanotubes. *Nature Photon.* **8**, 47 (2014).
- [4] K. Balasubramanian, Y. Fan, M. Burghard and K. Kern. Photoelectronic transport imaging of individual semiconducting carbon nanotubes. *Appl. Phys. Lett.* **84**, 2400 (2004).
- [5] Y. H. Ahn, A. W. Tsen, B. Kim, Y. W. Park and J. Park. Photocurrent imaging of p-n junctions in ambipolar carbon nanotube transistors. *Nano Lett.* **7**, 3320 (2007).
- [6] T. DeBorde, L. Aspirtarte, T. Sharf, J. W. Kevek and E. D. Minot. Photothermoelectric effect in suspended semiconducting carbon nanotubes. *ACS Nano* doi: **10.1021/nm403137a** (2013).
- [7] M. Freitag, T. Low, F. Xia and P. Avouris. Photoconductivity of biased graphene. *Nature Photon.* **7**, 53 (2013).
- [8] M. Freitag, T. Low and P. Avouris. Increased responsivity of suspended graphene photodetectors. *Nano Lett.* **13**, 1644 (2013).

Summary

Photocurrent in Carbon Nanotubes

Light-matter interaction at the nanoscale can exhibit many interesting physical phenomenas. It is also of great importance for designing devices which operate efficiently with low loss. Carbon nanotubes are excellent systems to carry out such work as they have very interesting optical properties which can be readily observed at room temperature.

In this thesis we explore light-matter interaction in a carbon nanotube p-n junction. Our main probing technique is photocurrent, which is based on the absorption of photons and extraction of electrical current. We use photocurrent as a sensitive probe to investigate the physical behavior of the carbon nanotubes under the influence of gate voltage, light polarization and spatial laser position.

In the first part of the thesis we use photocurrent as a tool for imaging of the potential landscape and spectral probing of the optical resonances in carbon nanotubes. These resonances are characteristic for carbon nanotubes and strongly influence the optical properties of the carbon nanotube. We find that we can employ these to investigate physical properties such as the absorption efficiency and the dielectric constant of the carbon nanotube. We also show that these resonances can be of interest for developing optoelectronic devices based on carbon nanotubes, such as solar cells.

In the second part of the thesis we focus on the effect of heating during optical excitation and explore how this alters the photocurrent response in carbon nanotubes (and other nanoscale systems, such as MoS_2). When a photon is absorbed it can either create an exciton (or a free electron-hole pair) or it can create a hot electron with a temperature much larger than the lattice temperature. Depending on which mechanism is dominant, different photocurrent response can be observed at the carbon nanotube p-n junction.

We present evidence that the photovoltaic mechanism dominates in semi-conducting carbon nanotubes while the photothermal mechanism dominates in metallic nanotubes. The two different photocurrent generation mechanisms in

metallic and semiconducting nanotubes are an important milestone in understanding the physical processes governing the optoelectronic response in carbon nanotubes.

The semiconducting carbon nanotube was additionally investigated under various experimental conditions, such as gate voltage and thermal coupling to the environment and the dominating photocurrent generation mechanism was found to be consistent with the photovoltaic effect.

Finally, photocurrent measurements were performed on a different material system, namely MoS₂, and the photocurrent in this 2D semiconductor was found to be a result of the photothermal mechanism.

A thorough understanding of the physical processes which govern the photoresponse in nanoscale systems may open the door to exploiting these processes for very efficient energy harvesting devices at the nanoscale.

Maria Barkelid
Delft, 2014

Samenvatting

Fotostroom in Koolstof Nanobuisjes

Licht-materie interactie op nanoschaal vertoont veel interessante fysische fenomenen. Het is van groot belang voor het ontwerpen van componenten die efficiënt werken met lage verliezen. Koolstof nanobuisjes zijn uitstekende systemen om dergelijk onderzoek uit te voeren omdat ze vele interessante optische eigenschappen bezitten die gemakkelijk kunnen worden waargenomen bij kamertemperatuur.

In dit proefschrift onderzoeken we licht-materie interactie in een koolstof nanobuis pn-overgang. Onze meetings techniek is fotostroom die is gebaseerd op de absorptie van fotonen en winning van elektrische stroom. Wij gebruiken fotostroom als een gevoelige techniek om het fysische gedrag van de koolstof nanobuisjes onder invloed van gate spanning, lichtpolarisatie en ruimtelijke laserpositie onderzoeken.

In het eerste deel van het proefschrift gebruiken we fotostroom als een instrument voor de beeldvorming van de potentiële landschap en spectrale sonderen van de optische resonanties in koolstof nanobuizen. Deze resonanties zijn karakteristiek voor koolstof nanobuisjes en zijn bepalend voor de optische eigenschappen van de nanobuis. We hebben ontdekt dat we deze resonanties kunnen gebruiken om fysische eigenschappen zoals absorptie-rendement en de diëlektrische constante te onderzoeken. We tonen ook aan dat deze resonanties van belang zijn voor het ontwikkelen van opto-elektronische apparaten op basis van koolstof nanobuisjes, zoals zonnecellen.

In het tweede deel van het proefschrift richten we ons op het effect van verwarming tijdens optische excitatie en onderzoeken we hoe dit de fotostroom respons in koolstof nanobuizen (en andere nanoschaal systemen, zoals MoS_2) verandert. Wanneer een foton geabsorbeerd wordt kan het een exciton (of een vrij elektron-gat paar) of het kan een heet elektron met een temperatuur die groter is dan de temperatuur van het atoomrooster creëren. Afhankelijk van welk mechanisme dominant is, kan een bepaalde fotostroom reactie worden waargenomen

op de koolstof nanobuis pn-overgang.

We presenteren het bewijs dat het fotonvoltaïsche mechanisme domineert in halfgeleidende koolstof nanobuisjes terwijl de fotothermale mechanisme domineert in metallische nanobuisjes. De twee verschillende fotostroom generatie mechanismen in metallische en halfgeleidende nanobuisjes zijn een belangrijke mijlpaal in het begrijpen van de fysische processen rond de opto-elektronische respons in koolstof nanobuizen.

De halfgeleidende koolstof nanobuis werd bovendien onderzocht onder verschillende experimentele condities, zoals gate spanning en thermische koppeling met de omgeving. Het overheersende mechanisme van fotostroom generatie bleek consistent het fotonvoltaïsch effect te zijn.

Tenslotte werden fotostroom metingen op een ander materiaalsysteem, namelijk MoS₂ uitgevoerd. De fotostroom in deze 2D halfgeleider bleek een gevolg van het fotothermische mechanisme te zijn.

Een goed begrip van de fysische processen die de foto-reactie bepalen in nanoschaal systemen kunnen nieuwe mogelijkheden ontsluiten voor zeer efficiënte energie oogstende apparaten op nanoschaal.

Maria Barkelid
Delft, 2014

Acknowledgement

The field of nanoscience has fascinated me since that first day I stepped into a lecture hall as an undergraduate student at Lund University. From that moment it was given that I would continue working in the field of nanoscience and I quickly developed a taste for experimental research, thanks to several people at the Solid State Physics department in Lund. By the time I finished my master in Engineering Nanoscience I knew I wanted to do a PhD, the question was only at which research institution and in which field.

In May 2010 I started my PhD research on carbon nanotube optoelectronics in the Quantum Transport group at Delft University of Technology. Looking back on seemingly endless late nights in the lab or frustrating clean-room sessions I can now say that PhD research was nothing like I expected it to be.

Throughout the past 4 years I have come to cross paths with a great many people who in one way or another have contributed to the work that has been presented in this thesis. Therefore I would like to seize this opportunity to thank these people, for without them this work would not have been possible.

First I would like to thank my supervisor. Val, thanks for giving me the freedom to define my own research direction and for letting me go my own way.

Secondly I would like to thank my promotor. Leo, you always inspire people around you to give their outmost. Thanks for teaching me to aim high.

Next to my supervisors several other people have been involved to various extents in my research. Gary, thanks for teaching me to be critical. Gilles, thanks for building a great measurement setup. Tang, we only overlapped for a short time in the beginning of my PhD. Thanks for showing me the ropes in the clean-room. Salvo, thanks for laying the foundation for the device fabrication.

In the beginning of my PhD I was fortunate to get to spend a few weeks in the lab of Jacques Lefebvre at the National Research Council in Ottawa, Canada. Jacques you taught me a lot about photoluminescence measurements on carbon

nanotubes, and about carbon nanotubes in general. Thank you.

Mark Rudner, you helped me a lot in shaping the photocurrent-generation-paper. I truly admire your knowledge and your ability to explain. Thanks for all the great scientific discussions. The paper would not have moved forward so efficiently without your help.

Andres, I truly admire your style of working and your productivity. I greatly enjoyed writing 2 papers with you and I have learnt a lot from your example. Good luck in Madrid! Michele, I enjoyed working with you on the MoS2 paper. Good luck with the rest of your PhD! I know you will do great.

Throughout the past years I have been lucky enough to have many amazing people around me who I can always turn to. Stephanie, thanks for being my rock and always having time for me. I don't think I would have survived the first 18 months without your support, and you have been a never ending source of hope and advice for me. Thank you!

Basia, thanks for being there for me and for always being on my side. Our conversations about work and life have meant a great deal to me and on countless times lifted my spirits when things looked very dark.

Maaïke, thanks for being an amazing friend. I am so impressed by your ability to combine research and motherhood. I have learnt a lot from you about being rational and keeping perspective on life. Thank you for all your support!

Kun, thanks for all the great times together. I'm very lucky to have you as a friend and your support has meant a great deal to me.

To all my other friends and colleagues in qt I would also like to extend a big Thank You! For both the fun times and the inspiring scientific discussions.

A great many people have helped me throughout the final preparation of my thesis. To whom I owe a great deal and without their dedication and commitment I would not have seen my defense day. Lieven, thanks for listening and for all your advice. Marc, thanks for your endless support and for all your time and efforts. Andreas, you always see a situation in the most positive light. I hope to learn a little bit of this skill from you. Thank you! Paula, thank you for never letting me lose hope. And for always believing in me. Joost, thank you for being there, prepared to support and assist. This has brought me a great deal of comfort.

I would also like to extend a thank you to all my other friends here in the Netherlands. Thank you for all the fun times together! The parties, bbqs, borrels, coffee-times, dinners and much more. It has made me feel so welcome here.

I would like to thank my family for supporting my choice to do a PhD (and deciding not to do this in Sweden). Thank you for all your support and patience with me over the past four years!

And finally, the light of my life, Johan. You are my never ending source of joy and happiness. You are my inspiration and guidance. If I ever wonder

what the meaning of these past four years was, I know it was to find you. The completion of this thesis would never have been possible without you by my side. To encourage, comfort and inspire. And for that I will be forever grateful. I am now looking forward to begin the rest of our lives.

Maria Barkelid
Delft, 2014

Curriculum Vitae

Karin Maria Barkelid

- 16 Oct. 1985 Born in Helsingborg, Sweden.
- 2001-2004 High School, Science Program, Helsingborg, Sweden.
- 2005-2010 M.Sc. in Engineering Nanoscience, Lund University, Faculty of Engineering, Sweden.
Undergraduate Reserch: *Characterization of vertical wrap-around gate InAs nanowire FET.*
Supervisor: Prof. L.-E. Wernersson
Master Thesis: *Single Silicon p-i-n Nanowire Avalanche Photodiodes for Single Photon Detection.*
Supervisor: Dr. V. Zwiller.
- 2008-2009 Education Abroad Program at University of California Santa Barbara, USA.
Undergraduate Research: *Molecular Beam Epitaxy of ErAs nanowires on GaAs 411*
Supervisor: Prof. C. Palmstrom
- 2010-2014 PhD in Physics, Delft University of Technology, The Netherlands.
Thesis: *Photocurrent in Carbon Nanotubes.*
Promotor: Prof. dr. ing. L. P. Kouwenhoven
Co-promotor: Dr. V. Zwiller

List of Publications

1. *Resonant Photocurrent Response in a Semiconducting Carbon Nanotubes*
In preparation
2. *Photocurrent Generation in Semiconducting and Metallic Carbon Nanotubes*
M. Barkelid and V. Zwiller.
Nature Photonics, **8**, p. 47-51 (2014)
3. *Single Carbon Nanotube Photovoltaic Device*
M. Barkelid and V. Zwiller.
Journal of Applied Physics, **114**, 164320 (2013)
4. *Large and Tunable Photothermoelectric Effect in Single-Layer MoS₂*
M. Buscema, M. Barkelid, V. Zwiller, H. S. J. van der Zant, G. A. Steele
and A. Castellanos-Gomez.
Nano Letters **13**, p. 358-363 (2013)
5. *Fast and Efficient Photodetection in Nanoscale Quantum Dot Junctions*
F. Prins, M. Buscema, J. S. Seldenthuis, S. Etaki, G. Buchs, M. Barkelid,
V. Zwiller, Y. Gao, A. J. Houtepen, L. D. A. Siebbeles and H. S. J. van der
Zant.
Nano Letters **12**, p. 5740-5743 (2012)
6. *Probing Optical Transistions in Individual Carbon Nanotubes Using
Polarized Photocurrent Spectroscopy*
M. Barkelid, G. A. Steele and V. Zwiller.
Nano Letters **12**, p. 5649-5653 (2012)
7. *Laser-Thinning of MoS₂: On Demand Generation of a Single-Layer
Semiconductor*
A. Castellanos-Gomez, M. Barkelid, A. M. Goossens, V. E. Calado, H. S.
J. van der Zant and G. A. Steele.
Nano Letters **12**, p. 3187-3192 (2012)

-
8. *Single semiconductor quantum dots in nanowires: growth, optics, and devices*
M.E. Reimer, N. Akopian, M. Barkelid, G. Bulgarini, R. Heeres, M. Hocevar, B.J. Witek, E.P.A.M. Bakkers, V. Zwiller
Quantum Dots: Optics, Electron Transport and Future Applications
Cambridge University Press (2012)
 9. *Imaging the Formation of a p-n Junction in a Suspended Carbon Nanotube with Scanning Photocurrent Microscopy*
G. Buchs, M. Barkelid, S. Bagiante, G. A. Steele and V. Zwiller.
Journal of Applied Physics **110**, 074308 (2011)
 10. *Single Photon Emission and Detection at the Nanoscale Utilizing Semiconductor Nanowires*
M. E. Reimer, M. P. van Kouwen, M. Barkelid, M. Hocevar, M. H. M. van Weert, R. E. Algra, E. P. A. M. Bakkers, M. T. Bjork, H. Schmid, H. Riel, L. P. Kouwenhoven and V. Zwiller.
Journal of Nanophotonics **5**, 053502 (2011)